School of Earth and Planetary Science

Microstructural Response of Zircon in High-Porosity Seeberger Sandstone Experimentally Shocked From 2.5 to 17.5 GPa

James Bishop

0000-0001-9025-2022

This thesis is presented for the Degree of

Master of Research – Earth & Planetary Science

of

Curtin University

Feb 13, 2022

Acknowledgements
Dr. W. Uwe Reimold (University of Brasilia) provided the shocked Seeberger sandstone thin sections on which this study was based. Dr. Aaron J. Cavosie and Dr. Nicholas E. Timms (Curtin University) provided advice, feedback, editing and supervision of this study, instruction and assistance for SEM operation, and served as thesis advisors. Dr. Gretchen Benedix served as the thesis chairperson of this study. Curtin University Graduate Research School provided a stipend scholarship. Elaine Miller (Curtin University) provided technical assistance, instruction and troubleshooting for SEM operation at the Microscopy and Microanalysis Facility in the John de Laeter Centre. Dr. Ahmed El-Mowafy is thanked for his continued support through personal crises and provision of multiple extensions for this thesis. The Space Science and Technology Centre provided financial support. The School of Earth and Planetary Science is thanked for access to equipment used in the processing of Seeberger sandstone thin sections.

Abstract

Shock metamorphism of minerals is widely recognised as a unique indicator of bolide impacts throughout the Earth's history. Shock effects have been studied in several minerals, the most widely studied being quartz. The response of minerals to shock is strongly affected by the nature of the host rock they are in. Minerals within highly porous rocks that are subjected to shock deformation respond differently than those hosted in nonporous, crystalline rocks. The difference in shock response has so far not been widely studied, with most research on shock metamorphism of minerals in laboratory settings being conducted on pure mineral samples. Little attention has been paid to either the role of shock impedance or porosity in natural samples.

Recently, shock recovery experiments by the multidisciplinary experimental and modelling impact crater research network (MEMIN) were conducted on porous, natural sandstone samples. The experiments characterised the shock response of quartz in host rocks of varying porosity, and demonstrate that for a given calculated applied shock pressure, quartz shock features formed that would typically be expected at significantly higher pressures in crystalline rocks.

In addition to quartz, the study of natural sandstone samples can provide shock response information for accessory phases such as zircon. Zircon is a common accessory phase in most rocks, and it preserves a unique set of shock responses ranging from physical deformation to the breakdown of the mineral into its chemical constituents.

The shock response of zircon hosted in porous sandstone was characterised in this study. Shock metamorphic features identified in zircon grains shocked to calculated applied pressures up to 17.5 GPa include planar fractures, vesicular melt films, planar deformation bands (PDB), mechanical {112} twins, transformation to the high-pressure polymorph and dissociation of zircon. These features were identified at calculated applied shock pressures that are 2-4 times lower than those commonly thought to produce such features in zircon hosted within a crystalline rock. The distribution of these features generally showed a progression of shock metamorphic features, radiating outward from the initial shockwave propagation point in the top-center of the sandstone charge toward the edges, showing progressive formation in concentric zones of reidite, {112} twins, PDB and melt films.

These findings correlate with those of MEMIN for quartz in a porous host rock, suggesting that the effect of porosity on shock response is not limited to only quartz, but also includes zircon and probably other minerals. The microscale response of a shockwave to a porous medium results in magnifications and reductions of the of bulk shock pressure on a microscale, with local pressures reaching up to four times the bulk shock pressure. This has implications for the identification of shock features in zircon at impact sites, as the porosity of the rock would have a significant impact on the shock response of the minerals within it.

1 - Introduction

Impact cratering is one of the most fundamental geological processes with respect to planetary formation and evolution. The extreme physical conditions involved with the process of impact cratering leads to widespread effects on the surrounding environment. The identification of impact structures and past impact events is a useful geological tool for understanding the history and characteristics of impact events through time (French and Koeberl, 2010) (Fig. 1).

Shock metamorphism refers to the reactions, polymorphic phase transformations and brittle and ductile deformation that accompanies a hypervelocity impact. The combination of high pressures and temperatures created during impact are not found at any other place on the Earth's surface, and thus shock metamorphism of minerals provides diagnostic evidence of impact events (French, 1998).

1.1 Approaches to studying shock metamorphism

Our understanding of shock metamorphism phenomena in minerals stems from observations that have been made of shock metamorphosed minerals at known impact sites (empirical observations) and through experimentation, where minerals are subjected to high-pressure metamorphic conditions in a laboratory setting (experimental observations).

Studies of known impact sites have resulted in the discovery of a variety of shock metamorphic features in minerals such as quartz (Stöffler and Langenhorst, 1994; Grieve et al., 1996; French and Koeberl, 2010), zircon (Bohor et al., 1993; Wittmann et al., 2006; Schmieder et al., 2015; Timms et al., 2017), monazite (Erickson et al., 2016) as well as other minerals. Studies of major constituent phases in crystalline target rocks such as quartz and feldspar have resulted in a shock stage classification based on the degree of shock metamorphic alteration of the target rocks and minerals, ranging from fractures in quartz and feldspar (stage 0), through to stages 1-5 with, with stages 1-5 representing progressive shock deformation of rocks between the two extremes (stage 0 to stage 5) – the latter of which represents fully melted target rock (Stöffler, 1971).

High pressures associated with impact events have been achieved in laboratory experiments on minerals. This is achieved in two fundamental ways; hydrostatic high-pressure and dynamic shock recovery experiments. Hydrostatic high-pressure experiments involve incrementally increasing pressure of a sample hydrostatically (i.e., no imposed deviatoric stress) in a cell over time until high pressures associated with impact events are reached (e.g. Reid and Ringwood, 1969). Alternatively, high pressures associated with shock metamorphism have been reproduced in dynamic shock recovery laboratory experiments, which employ the use of propellant devices to fire a projectile into a sample to generate a shockwave (e.g., Gibbons and Ahrens, 1971 and Kusaba et al., 1985). Investigations of material from static and dynamic shock recovery experiments are the only reliable way to calibrate formation

pressures of shock microstructures in minerals and relate them to empirical observations of natural impactites.

Minerals respond differently to shock compression (induced by the passing of a shockwave) and decompression (induced by the passing of a rarefraction wave) (Melosh, 1989). In turn the responses of minerals and other compounds in the target rock influences the propagation of the shockwave(s) and rarefraction wave(s). Shockwaves can be refracted and reflected causing variations in the exact stress-pressure-temperature-time (σ-P-T-t) paths experienced by particles in a rock. In recent years, advancements in numerical modelling approaches combined with shock physics has led to mesoscale numerical simulations yielding insights into shockwave propagation in heterogeneous media. In a heterogeneous, porous target, the difference in shock response of a pore compared to a grain results in changes in shockwave dynamics. This is noted in mesoscale numerical models (Güldemeister et al., 2013, Davison et al., 2016), which show that pore closure can result in significant, localised magnification of shock pressure, similar to empirical observations of quartz shock features reported in shock metamorphosed sandstone (Kieffer, 1971).

While empirical studies have focused on porous targets such as shocked sandstone (Kieffer, 1971), the majority of experimental shock deformation studies to date have focused on crystalline (nonporous) targets, primarily of single crystal or powder specimens of only one mineral. Whereas, many empirical studies focus on porous targets such as shocked sandstone (e.g., Kieffer, 1971). This has led to a knowledge gap between calibration of shock responses of nonporous targets versus porous targets.

One of the few exceptions are recent shock recovery experiments that have focused on the calibration of the shock response of natural samples of porous quartzose sandstone at calculated applied dynamic shock pressures ranging from 2.5 GPa to 17.5 GPa (Kowitz et al., 2016). These shocked sandstone samples contain the accessory phase zircon and were acquired for this study to (1) investigate the microstructures formed in zircon in porous target rocks at a range of calculated applied shock pressures and (2) calibrate the shock response of zircon hosted in the high porosity sandstone with calculated applied shock pressures and features in quartz. This study aims to achieve both (1) and (2), providing valuable new constraints for the important mineral zircon.

In this thesis and elsewhere in the literature on shock metamorphism, ‘pressure’ is a commonly used term (e.g. French, 1998; French, 2010). For the purposes of this study, three separate terms will be used referring to pressure associated with different phenomena. These are (1) the calculated applied pressure, (2) the apparent threshold pressure and (3) the maximum pressure. Calculated applied pressure (sometimes referred to as bulk shock metamorphic pressure) is the average calculated pressure applied to a sample in a shock recovery experiment. As it is a spatial average of the shock metamorphic pressure, spatial excursions in pressure above (or below) the calculated applied pressure may occur locally. An apparent threshold pressure is the pressure required to form a given shock metamorphic

feature. In the studied zircon grains, the apparent threshold pressure is the calculated applied pressure at which features such as reidite, mechanical {112} twins, and planar deformation bands (PDB) are observed. The maximum pressure is the highest pressure experienced by a sample; in this study, for example, it is the highest pressure experienced by a porous target in a shock metamorphic environment.

2 - Background – Quartz, zircon and dynamic shock recovery experiments in sandstone

The mineral quartz provides valuable insights into the processes of shock metamorphism. Quartz has been widely studied in its response to shock metamorphic conditions. It is a widespread rock-forming mineral, and it preserves unique features when exposed to shock metamorphic conditions (French, 1998). The widespread nature of quartz in crustal rocks on Earth and its response to shock metamorphism makes it ideal for studying impact events. Zircon, a common accessory phase in sandstone, also preserves evidence of shock metamorphism over a wide range of pressures (e.g. Cavosie et al, 2010; Cavosie et al, 2015; Cavosie et al, 2016). Shock recovery experiments on natural sandstone samples have recently been conducted, and provide valuable insight into, and calibration of, the shock response of quartz in porous rocks (e.g. Kowitz et al, 2013; Kowitz et al, 2016). Reviews of the current understanding of shock metamorphism of quartz and zircon, and shock deformation experiments on porous sandstones are provided below.

2.1 Shock response of quartz and its utility in impact sites

Features evident in shocked quartz ranges from physical disruption of the crystal structure to the formation of high-pressure silica polymorphs and melting.

Planar fractures (PF) are produced by low level shockwaves (5 to 20 GPa) in quartz (Stöffler, 1971). They appear as 0.5 – 5 mm long sets of open fractures at one or multiple locations in a grain, usually showing spacings of greater than 20 μm. PF can be infilled with secondary minerals (Stöffler and Langenhorst, 1994). Feather features are often associated with planar fractures (Poelchau and Kenkmann, 2011).

Planar deformation features (PDF) appear as thin sets of crystallographically-controlled planes or lamellae, sometimes decorated with small vesicles. PDF are planes of amorphous quartz where the crystallographic structure has ‘slipped’ under high strain conditions. They are usually spaced closer than PF, generally at distances of 2-10 μm apart. PF can closely resemble PDF, however PF appear to act as boundaries for planar deformation features, suggesting that PDF form after PF during shock events (Stöffler and Langenhorst, 1994). It should be noted that PF and PDF can form in sets with multiple orientations, with families of PDF and PF diagnostic of the level of shock metamorphism. Over 35 distinctive PDF orientations have been recognised in quartz (Stöffler and Langenhorst, 1994).

At higher shock pressures, quartz can transform from a crystalline structure to an amorphous state without melting known as diaplectic silica glass (Stöffler and Langenhorst, 1994). Diaplectic silica glass can be challenging to identify, as grains

with a similar appearance can result from a number of non-shock metamorphic conditions. Identification generally requires investigation through electron microscopy or x-ray diffraction (French and Koeberl, 2010).

Lechatelierite is a glassy (amorphous) phase that has quenched from molten silica. It tends to occur in veins of solidified melt within shock metamorphosed rocks. Unlike diaplectic silica glass, lechatelierite possesses vesicles and evidence of flow structures, indicating that it was a liquid prior to quenching (Stöffler and Langenhorst, 1994).

The transformation of quartz to the silica polymorphs stishovite and coesite is a known result of shock metamorphism. These polymorphs typically appear as fine-grained granular aggregates within shocked quartz shocked to at least 30 GPa, with stishovite produced in single crystal shock recovery experiments on quartz at 22-24 GPa (Stöffler and Langenhorst, 1994).

2.2 Progress in understanding responses of zircon during impacts

Zircon ($ZrSiO_4$) is a common accessory phase found in most rocks. It is useful for studying shock metamorphism because it is a mineral that preserves evidence of different types of deformation over a wide range of pressures, showing features ranging from changes in crystallographic orientation to the formation of polymorphs, and the breakdown of the mineral into its constituent dioxides – ZrO_2 and SiO_2 (Fig. 2) (Timms et al., 2017). Shocked zircon can also be used for dating impact events (e.g. Erickson et al., 2020).

As with many shock-metamorphosed minerals, irregular fracturing and comminution of grains is a common occurrence. Whilst irregular fractures can be caused by shock metamorphism, they are not indicative of an impact, as they can be formed in other non-impact related environments; (e.g. Rimša et al., 2000; Schaltegger et al., 2015).

Planar fractures (PF) are planar, open fractures in zircon that often occur in sets in one or more orientations. They indicate high shear stress sometimes associated with impact environments, where zircon has broken along a single crystalline shear plane (Cavosie et al., 2010; Timms et al., 2012; Erickson et al., 2013;). Shock recovery experiments show that PF can form at pressures of up to 20 GPa and temperatures below 700 °C (Leroux et al., 1999). Whilst PF are often formed as a result of shock metamorphism, they have also been observed in certain igneous environments (Schaltegger et al., 2015). When planar fractures that are not open are observed, they are referred to as planar features.

Dislocation creep (crystal plasticity) is the formation and migration of crystallographic defects (edge and screw dislocations), processes which are facilitated by elevated temperature and stress conditions (Reddy et al., 2006; Timms et al., 2012). The cumulative effects of formation of such defects can lead to crystallographic misorientations across a host grain at magnitudes of 45° or greater. Dislocations can form planar arrays known as low-angle (<10°) boundaries. Whilst crystal plastic strain can form in zircons located within ductile shear zones (e.g., Piazolo et al., 2012), and magmatic settings (Reddy et al., 2009) tectonically induced misorientations tend to be small, typically <14°. Impact-related crystal plasticity can

result in much greater misorientations (35°) across a host grain (Timms et al., 2012; Erickson et al., 2013; Montalvo et al., 2017).

Planar deformation bands (PDB) are tabular domains that are misoriented from the host grain and bounded by two parallel low-to moderate angle boundaries, usually occurring in sets that can transect large portions of a zircon grain (Timms et al., 2012; Erickson et al., 2013). Kovaleva et al. (2015) describes PDB as being oriented parallel to {100} as well as {001}, with misorientation axes parallel to <100> or <001>. PDB that accommodate low-angle misorientations of 1-2° can form in high-strain rate, high-grade regional metamorphic environments (Kovaleva et al., 2015). In contrast, PDB formed in shock metamorphic environments can accommodate well over 10° of misorientation (e.g., Montalvo et al., 2017).

Zircon can form deformation twins in impact settings (Moser et al., 2011; Timms et al., 2012, 2018; Erickson et al., 2013). Twins occur as ~1 μm wide lamellae along {112} in zircon, commonly in sets (Timms et al., 2012). Multiple orientations of {112} twin sets are possible as up to four sets of symmetrically equivalent {112} twins may form in zircon (Erickson et al., 2013; Cavosie et al., 2015, 2018; Timms et al., 2018). The form of the twins can range from isolated domains to highly lamellar features. A crystallographic misorientation relationship of 65° around <110> of the host grain defines {112} twins (Moser et al., 2011; Timms et al., 2012, 2018). Mechanical {112} twins have only been reported in one laboratory experiment, a static (diamond anvil cell) experiment, quenched at 20 GPa (Morozova et al., 2017). As this is the only known experimental constraint on the formation of mechanical {112} twins, exact formation conditions remain poorly constrained. Mechanical twins have been reported in empirical studies of the Vredefort dome at shock pressures of at least 20 GPa (determined by observation and modelling of specimen distances from the centre of the crater, and observations of shock deformation features in quartz) (Moser et al., 2011). Currently there are no dynamic shock experimental constraints for twinning in zircon.

Reidite, a high-pressure polymorph, can form in impactites (Glass et al., 2002; Cavosie et al., 2015a). Reidite, also tetragonal, is approximately 11 % denser than zircon, yet coordination of Zr, Si and O atoms remains the same as is found in zircon (Glass et al., 2002; Glass and Liu, 2001; Reid and Ringwood, 1969). Reidite exists in a variety of forms, including lamellar, granular aggregates at grain boundaries, or within grains, and as transformed domains of a zircon grain (domainal), and dendritic habits (e.g. Cavosie et al., 2015; Erickson et al., 2017; Timms et al., 2017; Cavosie et al., 2021).

Reidite transforms with a fixed crystallographic orientation relationship to the host zircon grain. The symmetry of both phases can result in up to eight symmetrically equivalent variants of reidite (Erickson et al., 2017; Timms et al., 2017). An example of the relationships produced include approximately 90°/<110> misorientation which results in a $(001)_{zircon}$ aligned with $\{110\}_{reidite}$, $\{001\}_{reidite}$ aligned with $\{100\}_{zircon}$, a shared $\{110\}_{zircon}$ and $\{110\}_{reidite}$ as well as an alignment of $\{112\}_{reidite}$ to $\{110\}_{zircon}$ (Erickson et al., 2017; Timms et al., 2017; Cox et al., 2018).

At temperatures above 1673 °C and at low pressure (much less than 1 GPa) following high pressure conditions in impact environments (Timms et al., 2017) zircon can dissociate into two constituents; silica (SiO_2) and zirconia (ZrO_2) (Kleinmann, 1968; Kaiser et al., 2008). The dissociation process commonly results in a vermicular, or blebby texture indicative of unmixing of silica from the original zircon, leaving behind the more refractory zirconia (Timms et al., 2017). At higher temperatures (>1675 °C), the dissociation of zircon will lead to the formation of a molten liquid silicate fraction, and solid ZrO_2 (tetragonal). At temperatures above ~2300 °C solid zirconia (cubic) will melt and mix with the silicate liquid excepting a certain molar fraction of ZrO_2 and SiO_2 in which two immiscible liquids are present (Timms et al., 2017). As the melt cools, solid cubic zirconia will again form, and this may transform to tetragonal and/or monoclinic zirconia, and even react with silica back to zircon during cooling (Timms et al., 2017).

Granular zircon has a polycrystalline texture seen in grains that undergo elevated temperature and pressure conditions. The pressure threshold for the granularization of zircon is unknown, but is likely a high T, low P phenomena (Timms et al., 2017), and as a result of this threshold being above that of reidite, granular reidite and granular zircon reverted from reidite may be observed (Timms et al., 2017). A particular subset of granular (polycrystalline) microstructure in zircon that specifically forms by reversion of reidite has been termed FRIGN (Former Reidite in Granular Neoblastic zircon) (Cavosie et al., 2018). In zircon, reidite is converted back into granular neoblastic zircon by high temperature conditions, below pressures at which reidite is stable (Kusaba et al., 1985). This back-transformation preserves the orientation relationships of reidite to zircon, revealing the former presence of reidite that has since been transformed back into zircon at much higher pressures and temperatures than normal dissociation of zircon (Cavosie et al. 2018). U-Pb geochronometers are reset during the formation of neoblastic zircon by recrystallisation, and have been targeted to date impact events (Kenny et al., 2017; Hauser et al., 2019; Rasmussen et al., 2020).

Approximate pressure-temperature conditions, and P-T paths can be estimated based on the assemblage of shock metamorphic features within some shocked zircon grains (Timms et al., 2012). Zircon may experience a high-temperature excursion, high pressure excursion, or both. A complex suite of possible features may exist within shocked zircon; such as the type of granular texture that is present, or the habit of reidite, may give clues as to the history of the grain (Timms et al., 2017).

2.3 Experimental constraints on shock metamorphism of zircon

Current understanding of the shock response of zircon is based on experiments conducted on pure samples of the mineral that were not included in a host rock. Reid and Ringwood (1969) showed through the use of a high-pressure apparatus in static experiments that the high-pressure $ZrSiO_4$ polymorph reidite forms from zircon above pressures of 12 GPa at elevated temperatures of 900 °C.

The conditions of the Reid and Ringwood (1969) experiments do not replicate the dynamic shock conditions experienced by zircon in a host rock during an impact

event, as the extreme pressure (and in some cases, temperature) conditions are present for fractions of a second, rather than hours or days. Dynamic shock recovery experiments more closely simulate the metamorphic conditions that occur within the crust, where high pressure and temperature conditions exist over short (s-length) timescales.

Dynamic shock recovery experiments involve the study of shockwaves interacting with mineral samples, rather than static loading within apparatus such as a diamond anvil cell. Shockwaves more accurately replicate the dynamic nature of impacts, with minerals experiencing large changes in pressure over short periods of time as they do in nature.

Kusaba et al. (1985) conducted shock recovery experiments using a light gas gun to accelerate a projectile to impact upon zircon powder cylinders (10mm diameter, 3mm thick) encased in steel, and large (cm-scale) crystals of zircon cut into thin millimeter thick slices, similarly encased to protect them from fragmentation. These shock recovery experiments resulted in the formation of several shock features within zircon. At pressures of around 30 GPa, reidite was found to be present in amounts of approximately 5% (in both single-crystal and powder). At 40 GPa the abundance of reidite increased to 30% (single crystal), while 100 % of zircon had been converted to reidite at 54 GPa (single crystal). Additionally, a significant amount of tetragonal ZrO_2 was detected through the use of X-ray diffraction in a single crystal sample shocked to 94 GPa indicating the decomposition of $ZrSiO_4$ (either as zircon or reidite) to ZrO_2 and SiO_2. However, the maximum temperature conditions achieved in this experiment were not known. The metastability of reidite at high-T was demonstrated by showing that the post shock product rapidly reverted to zircon upon heating to 1200 °C (Kusaba et al., 1985).

Leroux et al. (1999) conducted shock recovery experiments on thin zircon plates. Planar shock waves were generated with a high explosive apparatus, at pressures of 20, 40 and 60 GPa, as described by Deutsch and Schärer (1990). Planar features were observed by Leroux et al. (1999) under SEM in the 20 GPa sample, 10-50 μm apart and 1-2 μm across. Reidite was characterised under TEM by electron diffraction as comprising a small fraction of the 40 GPa sample. The 60 GPa sample was reported to be completely transformed to reidite, with {112} twins reported in reidite from this sample but not in zircon. Additionally, a polycrystalline texture consisting of 20-100 nm reidite grains were observed at 60 GPa, corresponding to a granular texture, or granular reidite.

Whilst Kusaba et al. (1985) and Leroux et al. (1999) successfully demonstrated the shock response of zircon and also calibrated that response to known pressures, the conditions of the experiments do not necessarily replicate that which may be experienced by zircon in a natural impact setting, as the starting materials used (single crystal or powdered zircon) are not representative of how zircon exists in nature. Most zircons that experience shock metamorphism are hosted in crystalline or porous host rocks (or sediments), exposing the zircon grains to complex interactions with their surrounding environments as the shock-wave passes. Therefore, dynamic experiments on natural rock samples are needed to replicate the

natural conditions that zircon and other minerals would experience during impact events. Such experiments could potentially provide the most accurate calibration of the shock metamorphic response of zircon at known pressures.

2.4 Shock recovery experiments on porous sandstone – MEMIN group

MEMIN (the Multidisciplinary Experimental and Modelling Impact research Network) is an impact cratering dynamics group in Germany that has conducted a large number of shock recovery experiments since 2009. For target materials, they used whole rock samples, through the use of projectiles fired from gas guns, high explosive apparatus and laser melting experiments (Kenkmann et al., 2018).

MEMIN researchers have shown through shock recovery experiments using high-explosive type apparatus (Fig. 6), that for sandstone, increased porosity results in an increasing presence of higher-pressure-than-expected shock metamorphic features. Their results show that calculated applied shock pressures which would not typically be capable of producing these features within crystalline (nonporous) rocks, can be magnified by several times at the pore-grain scale in porous rocks. This results in much higher local pressures (on a pore-grain scale) than the calculated applied pressures, leading to the presence of shock metamorphic features that would be expected at higher bulk pressures in crystalline rocks (Kowitz et al., 2016) (Figs. 3a, 5a, 5b).

The results of MEMIN experimentation on porous rocks have been supported by mesoscale numerical modelling of porous materials subject to shock conditions (Güldemeister et al., 2013), which suggest that a given calculated applied shock pressure can be magnified by up to four times at the grain/pore scale.

2.4.1 Findings of MEMIN; Seeberger sandstone

Seeberger Sandstone is quarried by the TRACO company at Seeberg, near Gotha, Germany. The sandstone is a light coloured sandstone deposited during the Triassic (ca. 215 Ma), and represents well-sorted fluvial sediments (Kenkmann et al., 2011). The cylindrical charges were cut from blocks of Seeberger sandstone, and are described as having an average grain size of 0.1 mm, porosity of 25-30 vol%, pore size of 20-100 μm with 89 vol% quartz (Kowitz et al., 2013a, b; Kowitz et al., 2016). Accessory phases identified in Seeberger sandstone include rutile, monazite, xenotime and zircon. Seeberger sandstone charges were shocked to calculated applied pressures ranging from 0 GPa (unshocked reference sample) to 17.5 GPa, increasing in increments of 2.5 GPa (Kowitz et al., 2016).

A wide range of shock phenomena were encountered in previous MEMIN studies of shocked Seeberger sandstone (SST) L3 (the 25-30 vol% sandstone described above), including fracturing, formation of melt, planar deformation features (PDF) in quartz and the formation of high-pressure silica polymorph (stishovite). SST L3 (water saturated) showed stishovite at a higher pressure (10 GPa compared to 7.5 GPa for SST L3, dry). This indicates that water saturation increases the pressure

required for shock features to form in porous environments, which is described as being a result of the high pore stiffness for confined, water saturated samples that inhibits pore collapse and the resultant localised pressures (Kowitz et al., 2016).

2.4.1.1 Fracturing & PDF

Fracturing was described both on the macro- and microscale. Macroscopic fractures were most prominent in sets that cross-cut the sample in a diagonal orientation, radiating from the corners (edges) of the charge toward the centre. At increasing pressures these large-scale fracture zones increase in their level of comminution, often hosting melt as well (Kowitz et al., 2013a; Kowitz et al., 2016) (Fig. 3b). Microscopic fractures (intragranular fractures within quartz) increased with shock pressure to a maximum saturation of 236 fractures/mm in SST L3 (10 GPa) (Kowitz et al., 2013b; Kowitz et al., 2016). PDF in quartz were only identified in the 15 and 17.5 GPa SST L3 sandstone charges (Kowitz et al., 2016).

2.4.1.2 Melt veins

Melt veins were noted both within quartz grains and in macro-scale fractures. Kowitz et al. (2013a) identified four distinct types of melt occurrences within the samples. The first type of melt was vesicular, and in backscattered electron (BSE) images is darker than surrounding shocked quartz. Flow structures are present in this melt and compositionally silica is dominant (54 wt%), followed by alumina at 26 wt%. This first type of melt was present in all shock recovery experiments using SST L5 (12-19 vol% porosity Seeberger sandstone) (Kowitz et al., 2013a). The second melt type is visually similar to the first, also having a similar chemical composition, but higher Fe content than the first type. This melt was only observed in experimental runs of ≥7.5 GPa (Kowitz et al., 2013a). The third melt type is again similar to the first and second, however contains small (0.5-2 μm) Fe particles (presumably originating from the ARMCO iron cylinder). This melt type is rarely vesiculated, however does exhibit flow structure (Kowitz et al., 2013a). The fourth type of melt is pure Fe, injected into the sample charge from the ARMCO iron sample container, found at the margins of the charges (Kowitz et al., 2013a).

2.4.1.3 Silicate glasses and melts

SiO_2 melt and diaplectic quartz glass began to form at 5 GPa in SST L3. The total volume of diaplectic glass and melt produced in the recovery experiments was up to 80 vol% diaplectic and melt for the SST L3 charge shocked to 17.5 GPa (Kowitz et al., 2013a; Kowitz et al., 2016).

2.4.1.4 High-P SiO_2 phases

The high-pressure silica polymorph stishovite was found within lechatelierite veins in SST L3 on the order of 0.7 μm to 1.5 μm. TEM analysis of the microscopic veins showed the presence of stishovite crystals. Stishovite was found in samples shocked from 7.5 GPa to15 GPa.

2.4.2 Implications of the prior MEMIN results

The dynamic shock experiments described above have shown that when a shock wave passes through a porous medium such as sandstone, pressure can be magnified by several times at the local pore-grain scale resulting from pore collapse (Kowitz et al., 2016). The stark difference in the behaviour of porous rocks compared to crystalline rocks when exposed to shock waves required modification of the original shock stage classification scheme for quartzo-feldspathic rocks described by (Stöffler, 1971) (Fig. 4). The original classification scheme for porous sandstone (Fig. 5a) was originally from empirical observations of shocked sandstone at Meteor Crater (USA) by Kieffer (1971) and Kieffer et al. (1976). This scheme indicates significantly lower pressure classifications for similar shock stages, showing the effect porosity has on shock response. The shock stage classification for porous sandstone was modified based on the results of the dynamic shock experiments, leading to a new classification and calibration of shock stage in porous sandstone (Kowitz et al., 2016) (Fig. 5b).

2.4.3 Aims and objectives of this study

Here, findings are presented which evaluate the hypothesis that when a shockwave passes through zircon (or indeed any mineral) hosted within a porous (anisotropic/heterogeneous) medium, porosity will cause localised, grain-scale magnifications in pressure and temperature that may result in the presence of shock metamorphic features within the mineral that are normally encountered at higher calculated applied shock pressures in nonporous (crystalline) targets.

This study aims to introduce finer calibration of the shock pressures required to produce shock metamorphic phenomena in zircon, with an emphasis on mechanical {112} twins and the high-pressure $ZrSiO_4$ polymorph reidite. The studied zircon grains are hosted in the same thin sections of L3 Seeberger sandstone with 25-30 vol% porosity studied by Kowitz et al. (2013, 2016) and that were used to develop a shock stage classification for porous rocks based on the response of quartz (Fig. 3a).

2.4.4 Sample Background, Methods and Analytical Techniques

The sample suite analysed in this study consists of Seeberger sandstone L3 (SST L3) with initial porosity 25-30 vol%. Thin sections were cut from sandstone charges which were experimentally shocked at calculated applied pressure intervals (calculated based on the shock impedance between the steel driver plate and sandstone charges) of 2.5 GPa, ranging from 0 GPa (unshocked) to 17.5 GPa (Kowitz et al., 2013a). The sandstone is a well-sorted fluvial arenite with subrounded quartz grains, many of which possess iron oxide and clay mineral rims (Kenkmann et al., 2011).

The thin sections will be referred to herein by their respective calculated applied pressures. The shock experiments were conducted at the Efringen-Kirchen facility at the Ernst-Mach Institut, Germany, in a high-explosive type apparatus (Kowitz et al., 2013a) (Fig. 6). Seeberger sandstone charges were prepared as 15 mm by 20 mm cylinders (Fig. 7) that were drilled into the bedding plane of the sandstone, so the bedding was parallel to the long axis of the cylinder (Kowitz et al., 2013a). Pressure

calculations were conducted to an accuracy of ±4% using the method of graphical impedance matching at the sandstone-ARMCO iron interface (Kowitz et al., 2013a, 2016).

All thin sections used in this study, except the 10 GPa sample, were cut centrally along the vertical long-axis of the sandstone charge, and thus represent a vertical section through the cylinder (Fig. 7). Most sections thus provide a ‘vertical’ perspective on the propagation of the shock wave front. The 10 GPa section is a crescent-shaped thin section, cut parallel to the horizontal axis (parallel to the flat edge) of the cylinder, representing a ‘horizontal’ perspective relative to the shock wave propagation front. A 10 GPa vertical section was not available for this study, and the depth of the 10 GPa thin section from the ‘top’ of the sandstone charge is unknown.

The Seeberger sandstone charges were shocked to selected pressures at MEMIN facilities and then cut into thin sections for analysis. The eight thin sections were trimmed by a few millimeters to fit instrument sample holders at Curtin University, and polished in a solution of 0.05 µm colloidal silica in NaOH (pH = 10) solution on a Buehler Vibromet II (vibratory polisher) for 4 hours, before being carbon coated to a thickness of 5 nm.

3 - Methods and analytical techniques

The eight sections of Seeberger Sandstone were analysed using a TESCAN MIRA3 field emission scanning electron microscope (FE-SEM) at the John de Laeter microscopy and microanalysis facility at Curtin University, imaging in both backscattered electron (BSE) imaging and electron backscatter diffraction (EBSD) mapping mode. Operating conditions typically involved a working distance of 20 mm, using a 20 kV accelerating voltage [beam intensity (equivalent to current) = 16], with beam current approximately 1.4 nA. EBSD pixel resolution ranged from 50 nm to 300 nm, with most maps being conducted at 50 nm resolution. The match units used were zircon 5260 (Hazen and Finger, 1979) and reidite 6032 (Farnan et al., 2003).

Each thin section was first surveyed to identify the number of zircons present using BSE. The use of EDS (Energy Dispersive Spectroscopy) allowed the identification of the Zr, Si and O peaks indicative of zircon. BSE imaging additionally allowed for the identification of nonplanar fracturing and planar fracturing in zircon, as well as the presence of zircon dissociation textures. Also identified in BSE were quenched vesicular melt films around zircon grains, and fracturing and comminution of the matrix quartz grains.

Once zircon grains were identified and their location mapped within the thin section, EBSD orientation analysis was conducted on a representative population of grains. For most thin sections, all zircon grains were mapped by EBSD. EBSD analysis allowed for the identification of microstructures associated with crystal plasticity, such as PDB and mechanical {112} twins. Reidite in zircon was identified as well. EBSD files were generated in AZtec (Oxford Instruments v. 4.2-4.4) and were processed with the Oxford Instruments HKL Channel5 analytical and post-processing software suite. In Channel, the modules Tango and Mambo were used to conduct microstructural analysis and generate pole figures, respectively. This allowed for the graphical representation of PDB, mechanical {112} twins, reidite, and other crystal-plastic microstructures.

Additionally, the location of each zircon was recorded on a BSE image of the entire thin section, along with the shock metamorphic features in each zircon. Such maps provide information on the spatial distribution of shock metamorphic features (and therefore shockwave intensity) within each Seeberger sandstone charge. BSE maps were colour-coded for the distribution of shock metamorphic features to allow regions of like features to be connected and distinguished.

The Oxford Instruments HKL Channel 5 post-processing software suite has several processing modes that are useful for the identification of shock metamorphic features in zircon. Analysis and data display modes utilised in the Channel software suite in the Tango program include crystallographic orientation maps using an inverse pole figures (IPF) colour scheme, band contrast (BC – a measure of EBSD pattern quality), phase identification, special boundary (SB) detection, and user-defined crystallographic orientation of ‘texture component’ (TC). Additionally, pole figures were be generated within the Mambo program to analyse the crystallographic relationships between the host zircon and reidite or twinning.

Inverse pole figure (IPF) is a colour representation of crystallographic orientation in the sample reference frame (i.e., x, y, z). Colours are assigned to areas of a mapped grain based on the orientation of the poles of the crystallographic axes relative to a principal direction on the map.

Band contrast (BC) images are a greyscale, with tone representing the signal strength of the electron backscatter diffraction pattern. Areas of a zircon grain with a higher signal strength appear brighter in BC, whilst areas of poor signal strength appear darker. This analysis mode is useful for the identification of intra-granular fractures within zircon, as well as identification of areas of a grain that indexed well (producing a strong diffraction pattern) or indexing poorly (producing a weak diffraction pattern).

Phase maps were produced by assigning colours to phase for each data point within an EBSD map. In this study, phase maps are principally used to show the distribution of zircon and reidite. Reidite is assigned one colour (for example, red), and zircon is assigned another (usually green).

Special boundary (SB) maps were developed to visualise misorientations with specific angles/axes between adjacent data points. As all angular relationships among all pixels are recorded, specific orientations can be highlighted. This is useful for the identification of {112} twins, which are defined by a 65° misorientation around <110> of the zircon host grain. The special boundary function will highlight all selected locations where this specific angle/axis relationship exists for adjacent pixels; in this case a 65° misorientation around <110> characteristic of mechanical {112} twinning in zircon.

Texture component (TC) is a colour-coded display of the misorientation of adjacent pixels of a selected phase. A range of misorientations is specified (e.g. 0-20°) from a user-defined reference point, and colours are automatically assigned based on the magnitude of the misorientation from the reference. In this study, a rainbow colour palette is used, where blue defined the reference orientation, while red shows areas of misorientation approaching the specified range limit. If a misorientation exceeds the specified range, it will not be coloured.

Pole figures were generated from EBSD files using Mambo. Pole figures can be used to evaluate the crystallographic relationships among host zircon and, twins, PDB, and reidite (as described in section 2.2). In the case of reidite, should the predicted relationships be observed and confirmed (Erickson et al., 2017), the instance of reidite can be validated. In the same manner, pole figures can be used to confirm the presence of mechanical twinning by visualising a 65° misorientation between host and twin in the {112} plane, where the twin and host share a <110> direction. All pole figures presented here are equal area, lower hemisphere projections.

All results were assembled and analysed to produce a calibration of shock features produced in zircon at variable pressure in a sandstone host of fixed porosity of 25-30 vol.%. The tabulated results were then mapped onto panoramas of the entire thin sections (for samples that showed measurable distributions of features), showing the

spatial distribution of shock features (and therefore pressures) within an individual sandstone charge.

4 – Results

A total of 597 zircon grains were identified across the eight thin sections analysed, ranging from the unshocked reference sample (here referred to as 0 GPa) to 17.5 GPa. Of the 597 zircon grains identified, 414 were mapped by EBSD (69%). This corresponds to between 13 to 71 grains per sample (average 52). The number of zircon grains in each sample ranged from 48 to 100 (average 75). Detailed statistics on the number of zircons analysed in BSE, EBSD and their shock metamorphic features can be found in Table 1.

Planar fractures in zircon were identified based on three criteria. These criteria were that the fractures be planar, in a set of at least 3, and either were cutting across a large portion (50%) of the grain, or were closely spaced in a parallel set within a localised area.

4.1 - Shock metamorphic features observed in BSE and EBSD

4.1.1 - Unshocked reference sample, 0 GPa (vertical section)

The sandstone in the unshocked (0 GPa) sample was found not to be fractured or deformed, with primary porosity (Fig. 9a), as well as the rectangular shape of the charge preserved (Fig. 8a, 9a). The zircons identified in BSE show evidence of nonplanar fracturing; no planar fractures were observed (Figs. 10, 11). The surrounding quartz grains preserve some fracturing. Fractures in both minerals are likely due to sedimentary processes, such as diagenesis and compaction.

A total of 13 of the 78 zircon grains (17%) were mapped by EBSD, which are distributed throughout the thin section. These 13 grains show little evidence of crystal plastic deformation, with maximum misorientation within coherent sub-domains observed in the analysed zircons below 2°. The misorientation internal to the grains likely a result of minor physical deformation (burial), while misoriented regions at the edges of the grain are fragments that have separated from the host grain (Fig. 12). No PDB and only very weak lattice strain within coherent (i.e., non-fractured domains) were observed in the mapped zircon grains.

4.1.2 - 2.5 GPa (vertical section)

Almost all primary porosity in the 2.5 GPa sample was removed (Fig. 8b). The sample was noticeably compacted but still has an overall rectangular shape. At the section-scale, fractures were present oriented diagonally from the top left and bottom right corners, and are connected in the middle. At the grain scale, significant compaction was observed and fracturing of quartz grains resulted in a small amount of secondary porosity (Fig. 9b).

The 2.5 GPa section contained a total of 100 zircon grains. Of these, all were surveyed in BSE and many show nonplanar, irregular fractures. 5 of 100 grains possessed planar fractures, (Fig. 11b). Some zircon grains were severely disrupted and fragmented, with evidence of block rotation observed within fractured grains, distinguishable by displacement of grain fragments. Of 100 zircon grains, 47 were mapped by EBSD. One well-formed PDB with a crystallographic misorientation of 12° across the band was observed (Fig. 13). Four other PDB were observed with

lower degrees of misorientation. Crystal plastic deformation microstructures were observed in all zircon grains within the 2.5 GPa section. The total misorientation (including misorientations associated with rigid fracture block rotation) ranged from less than 5° across single grains to well over 80° across grains that were severely disrupted and had experienced block rotation. Misorientations across single continuous domains within zircon grains was generally <10°.

4.1.3 - 5 GPa (vertical section)

All primary porosity in the 5 GPa sample was removed. The overall shape of the section appears to show less vertical shortening than the 2.5 GPa section, however significantly more disruption (fracturing) is present. A significant amount of fractures are present, observable on both the entire thin section (Fig. 8c), and on a pore-grain scale, resulting in a small degree of secondary porosity within fractures (Fig. 9c).

A total of 83 zircons were identified. All 83 zircons were surveyed using BSE in the 5 GPa sample. Of these, 3 grains show planar fractures (Fig. 11c), while all but one grain shows nonplanar fracturing (Fig. 14a). In the 5.0 GPa section, a total of 41 zircon grains out of 84 were mapped by EBSD. One zircon showed < 5° of crystal plastic deformation. This was the same zircon grain noted to lack nonplanar fractures in the BSE survey. The internal misorientation across the grain was <1°, with the exception of the bottom right corner of the grain, which records a misorientation of approximately 5° (Fig. 14b). The corner of the zircon grain that experienced the greatest deformation was facing towards the shock wave-front. Only one grain analysed contained PDB; the PDB occurred as a set, with individual misorientations within the set ranging from 3 to 8° (Fig. 15).

4.1.4 - 7.5 GPa (vertical section)

All primary porosity was removed from the 7.5 GPa sample. Fracturing both on the sample scale and pore-grain scale has progressed compared to the 2.5 GPa and 5 GPa samples, with fractures cutting across multiple grains seen across the sample. The sample appears to be further compacted, with continued shortening along the vertical axis and expansion along the horizontal axis, showing deformation on a bulk scale (Fig. 8d, 9d). Pronounced concavity is visible along the top surface. As with the 2.5 and 5.0 GPa samples, planar fractures and nonplanar irregular fractures are present in zircon. Vesicular melt films around zircon grains were observed in this sample.

A total of 94 zircon grains were identified in BSE. All grains except one (#63) possess nonplanar fracturing, whilst 5 grains have planar fractures identified in BSE (Fig. 11d). Quenched silicate melt films are present around 11 zircon grains (Fig. 16). The 7.5 GPa sample represents the first appearance of melt films around zircon. Of the 94 zircon grains present in the 7.5 GPa thin section, 54 were analysed by EBSD. A total of 11 grains contain PDB (11 %), which preserve a range of misorientations, ranging from <5°, up to 12° (Fig. 17).

4.1.5 - 10 GPa (horizontal ‘crescent’ section)

All primary porosity was removed from the 10 GPa sample. Fractures are seen to further progress in the microstructure compared to the 7.5 GPa sample, resulting in increased secondary porosity compared to the previous samples (Fig. 9e). Sample-scale fractures appeared to be concentrated in ring-like fractures that radiate outward from the centre (Fig. 8e). Due to the horizontal cross section of the sample, the level of compaction and shape of the charge cannot be directly compared to the other samples.

A total of 71 zircon grains were identified in the 10 GPa thin section. Of these, 1 grain contained planar fractures (Fig. 11e). Additionally, 24 zircon grains (34%) have melt films around their margins. All 71 zircon grains were analysed with EBSD. Of those analysed, 7 contained PDB (10%), 4 contain mechanical twinning (6%) and 6 contain reidite (9%). PDB in this sample were observed isolated, generally in single ‘wedge’ shaped zones, in sets of single and multiple parallel PDB at different, complex orientations, each accommodating misorientations ranging from 3 to 10°. (Figs. 18, 19). Four grains in the 10 GPa section have mechanical {112} twins. Of these grains, one possessed well-formed twin lamellae (Fig. 20a, b). The other three grains possessed only small linear segments of adjacent twin pixels. Seven zircon grains were found to have been partially transformed to reidite. The proportion of reidite converted from zircon was generally small, comprising only up to 0.15% of the grain. The habit of reidite found in this charge is domanial; no instances of lamellar reidite were observed (Fig. 21). The proportion of reidite-bearing grains in this sample was 7 of 71 (10% of the total grains present). The 10 GPa sample represents the first appearance of diagnostic shock microstructures in zircon.

4.1.6 - 12.5 GPa (vertical section)

All primary porosity is significantly diminished in the 12.5 GPa sample, with more intense compaction and deformation of the charge than the lower pressure charges (e.g., 7.5 GPa). The deformation of the charge has continued from the previous similarly cut section (7.5 GPa), with the sides of the section showing a strong convex shape, and the top showing significant concavity (Fig. 8f). Denser networks of fractures run from the corners to the centre of the sample from the corners, whilst small comminution zones are seen to have developed along these fractures (Fig. 9f).

A total of 60 zircon grains were identified in the 12.5 GPa section. Of these, 3 (5%) possess planar fractures/features (Fig. 11f) and 32 (53%) have vesicular melt films on the margins of the grain. Two zircon grains, zircon #9, and #13 exhibited evidence of dissociation to zirconia along grain margins. In BSE, small (<40 nm) granular aggregates occuring on the margin of comminuted and fragmented grains, that are brighter in BSE (and therefore have a higher average atomic number than zircon), suggesting that they are likely baddeleyite (Fig. 22). Of 59 grains analysed via EBSD, 5 have PDB, 11 have {112} twins and 20 have reidite (in domanial or lens-like habits). An example of a PDB (along with a twin) can be found in Figure 23. Misorientations across PDB in the 12.5 GPa sample ranged from 5 to 15°.

Twinned grains are more prevalent in the 12.5 GPa sample compared to the 10 GPa sample (19% for this sample as opposed to 6% for 10 GPa). Twin habits in the 12.5 GPa sample include examples of single twin lamellae toward the extremities of grains (Fig. 24), as well as well-formed sets of twin lamellae across large portions of a grain (Fig. 25). Domainal and lens-like habits of reidite were observed in the 12.5 GPa sample. Examples of reidite found in this sample are shown in Figure 26. The relative proportion of zircon converted to reidite was observed to be at most 0.5% of the grain, compared to at most 0.2% of the grain in the 10 GPa section.

4.1.7 - 15 GPa (vertical section)

All primary porosity is absent in the 15 GPa sample, with some secondary porosity formed by fractures and vesicles in quenched melt pockets. The overall shape of the charge has changed significantly (Fig. 8f), with a further increase in the convex shape of the sides of the section compared to 12.5 GPa, however the top of the sample does not appear to show significant concavity and is instead an irregular shape. A higher fracture pattern density is present compared to the 12.5 GPa sample, along with zones of comminution (Fig. 9f).

Of the 48 zircon grains identified in the 15 GPa sample, 18 (37.5%) zircon grains had quenched melt films around them, and none possessed planar fractures. All 48 grains were mapped via EBSD, enabling PDB to be identified in 5 grains (10%). Misorientations across individual PDB were generally low (<10°). However, one grain (#24) possessed two orientations of PDB, with misorientations across PDB ranging from 5 to 7° (Fig. 27). Twins in the 15 GPa sample are limited to one zircon grain. Within this grain, two regions with a concentration of closely associated twin boundaries were observed, as well as reidite (Fig. 28). Reidite was present in 10 of 48 zircon grains (21%). All occurrences of reidite in this sample were domanial. In some instances, reidite comprised a significant portion of the grain (up to 4% of the EBSD mapped region) (Figs. 29, 43c).

4.1.8 - 17.5 GPa (vertical section)

All primary porosity has been removed from the 17.5 GPa sample, with secondary porosity present as a result of the formation of fractures and shear zones, or vesicles in melt zones. Strain of the thin section on a sample scale is quite pronounced, as the charge is now wider than it is tall; the sample sides are profoundly convex, while the top of the sample is profoundly concave (Fig. 8g). The sample is pervasively fractured, and discrete shear zones dominate the microstructure (Fig 9g).

A total of 62 zircon grains were identified in the 17.5 GPa sample. Of these, one grain possessed planar fractures (Fig. 11g). A total of 31 zircon grains (50%) have quenched melt films surrounding them. All 62 zircon grains were mapped in EBSD. 9 grains (15%) preserve PDB. The PDB are generally low-angle (≤ 10° misorientation across the PDB), and were not observed to occur in multiple orientations within individual grains (i.e. Fig. 30). 8 of 62 zircon grains have {112} shock twins. Of particular interest was zircon #46, which displays distinct twin domains that were disaggregated and fractured from the main portion of the grain (Fig. 31), and zircon 29 which shows a set of twins in a small portion of the grain, with some twin lamellae

possibly being smaller than the step size of the analysis (Fig. 32). Reidite was observed in 25 of 62 grains (40%). The habit of reidite observed in the 17.5 GPa sample was entirely domainal. A significant portion of some zircon grains were converted to reidite (up to 6% of the mapped grain) (Figs. 33, 43d).

5 – Discussion

5.1 distribution of deformation features

The extent of shock metamorphic features in the 2.5 to 7.5 GPa thin sections was limited, consisting of zircon grains with PDB, planar fractures and melt films (7.5 GPa sample only), none of which are currently considered to be diagnostic of shock metamorphism. The distribution of PDB, PF and melt films across the 2.5 – 7.5 GPa charges is shown in Figures 34, 35 and 36.

Shock microstructures within zircon grains in the 10, 12.5, 15 and 17.5 GPa samples were much more varied, including PDB, {112} twins, reidite and evidence of zircon dissociation. The spatial distribution of features such as reidite, twins and PDB were observed to have common elements, such as the grouping of reidite and twin-bearing grains toward the top or centre of the thin sections, corresponding to the top or centre of the sandstone charges (Figs. 37, 38, 39 and 40). The distribution of these features was mapped in these thin sections, with like features representing a single zone. The distribution of these like-feature zones was often found to be progressive, with reidite zones being near the top or centre of the thin section, while twin and PDB zones extended out further (lower) from this area. The semi-concentric distribution varies with the orientation of the thin section (vertical or horizontal) and with pressure. The reidite zones either wholly or partially overlap zones containing twins and PDB in the 10 to 17.5 GPa thin sections.

Despite the fact that some grains in these regions possess features such as twins, reidite and PDB, not all grains in these regions possess these features. This shows that in addition to broad, sample-scale pressure gradients, there are micro-scale variations in pressure as well, and this grain-scale heterogeneity in pressure results in some zircon grains possessing shock features, and other nearby grains possessing none.

The distribution of shock microstructures in zircon across all samples was observed to be non-uniform. This suggests that shock pressures in the sample charges were similarly non-uniform. A uniform distribution would show all the shock features distributed randomly throughout the thin sections, but this was not the case. Instead, shock features are mostly spatially confined to discrete zones that show similar distributions throughout various pressures, with certain shock features such as reidite and twins generally restricted to the top halves of the thin sections.

The cause of the non-uniform distribution of shock features in the 2-cm-tall experimental charges is likely due to shockwave attenuation as it passes through a heterogeneous, porous medium. As the shockwave collapses pores and compresses grains, energy is lost to the mechanical deformation of the sandstone charge. This

causes the shockwave to lose energy as it progresses through the charge, resulting in a distribution of shock metamorphic features that is non-uniform, whilst the porosity of the original charge is uniform (Fig. 8a).

Kowitz et al. (2013) dealt with the problem of non-uniform distribution of shock pressure at the thin section scale by only making observations of features in quartz from a region 5 mm in width and 300 μm in height in the top-centre of the sandstone charge. This strategy was an attempt to avoid complex interactions between the shockwave and the sample container which may have caused reverberation and magnification, resulting in shock deformation conditions that are not representative of the calculated applied pressure assigned to the sample.

In this study, evidence of reverberation is potentially present in at least one of the samples. The 15 GPa thin section (Fig. 39) contains one reidite-bearing grain at the bottom of the thin section, an uncharacteristic location for reidite-bearing grains across the suite, as well as four grains containing PDB in close proximity. This appears to indicate that there was shock-wave reverberation toward the bottom of the charge in this sample, as reidite was not observed anywhere near the bottom of the thin section in the other vertical sections.

5.2 – Onset of shock microstructures

The onset of shock metamorphic microstructures in zircon was progressive between the various pressure samples. PDB and PF are absent in the unshocked reference sample (0 GPa), and are present at the lowest shock pressure of 2.5 GPa, suggesting the onset of formation of PDB and PF in zircon is above 0 GPa and below or by 2.5 GPa in a sandstone with 25-30 vol% porosity (Fig. 41). Similarly, planar fractures were absent from zircon grains observed in BSE in the unshocked (0 GPa) reference sample, but they are present at 2.5 GPa, however their abundance was not observed to increase significantly with pressure – 5% of grains at 2.5 GPa; 6% of grains at 5 GPa; 5% of grains at 7.5 GPa; 1% of grains at 10 GPa; 5% of grains at 12.5 GPa; 0% of grains at 15 GPa and 2% of grains at 17.5 GPa (Figs. 41, 42).

Twins first appear in the 10 GPa sample, and show a systematic increase in abundance with increasing pressure (Figs. 41, 42). Twins were observed to form lamellar, polysynthetic sets in three out of the four samples shocked to greater than 10 GPa (Figs. 20, 25, 32). The twin sets show mostly similar morphology, with the apparent width of individual twin lamellae on polished surfaces less than 1 μm across. The twin domains are often associated with linear features in band contrast and texture component maps that connect or line up with twins identified by the special boundary function in Tango, suggesting that some twin lamellae may be below the minimum resolution of the EBSD map (50 nm) (i.e. Fig. 32). Well-formed twin sets were less common than irregular twin regions that comprised most of the twins identified (e.g. Fig. 23, Fig. 28). Additionally, sets of twins that appear to be lamellar and polysynthetic before being fractured and disaggregated were identified in the 17.5 GPa sample (Fig. 31). The fractured twins show evidence of lamellar features that were subsequently severely disrupted.

Reidite was first observed in the 10 GPa charge. The abundance of reidite increased from 10% of grains surveyed at 10 GPa, to 34% of grains at 12.5 GPa to 21% at 15 GPa and up to 40% at 17.5 GPa, indicating an overall trend of increasing percentage of reidite-bearing grains, with increasing calculated applied pressure. (Figs. 41, 42; Table 1).

The relative areal percentages of grains that were converted to reidite also appears to increase with pressure. In the 10 GPa sample, the largest example of domanial reidite was observed to be in an area comprising approximately 0.2% of the mapped grain (Figs. 21, 43a). In the 12.5 GPa sample, the largest example of domanial reidite is observed to be in an area comprising approximately 0.5% of the mapped grain (Figs. 26b, 43b). In the 15 GPa thin section, the zircon grain with the largest amount of reidite shows a portion converted to domanial reidite of approximately 4% of the mapped grain (Figs. 29, 43c). The 17.5 GPa sample has a zircon grain which represents the highest abundance of reidite formed within a single grain. A total of 6% of the zircon transformed to domanial reidite (Figs. 33, 43d). Collectively, there is a transition from a small fraction of reidite (0.2%) at 10 GPa to a significant portion of the mapped grain (6%) at 17.5 GPa (Fig. 43, 44).

The entire sample suite contained only two partially dissociated zircon grains, both of which are present in the 12.5 GPa sample (Figs. 22, 38). The initial position of the dissociated zircon grains may have influenced the fact that they partially dissociated, because they are located close to the initial propagation point of the shockwave indicating a post-shock temperature excursion of >1673 °C (Timms et al., 2017), which would be more intense close to the initial propagation point. This is also supported by the presence of reidite in one of the dissociated grains and other shock metamorphic features in proximity to the top of the thin section. Additionally, these two zircon grains may have been situated in an advantageous position next to a pore to allow for a larger than usual amount of pressure (and temperature) magnification (Güldemeister et al., 2013). However, the intensity of deformation in the final microstructure is too great to determine the initial setting of these zircon grains relative to pores and quartz grains.

5.2.1 - Progressive nature of microstructures with pressure

Microstructural abundances of features such as melt films and reidite were observed to increase progressively as a function of shock pressure (Table 1; Fig. 42). Planar fractures were not observed to increase significantly in abundance over the pressure range studied (2.5 to 17.5 GPa), as their abundance among samples appeared to be random 0-6% of grains in each sample (average 3.6). The abundances of melt films was observed to increase from 12% of zircon grains surveyed in the 7.5 GPa sample, to 34% in 10 GPa, to an average of 47% of grains between 12.5 GPa and 17.5 GPa. The increasing abundance of melt films appears to be linked to shock pressure. Reidite-bearing grains similarly were first found at 10% of grains in the 10 GPa sample, whilst the average number of grains partially converted to reidite increased to 32% for the 12.5 to 17.5 GPa samples. Additionally, the relative proportion of grains converted to reidite also increased pressure, with 10 GPa showing at most 0.2 % of a mapped grain converted to reidite, 12.5 GPa showed at

most 0.5 % converted to reidite. The 15 GPa sample showed a maximum of 4% of a grain converted to reidite, while the 17.5 GPa sample showed a portion of domanial reidite that comprised 6% of the mapped grain (Fig. 43).

Timms et al. (2017) predicted a progressive sequence of microstructures in zircon with pressure. A progressive sequence of microstructures appears to be what is represented in the studied samples (Fig. 42). There is a non-uniform distribution of microstructural features such as reidite, twins and PDB, and the apparent distribution of these features within the sample charges; i.e., reidite is always located toward the centre or top of the charge. An exception is one reidite-bearing grain that occurs at the bottom of the 15 GPa thin section, likely caused by shock-wave reverberation, with the distribution of twins and PDB extending further downward into the sample (Figs. 37, 38, 39, 40).

Twinning, PDB and dissociation of zircon do not appear to represent a progressive increase of abundance with pressure. Twins were observed in the 10 GPa sample, but the relative percentages of zircon grains bearing twins was not seen to significantly increase with pressure (Table 1). The number of zircon grains with PDB was also not observed to vary much with pressure, with an average of 10% of grains bearing PDB across all shocked samples. The sample bearing the fewest PDB (5 GPa) included only 2% of grains, while the sample bearing the most (17.5 GPa) had 15% of grains bearing PDB. Dissociation could not be analysed for progressive increases over pressures, as it was only present in the 12.5 GPa sample.

5.3 - Summary of zircon shock features, progression of features across samples, and comparison with previous research on shocked zircon

Orientation analysis of the 0 GPa (unshocked reference sample) thin section revealed zircon grains that were not significantly deformed, often possessing slightly different crystalline orientations in different parts of the grain which likely reflects mechanical fracturing as a result of sedimentary processes and diagenesis.

5.3.1 – PF

Planar fractures were not observed in the 0 GPa sample. However, fractures that appeared to be semi-planar but did not fulfill the criteria for identification of PF were observed (Fig. 11a). PF were first observed to be present in the 2.5 GPa sample. This suggests their formation in this sample suite occurred above 0 GPa and before or by 2.5 GPa (Fig. 11b). The abundance of planar fractures was not observed to systematically increase with pressure; rather their abundance decreased with increasing pressure (Figs. 41, 42).

5.3.2 - PDB

The PDB are present in the lowest shock pressure sample (2.5 GPa). Maximum misorientation across individual PDB found in the 2.5 GPa sample was 11°. Examples of PDB were observed at every shock pressure, with misorientations ranging from 4 to 12°. The magnitude of PDB misorientation was not observed to increase systematically with pressure, and the abundance of PDB-bearing grains remained relatively constant (Figs. 41, 42. Table 1).

PDB can form under ductile strain conditions (Kovaleva et al., 2015), however misorientations of 2.7° and below are characteristic of high P-T metamorphic environments (Kovaleva et al., 2015). The 11° of plastic deformation observed across PDB in zircon grains within the 2.5 GPa sample suggests that they were formed in a shock metamorphic environment (Montalvo et al., 2017). This supports the findings of Kovaleva et al. (2015) that the formation of PDB with misorientations of greater than 2.7° is not found in ductile strain conditions, and therefore only occurs in shock metamorphic environments. PDB in zircon were present in the lowest shock pressure sample, suggesting their formation threshold is above 0 GPa and before or by 2.5 GPa calculated applied pressure in sandstone with 25-30 vol% porosity. The misorientation magnitude of most PDB across the shocked sample suites (4-12°) also confirms that whilst PDB with very low angle (<2.7°) boundaries, such as those identified by Kovaleva et al. (2015) can form in 'tectonic' ductile strain conditions, PDB with greater degrees of deformation appear indicative of a shock metamorphic environments rather than tectonic conditions.

5.3.3 – Quenched silicate Melt Films

Melt films around zircon were observed first in the 7.5 GPa sample (Fig. 15), and their abundance increased from 12% at 7.5 GPa to between 34 and 53 % of grains by 10 GPa to 17.5 GPa (Figs. 41, 42; Table 1). The presence of melt films in the 7.5 GPa sample suggests that the post-shock temperatures required to melt surrounding minerals was reached above 5 GPa and before or by 7.5 GPa in sandstone with 25-30 vol% porosity.

5.3.4 - Twins

Mechanical {112} twins were observed to be present in zircon from 10 GPa to 17.5 GPa, which represents the first reported occurrence of twins in shock deformation experiments. The abundance of twins was not seen to vary significantly with sample pressure (Figs. 41, 42; Table 1), with one sample (15 GPa) showing only a pair of isolated twin lamellae (Fig. 28), whilst complex sets of twins were observed in the 10, 12.5 and 17.5 GPa samples (Figs. 20, 25, 32). Twin habits, as described in section 4, were observed to vary from isolated twin sections to sets of multiple twin lamellae. The presence of twins at 10 GPa suggests that the calculated applied shock pressure required to form mechanical twins in zircon is above 7.5 and before or by 10 GPa in sandstone with 25-30 vol% porosity.

Current understanding of the pressures required to produce mechanical twins in zircon is based on one empirical constraint, which suggests twins form at shock pressures of at least 20 GPa (Moser et al., 2011) and one static (diamond anvil cell) experiment, which showed twinning in a sample of zircon powder quenched at 20 GPa (Morozova et al., 2018) (Table 2). Results presented in this study represent the second ever experimental constraints on twinning in zircon, and the first example of producing twins in a dynamic shock-recovery experiment. These results show that the calculated applied pressure threshold for twinning in zircon may be lower than previously thought (i.e. 10 GPa compared to 20), for zircon in sandstone with 25-30 vol% porosity due to localised pressure amplification of 2-4 times the calculated applied pressure (Güldemeister et al; 2013).

.

5.3.5 - Reidite

Reidite was present starting at 10 GPa. Both the relative proportion of the analysed zircon grain converted to reidite, and the number of grains bearing reidite increases with pressure (Figs. 41, 42, 43; Table 1). As reidite was first identified at 10 GPa, this indicates that reidite formed at calculated applied pressures above 7.5 GPa and before or by 10 GPa.

Shock recovery experiments using thin zircon plates or zircon powder dynamically shocked to various pressures have shown that reidite can form at calculated applied shock pressures of >20 GPa (Kusaba et al., 1985; Leroux et al., 1999; Cavosie et al., 2015; Erickson et al., 2020) (Table 3). This study is the first dynamic shock-recovery experiment to produce reidite using natural rock samples as experimental charges. The results of this study provide additional constraints on the formation of reidite in zircon in sandstone with 25-30 vol% porosity, showing that reidite can be produced at lower calculated applied pressures in porous host rocks due to localised pressure amplification.

5.3.6 – Dissociation

Dissociation of zircon was only noted in two grains in the 12.5 GPa sample (Fig. 22). The presence of reidite in one of the grains in which dissociation was also present suggests that in addition to achieving the pressures required to form reidite, parts of those grains were also subjected to post-shock temperatures in excess of 1673 °C, the threshold at which zircon can dissociate into ZrO_2 and SiO_2 at 1 atm (Kleinmann, 1968; Kaiser et al., 2008; Timms et al., 2017). While such high temperatures are not expected to occur at a calculated applied shock pressure of 12.5 GPa in crystalline (nonporous) solids, localised temperature excursions of this magnitude have been predicted through mesoscale numerical modelling of shockwave propagation through porous materials (e.g. Davison et al., 2016).

5.3.7 – Apparent threshold pressures: {112} twins and reidite

The apparent threshold pressures (Fig. 47) for the formation of mechanical {112} twins and reidite, based on calculated applied pressures, appear to be significantly lower than what has been reported so far in previous research. Morozova et al. (2018) reported mechanical twins in zircon in a diamond anvil cell apparatus quenched at 20 GPa. Additionally, empirical observations of mechanical twins in zircon at Vredefort Dome by Moser et al. (2011) were interpreted as evidence that mechanical twins form at pressures of 20 GPa.

In this study, {112} twins appear to have formed at calculated applied pressures above 7.5 GPa and by 10 GPa in a shocked zircon-bearing sandstone of 25-30 vol% porosity (Table 2). It would appear that the apparent threshold pressure for formation of {112} twins in a rock of this porosity is at least 10 GPa lower than that inferred for naturally shocked crystalline rock (Moser et al., 2011; Timms et al., 2017).

Apparent threshold pressures for the formation of reidite in this study appears to overlap those for mechanical {112} twins within the experimental constraints, i.e.,

both microstructures are absent in the 7.5 GPa sample and present in the 10 GPa sample. Reidite was observed in the 10 GPa sample, suggesting it forms at calculated applied pressures above 7.5 GPa and by 10 GPa in zircon hosted in a sandstone of porosity 25-30 vol% (Table 2). It would appear that the apparent threshold pressure for formation of reidite in a rock of this porosity is at least 20 GPa lower than that reported for crystalline rock by Kusaba et al. (1985) and Leroux et al. (1999) (Table 3).

5.4 - Causes of non-uniform distribution of microstructures

The primary reason for the non-uniform distribution of microstructures across the sample charges as observed in the thin sections analysed in this study appears to be shockwave attenuation as a result of porosity and pore collapse.

Kieffer (1971) and Kieffer et al. (1976) describe porosity as causing shock wave rarefaction and reverberation at the pore scale, between pores and grains in shocked Coconino sandstone from Meteor Crater (Barringer Crater), USA. At the microstructural scale the shockwaves are ‘slowed down’ by their interaction with pores and grains, causing them to ‘stack up’ upon each other as they traverse a porous medium. This, in effect, causes a magnification of shock pressures which is a result of the passage of a shockwave through a heterogeneous, porous medium.

Kowitz et al. (2013; 2016) also describe the phenomena of shockwave reverberation and rarefaction on a microstructural scale, which has the result of producing shock features that would normally be expected at higher pressures (in a nonporous medium) in porous sandstones. Mesoscale numerical modelling conducted by Kowitz et al. (2013) shows that as a shock front passes through a porous medium, the shockwave becomes extremely heterogeneous at the pore-grain scale, with shock pressures locally magnified by up to four times (Fig. 45).

Güldemeister et al. (2013) conducted similar mesoscale numerical modelling (which Kowitz et al. (2013) based their mesoscale numerical models on). The modelling of single and multiple pores subjected to shock conditions showed that shock pressure could indeed reach up to four times bulk shock pressures as the shockwave passed through pore spaces (Fig. 46).

This essentially shows that a range of shock pressures can be reached locally when a shockwave passes through a porous, heterogeneous material, where locally the maximum pressure can significantly exceed the calculated applied pressure (Fig. 47). In contrast, when a homogenous, crystalline material experiences shock deformation the pressure response is generally uniform, and the maximum pressure is the same as calculated applied pressure (Fig. 47). Locally, pressure can be amplified on a pore-grain scale, producing localised shock effects that are indicative of much higher shock pressures than the calculated applied shock pressure (Fig. 47). Localised elevation of the maximum pressure above the calculated applied pressure in porous rocks explains how certain shock metamorphic features can form at lower calculated applied shock pressure than their established apparent threshold pressure (Fig. 47). The difference between the shock response of a porous and nonporous medium, and the effect in regard to the formation of features for which the

apparent threshold pressure is greater than the calculated applied pressure the porous medium was subjected to is illustrated in Figure 47.

It was noted that in some vertical sections, towards the bottom, there were dome-shaped areas of relatively less shock fracturing and brecciation (Fig. 48), and shock deformation (presence of shock metamorphic features in zircon) (Figs. 36, 38, 40). This may be due to a 'shock shadow' effect wherein the shockwave intensity attenuates toward the bottom of the sample. Another possibility may be shockwave reflection from the base plate and interference with the primary shock wave that results in an area of less intensity, or some combination of both of these phenomena.

5.5 - A new shock stage classification for zircon in porous sandstone

Kowitz et al. (2013; 2016) proposed a classification scheme for shock stages of porous sandstone (Fig. 5b). This differs significantly from the classification of nonporous, crystalline rocks (Fig. 4). The study of shock features in zircon in this study is based upon the same sample suite (meaning, the same thin sections) that Kowitz et al. (2013; 2016) used to define the new classification shock stages in porous sandstones.

The first shock stage classification of zircon is here presented based on the systematic responses of zircon to shock conditions in porous sandstone (25-30 vol% porosity) from 2.5 to 17.5 GPa (Table 4). This pressure range represent shock stages 0 to 4 in the shock classification scheme of porous sandstones proposed by Kowitz et al. (2016). Also incorporated into the shock stage classification of zircon are previously published results for the shock response of zircon in shock stage 5 (100% vesicular glass) in Coconino sandstone from Meteor Crater (Cavosie et al., 2016).

Zircon in shock stage 0 (unshocked) rocks does not show any diagnostic shock metamorphic phenomena. Shock stage 0 zircons are commonly fractured, but not in a systematic way (Figs. 10, 11a). Zircon in shock stage 1a (<1.5 GPa calculated applied pressure) were not evaluated in this study. Zircon in shock stage 1b (2.5 to 5 GPa calculated applied pressure) represents the first appearance of PF (Figs. 11b, 11c) and PDB (Figs. 13 and 15) in zircon. Shock stage 1c (7.5 GPa calculated applied pressure) is a new shock stage classification subdivision proposed here, that represents formation of quenched silicate melt films around the periphery of zircon grains (Fig. 16). In addition, zircon in shock stage 1c rocks also have PF (Fig. 11d) and PDB (Fig. 17).

Shock stages 2 to 4 represent profound changes in the shock response of zircon, due to the formation of diagnostic shock microstructures. In addition to PF and PDB, the diagnostic microstructures include {112} mechanical twins and the high-pressure polymorph reidite which are found in rocks from shock stage 2 through 4. Examples of zircon microstructures in shock stage 2 (10-12.5 GPa calculated applied pressure) include {112} twins (Figs. 20, 25) and reidite (Figs. 25 and 26). Examples of zircon microstructures in shock stage 3 (15 GPa calculated applied pressure) include {112} twins (Fig. 28) and reidite (Fig. 29). Examples of zircon microstructures in shock

stage 4 (17.5 GPa calculated applied pressure) include {112} twins (Figs. 31, 32) and reidite (Fig. 33).

The presence of partial dissociation of zircon was observed in shock stage 2 (12.5 GPa calculated applied pressure). Dissociation of zircon in the 12.5 GPa sample was not found to be progressive, as it was not observed in any other samples. Therefore, the new shock stage scheme for zircon presented here (Table 4) does not include dissociation.

Zircon in shock stage 5 porous sandstone was not included in this study. However, the shock behaviour of zircon in shock stage 5 Coconino sandstone (100% vesicular glass) by Cavosie et al. (2016) provides an example of the response of zircon in shock stage 5 sandstone and is included in Table 4.

The new shock stage scheme for zircon has implications for studies of zircon in porous target rocks, such as at the Rock Elm impact structure, where reidite was reported in sandstone (Cavosie et al., 2015), at Meteor Crater where FRIGN zircon was reported in shock stage 5 sandstone by (Cavosie et al., 2016), and at Kamil crater where shock-twinned zircon was reported in shock stage 3 sandstone (Cavosie et al., 2021). These examples, as well as other impact sites where zircon has been identified in a host that was originally porous show that further investigation may be required when reconstructing the shock metamorphic pressures that zircon was exposed to at (porous) impact sites. Further research that may prove beneficial would be the study of the shock response of zircon in sandstones of lower porosity than that studied here to provide a finer calibration of shock response (for example, > 0 vol% porosity and < 25 vol% porosity sandstones), to ‘fill in the gaps’ and provide a continuous shock stage scheme for zircon hosted in rocks over a range of porosities. The results of this research may be applied to terrestrial porous target rocks such as sedimentary host rocks, and non-terrestrial porous environments, such as Lunar regolith and other high-porosity target environments in the solar system such as asteroids which have a loose regolith.

6 – Conclusion

The systematic analysis of zircon hosted in Seeberger sandstone with initial 25-30 vol% porosity, shocked to calculated applied pressures of 2.5 to 17.5 GPa at 2.5 GPa intervals, has shown a progression of shock metamorphic features in zircon hosted in a high-porosity sandstone across a range of pressures.

This analysis allowed for the identification of features including PF, PDB, melt films, {112} mechanical twinning, the high-pressure zircon polymorph reidite and isolated examples of dissociation of zircon. Of these features, only reidite, twins and melt films showed a systematic increase in abundance with increasing shock pressure (at or above 7.5 GPa) applied to the sandstone samples. This study represents the first ever study to document twinning in zircon in shock deformation experiments, and the first to provide experimental constraints for the formation conditions of reidite, twinning and dissociation in zircon in porous target rocks.

The discovery of reidite at calculated applied shock pressures as low as 10 GPa is significant, as reidite is not thought form at such low shock metamorphic pressures (typically in crystalline host rocks it is expected to form at calculated applied shock pressures of 30 GPa) (Kusaba et al., 1985; Leroux et al., 1999). The hypothesis for the presence of reidite at lower-than-expected calculated applied pressures is attributed to microscale spatial heterogeneity in pressure (and post-shock temperature), as described by Kowitz et al. (2013), Güldemeister et al. (2013) and Davison et al. (2016). The localised pressure magnifications (and reductions) generate maximum shock pressures on the microscale that are high enough to allow the formation of high-pressure features in zircon such as {112} mechanical twinning and reidite, which necessitated a re-evaluated shock stage classification for zircon in porous target rocks.

A new shock stage classification for zircon hosted in porous (25-30 vol%) sandstone is presented here, based on the same samples used to establish a shock stage scheme for porous rocks based on progressive deformation of quartz. Shock stages 1a, 1b and 1c represent calculated applied pressures from <1.5 GPa to 7.5 GPa, which includes shock metamorphic features for zircon such as PF, PDB and melt films. Shock stages 2, 3 and 4 represent calculated applied pressures from 10 GPa to 17.5 GPa, and include shock metamorphic features for zircon that include mechanical {112} twins and reidite. Shock stage 5 represents calculated applied pressures of > 18 GPa and includes near complete rock melting and the formation of granular microstructures in zircon (Cavosie et al., 2016).

7 - References

Bohor, B.F., Betterton, W.J., Krogh, T.E., 1993. Impact-shocked zircons: discovery of shock-induced textures reflecting increasing degrees of shock metamorphism. Earth and Planetary Science Letters 119, 419–424. https://doi.org/10.1016/0012-821X(93)90149-4

Cavosie, A.J., Quintero, R.R., Radovan, H.A., Moser, D.E., 2010. A record of ancient cataclysm in modern sand: Shock microstructures in detrital minerals from the Vaal River, Vredefort Dome, South Africa. Geological Society of America Bulletin 122, 1968–1980.

Cavosie, A., Erickson, T., Timms, N., 2015. Nanoscale records of ancient shock deformation: Reidite ($ZrSiO_4$) in sandstone at the Ordovician Rock Elm impact crater. Geology 43, 315–318. https://doi.org/10.1130/G36489.1

Cavosie, A.J., Erickson, T.M., Timms, N.E., Reddy, S.M., Talavera, C., Montalvo, S.D., Pincus, M.R., Gibbon, R.J., Moser, D., 2015b. A terrestrial perspective on using ex situ shocked zircons to date lunar impacts. Geology 43, 999–1002.

Cavosie, A.J., Timms, N.E., Erickson, T.M., Hagerty, J.J., Hörz, F., 2016. Transformations to granular zircon revealed: Twinning, reidite and ZrO_2 in shocked zircon from Meteor Crater (Arizona, USA). Geology 44, 703-706. https://doi.org/doi:10.1130/G38043.1

Cavosie, A.J., Timms, N.E., Ferrière, L., Rochette, P., 2018. FRIGN zircon—The only terrestrial mineral diagnostic of high-pressure and high-temperature shock deformation. Geology 46, 891–894.

Cavosie, A.J., Folco, L., 2021. Shock-twinned zircon in ejecta from the 45-m-diameter Kamil crater in southern Egypt. Geological Society of America Special Paper 550, 419-432. https://doi.org/10.1130/2021.2550(17)

Cox, M.A., Cavosie, A.J., Bland, P.A., Miljković, K., Wingate, M.T.D., 2018. Microstructural dynamics of central uplifts: Reidite offset by zircon twins at the Woodleigh impact structure, Australia. Geology 46, 983–986. https://doi.org/10.1130/G45127.1

Davison, T.M., Collins, G.S., Bland, P.A., 2016. Mesoscale Modeling of Impact Compaction of Primitive Solar System Solids. Astrophysical Journal 821, 68. https://doi.org/10.3847/0004-637X/821/1/68

Deutsch, A., Schärer, U., 1990. Isotope systematics and shock-wave metamorphism: I. U-Pb in zircon, titanite and monazite, shocked experimentally up to 59 GPa. Geochimica et Cosmochimica Acta 54, 3427–3434. https://doi.org/10.1016/0016-7037(90)90295-V

Erickson, T.M., Cavosie, A.J., Moser, D.E., Barker, I.R., Radovan, H.A., 2013. Correlating planar microstructures in shocked zircon from the Vredefort Dome at multiple scales: Crystallographic modeling, external and internal imaging, and EBSD structural analysis. American Mineralogist 98, 53–65.

Erickson, T.M., Cavosie, A.J., Pearce, M.A., Timms, N.E., Reddy, S.M., 2016.

Empirical constraints on shock features in monazite using shocked zircon inclusions. Geology 44, 635–638.

Erickson, T., Pearce, M., Reddy, S., Timms, N., Cavosie, A., Bourdet, J., Rickard, W., Nemchin, A., 2017. Microstructural constraints on the mechanisms of the transformation to reidite in naturally shocked zircon. Contributions to Mineralogy and Petrology 172, 1–26. https://doi.org/10.1007/s00410-016-1322-0

Farnan, I., Balan, E., Pickard, C.J., Mauri, F., 2003. The effect of radiation damage on local structure in the crystalline fraction of $ZrSiO_4$: investigating the ^{29}Si NMR response to pressure in zircon and reidite. American Mineralogist 88, 11–12.

French, B.M., 1998. Traces of catastrophe: A handbook of shock-metamorphic effects in terrestrial meteorite impact structures. Technical Report, Lunar and Planetary Institute Contribution 954.

French, B.M., Koeberl, C., 2010. The convincing identification of terrestrial meteorite impact structures: What works, what doesn't, and why. Earth-Science Reviews 98, 123–170. https://doi.org/10.1016/j.earscirev.2009.10.009

Glass, B.P., Liu, S., 2001. Discovery of high-pressure ZrSiO4 polymorph in naturally occurring shock-metamorphosed zircons. Geology 29, 371–373.

Glass, B.P., Liu, S., Leavens, P.B., 2002. Reidite: An impact-produced high-pressure polymorph of zircon found in marine sediments. American Mineralogist 87, 562–565.

Grieve, R.A.F., Langenhorst, F., Stöffler, D., 1996. Shock metamorphism of quartz in nature and experiment: II. Significance in geoscience*. 31(1), 6-35. https://doi.org/10.1111/j.1945-5100.1996.tb02049.x

Güldemeister, N., Wünnemann, K., Durr, N., Hiermaier, S., 2013. Propagation of impact-induced shock waves in porous sandstone using mesoscale modeling. Meteoritics and Planetary Science 48, 115–133. https://doi.org/10.1111/j.1945-5100.2012.01430.x

Hauser, N., Reimold, W.U., Cavosie, A.J., Crósta, A.P., Schwarz, W.H., Trieloff, M., Da Silva Maia de Souza, C., Pereira, L.A., Rodrigues, E.N., Brown, M., 2019. Linking shock textures revealed by BSE, CL, and EBSD with U-Pb data (LA-ICP-MS and SIMS) from zircon from the Araguainha impact structure, Brazil. Meteoritics and Planetary Science 54, 2286–2311.

Hazen, R.M., Finger, L.W., 1979. Crystal structure and compressibility of zircon at high pressure. American Mineralogist 64, 196–201.

Kaiser, A., Lobert, M., Telle, R., 2008. Thermal stability of zircon (ZrSiO4). Journal of the European Ceramics Society 28, 2199–2211. https://doi.org/10.1016/j.jeurceramsoc.2007.12.040

Kenkmann, T., Wünnemann, K., Deutsch, A., Poelchau, M.H., Schäfer, F., Thoma, K., 2011. Impact cratering in sandstone: The MEMIN pilot study on the effect of pore water. Meteoritics and Planetary Science 46, 890–902. https://doi.org/https://doi.org/10.1111/j.1945-5100.2011.01200.x

Kenkmann, T., Deutsch, A., Thoma, K., Ebert, M., Poelchau, M.H., Buhl, E., Carl, E.-R., Danilewsky, A.N., Dresen, G., Dufresne, A., Durr, N., Ehm, L., Grosse, C., Gulde, M., GÜldemeister, N., Hamann, C., Hecht, L., Hiermaier, S., Hoerth, T., Kowitz, A., Langenhorst, F., Lexow, B., Liermann, H.-P., Luther, R., Mansfeld, U., Moser, D., Raith, M., Reimold, W.U., Sauer, M., Schäfer, F., Schmitt, R.T., Sommer, F., Wilk, J., Winkler, R., Wünnemann, K., 2018. Experimental impact cratering: A summary of the major results of the MEMIN research unit. Meteoritics and Planetary Science 53, 1543–1568. https://doi.org/10.1111/maps.13048

Kenny, G.G., Morales, L.F., Whitehouse, M.J., Petrus, J.A., Kamber, B.S., 2017. The formation of large neoblasts in shocked zircon and their utility in dating impacts. Geology 45, 1003–1006.

Kieffer, S.W., 1971. Shock metamorphism of the Coconino sandstone at Meteor Crater, Arizona. Journal of Geophysical Research 76, 5449–5473.

Kieffer, S.W., Phakey, P.P., Christie, J.M., 1976. Shock processes in porous quartzite: Transmission electron microscope observations and theory. Contributions to Mineralogy and Petrology 59, 41–93.

Kleinmann, B., 1968. The breakdown of zircon observed in the Libyan desert glass as evidence of its impact origin. Earth and Planetary Science Letters 5, 497–501. https://doi.org/10.1016/s0012-821x(68)80085-8

Kovaleva, E., Klötzli, U., Habler, G., Wheeler, J., 2015. Planar microstructures in zircon from paleo-seismic zones. American Mineralogist 100, 1834. https://doi.org/10.2138/am-2015-5236

Kowitz, A, Guldemeister, N., Reimold, W.U., Schmitt, R.T., Wunnemann, K., 2013. Diaplectic quartz glass and SiO_2 melt experimentally generated at only 5 GPa shock pressure in porous sandstone: Laboratory observations and meso-scale numerical modeling. Earth and Planetary Science Letters 384, 17. https://doi.org/10.1016/j.epsl.2013.09.021

Kowitz, Astrid, Schmitt, R.T., Uwe Reimold, W., Hornemann, U., 2013. The first MEMIN shock recovery experiments at low shock pressure (5–12.5 GPa) with dry, porous sandstone. Meteoritics and Planetary Science 48, 99–114. https://doi.org/10.1111/maps.12030

Kowitz, A., Güldemeister, N., Schmitt, R.T., Reimold, W., Wünnemann, K., Holzwarth, A., 2016. Revision and recalibration of existing shock classifications for quartzose rocks using low-shock pressure (2.5–20 GPa) recovery experiments and mesoscale numerical modeling. Meteoritics and Planetary Science 51, 1741–1761. https://doi.org/10.1111/maps.12712

Kusaba, K., Syono, Y., Kikuchi, M., Fukuoka, K., 1985. Shock behavior of zircon: phase transition to scheelite structure and decomposition. Earth and Planetary Science Letters 72, 433–439. https://doi.org/10.1016/0012-821X(85)90064-0

Leroux, H., Reimold, W.U., Koeberl, C., Hornemann, U., Doukhan, J.C., 1999. Experimental shock deformation in zircon: a transmission electron microscopic study. Earth and Planetary Science Letters 169, 291–301. https://doi.org/10.1016/S0012-821X(99)00082-5

Melosh, H.J., 1989. Impact cratering: A geologic process. New York, Oxford University Press; Oxford. Clarendon Press.

Montalvo, S., Cavosie, A., Erickson, T., Talavera, C., 2017. Fluvial transport of impact evidence from cratonic interior to passive margin: Vredefort-derived shocked zircon on the Atlantic coast of South Africa. American Mineralogist 102, 813–823. https://doi.org/10.2138/am-2017-5857CCBYNCND

Morozova, I., Shieh, S.R., Moser, D.E., Barker, I.R., Hanchar, J.M., 2018. Strength and Deformation of Zircon at Crustal and Mantle Pressures. Microstructural Geochronology; Planetary Records Down to Atom Scale 232, 167-182.

Moser, D.E., Cupelli, C.L., Barker, I.R., Flowers, R.M., Bowman, J.R., Wooden, J., Hart, J.R., 2011. New zircon shock phenomena and their use for dating and reconstruction of large impact structures revealed by electron nanobeam (EBSD, CL, EDS) and isotopic U-Pb and (U-Th)/He analysis of the Vredefort dome Canadian Journal of Earth Science 48, 117–139. https://doi.org/10.1139/E11-011

Piazolo, S., Austrheim, H., Whitehouse, M., 2012. Brittle-ductile microfabrics in naturally deformed zircon: Deformation mechanisms and consequences for U-Pb dating. American Mineralogist 97, 1544–1563. https://doi.org/10.2138/am.2012.3966

Poelchau, M. H., & Kenkmann, T. (2011). Feather features: A low-shock-pressure indicator in quartz. Journal of Geophysical Research: Solid Earth, 116(B2), 1-13.

Rasmussen, C., Stockli, D. F., Erickson, T. M., & Schmieder, M. (2020). Spatial U-Pb age distribution in shock-recrystallized zircon–A case study from the Rochechouart impact structure, France. Geochimica et Cosmochimica Acta 273, 313-330.

Reddy, S.M., Timms, N.E., Hamilton, P.J., Smyth, H.R., 2009. Deformation-related microstructures in magmatic zircon and implications for diffusion. Contributions to Mineralogy and Petrology 157, 231–244.

Reid, A.F., Ringwood, A.E., 1969. Newly observed high pressure transformations in Mn_3O_4, $CaAl_2O_4$, and $ZrSiO_4$. Earth and Planetary Science Letters 6, 205–208. https://doi.org/10.1016/0012-821X(69)90091-0

Rimša, A., Whitehouse, M.J., Johansson, L., Piazolo, S., 2007. Brittle fracturing and fracture healing of zircon: An integrated cathodoluminescence, EBSD, U-Th-Pb, and REE study. American Mineralogist 92, 1213–1224. https://doi.org/10.2138/am.2007.2458

Schaltegger, U., Ulianov, A., Müntener, O., Ovtcharova, M., Peytcheva, I., Vonlanthen, P., Vennemann, T., Antognini, M., Girlanda, F., 2015. Megacrystic zircon with planar fractures in miaskite-type nepheline pegmatites formed at high pressures in the lower crust (Ivrea Zone, southern Alps, Switzerland). American Mineralogist 100, 83–94. https://doi.org/10.2138/am-2015-4773

Schmieder M, Tohver E, Jourdan F, Denyszyn SW, Haines PW. Zircons from the Acraman impact melt rock (South Australia): shock metamorphism, U–Pb and

40Ar/39Ar systematics, and implications for the isotopic dating of impact events. Geochimica et Cosmochimica Acta. 2015 Jul 15;161:71-100.

Stöffler, D., 1971. Progressive metamorphism and classification of shocked and brecciated crystalline rocks at impact craters. Journal of Geophysical Research 76, 5541–5551. https://doi.org/doi:10.1029/JB076i023p05541

Stöffler, D., Langenhorst, F., 1994. Shock metamorphism of quartz in nature and experiment: I. Basic observation and theory. Meteoritics and Planetary Science 29, 155–181.

Timms, N.E., Reddy, S.M., Healy, D., Nemchin, A.A., Grange, M.L., Pidgeon, R.T., Hart, R., 2012. Resolution of impact-related microstructures in lunar zircon: A shock-deformation mechanism map. Meteoritics and Planetary Science 47, 120–141. https://doi.org/10.1111/j.1945-5100.2011.01316.x

Timms, N.E., Erickson, T.M., Pearce, M.A., Cavosie, A.J., Schmieder, M., Tohver, E., Reddy, S.M., Zanetti, M.R., Nemchin, A.A., Wittmann, A., 2017. A pressure-temperature phase diagram for zircon at extreme conditions. Earth-Science Reviews 165, 185–202. https://doi.org/10.1016/j.earscirev.2016.12.008ea

Timms, N.E., Healy, D., Erickson, T.M., Nemchin, A.A., Pearce, M.A., Cavosie, A.J., 2018. Role of elastic anisotropy in the development of deformation microstructures in zircon. Microstructural Geochronology: Planetary Records Down to Atom Scale, 183–202.

Wittmann, A., Kenkmann, T., Schmitt, R.T., Stöffler, D., 2006. Shock-metamorphosed zircon in terrestrial impact craters. Meteoritics and Planetary Science 41, 433–454. https://doi.org/10.1111/j.1945-5100.2006.tb00472.x

8 – Figure Captions

Figure 1. Photograph of an impact crater, and generalised schematic diagram of shock metamorphic effects in impact craters. **(A)** Aerial photo of Barringer crater (also known as Meteor crater) in Arizona, United States. Photo credit D. Roddy (USGS). **(B)** Generalised schematic diagram of an asteroid impact event, showing shock pressures (left) and shock deformation features typically induced in rocks (right). Adapted from (French, 1998).

Figure 2. Schematic diagram of shock metamorphic features in zircon. From Timms et al. (2017). Zrn = Zircon, Reid = reidite.

Figure 3. Shock calibration scheme for quartz in porous sandstones and cross-sections of porous Seeberger sandstone charges shocked from 2.5 to 17.5 GPa. **(A)** Shock calibration scheme for porous rocks (Kowitz et al., 2016) (modified). Seeberger Sandstone L3 is highlighted in blue, it has a porosity of 25-30 vol.%, and is the sample suite analysed in this study. Note the shock metamorphic effects (black dashed lines representing relative volume of diaplectic quartz glass, SiO_2 melt and high-pressure phases) versus pressure (X-axis) and porosity (Y-axis) indicating that an increase in porosity directly (and inversely) influences the pressure at which shock metamorphic features form. The squares, triangles and diamonds represent other rounds of shock recovery experiments conducted by MEMIN at different porosities, which are not used in this study. L3 = Layer 3. **(B)** Thin section scans of cross sections from the SST L3 (25-30 vol% porosity) charges shocked to various pressures. (Modified after Kowitz et al., 2016). Note the compaction of the charges steadily increases with pressure. SST L3 = Seeberger sandstone layer 3.

Figure 4. Shock stage classification scheme for quartzo-feldspathic rocks. Originally proposed by Stöffler (1971), modified by Kowitz et al. (2016).

Figure 5. Shock stage classification schemes for sandstone. **(A)** Shock stage classification scheme for porous sandstones, based on empirical observations conducted by Kieffer (1971) and Kieffer et al. (1976). **(B)** New shock stage classification scheme for dry, porous sandstone based on experimental observations of laboratory shocked sandstone samples Kowitz et al. (2016).

Figure 6. Schematic diagram of the high-explosive apparatus used to shock the sandstone charge. Note the flyer plate, which is accelerated to speeds in excess of 1km/s by a high explosive charge. The moving flyer plate impacts on the driver plate, transferring the force into the sandstone cylinder which is encased in an ARMCO iron container to ensure sample cohesion. Adapted from Kowitz et al. (2013).

Figure 7. Idealised diagram of the sandstone charges showing how thin sections were cut from them. The vertical rectangle section represents all but the 10 GPa thin

section, which is a horizontal ‘crescent’ shape. The shockwave propagation point is at the top centre of the charge.

Figure 8. BSE images of shocked Seeberger sandstone thin sections. Shock pressures show the increase in fracturing and deformation of the charges as pressure increases. **(A)** Unshocked reference sample (0 GPa) thin section (vertical rectangular section). The shape of the thin section represents an undeformed charge. **(B)** 2.5 GPa thin section (vertical rectangular section). Fractures connect the top left to the bottom right corners of the thin section, and the vertical compaction. **(C)** 5 GPa thin section (vertical rectangular section). Fracture prevalence across the thin section has increased. **(D)** 7.5 GPa thin section (vertical rectangular section). Fractures connect all four corners of the thin section, as well as further vertical compaction. **(E)** 10 GPa thin section (horizontal ‘crescent’ section). Concentric, ring-shaped fractures appear to radiate out from the centre of the charge. **(F)** 12.5 GPa thin section (vertical rectangular section). Fractures that connect the corners of the thin section have developed into zones of comminution and brecciation, a crescent shaped area at the bottom of the thin section appears to be less deformed. Compaction of the charge has progressed, with the width and height being approximately the same. **(G)** 15 GPa thin section (vertical rectangular section). Fractures are difficult to observe and appear to have transitioned to broad zones of comminution that take up almost all of the sample, but a small crescent of less deformed sandstone is present at the bottom edge. Compaction has also progressed, with the sample appearing wider than it is taller. The white lens at the top of the thin section is iron from the sample container. **(H)** 17.5 GPa thin section (vertical rectangular section). Fractures are difficult to observe, most of the sample is highly fractured and comminuted, the bottom section shows more deformation than in the other thin sections. Compaction has further progressed, with the top surface of the sample now concave and its width greater than its height.

Figure 9. Microstructure of the shocked Seeberger sandstone charges showing progressive deformation. **(A)** BSE image of the microstructure in the unshocked reference sample (0 GPa) thin section. Primary pore space is preserved, and grains appear to be undeformed. **(B)** BSE image of the microstructure in the 2.5 GPa thin section. Primary porosity has been completely removed, and grains appear to be fractured and forced together. **(C)** BSE image of the microstructure in the 5 GPa thin section. Primary porosity is absent, while fracturing in grains seems to have produced some secondary porosity. **(D)** BSE image of the microstructure in the 7.5 GPa thin section. Primary pore space is absent, while the progression of fracturing has led to an increase in secondary porosity compared to 2.5 and 5 GPa thin sections. **(E)** BSE image of the microstructure in the 10 GPa thin section. Primary porosity is absent, increased fracture density has led to more secondary porosity than the 7.5 GPa thin section. **(F)** BSE image of the microstructure in the 12.5 GPa thin section. Primary porosity is absent, but increased fracturing and comminution of the sandstone has resulted in increased secondary porosity compared to the 10 GPa thin section. **(G)** BSE image of the microstructure in the 15 GPa thin section. Primary

porosity is absent, and fracturing and comminution has progressed from the 12.5 GPa thin section, resulting in increased secondary porosity.
(H) BSE image of the microstructure in the 17.5 GPa thin section. Primary porosity is absent, whilst fracture density is similar to the 15 GPa thin section.

Figure 10. Zircon grains from the unshocked reference sample (0 GPa) thin section. **(A)** BSE image of zircon #1 in the 0 GPa thin section. Non-planar fractures are apparent around the majority of the grain. **(B)** BSE image of zircon #25 in the 0 GPa thin section. Non-planar fractures cross most of the grain, with a portion of the zircon grain appearing to have detached. **(C)** BSE image of zircon #15 in the 0 GPa thin section. Non-planar fractures is limited, with slight evidence of fractures visible across the grain, this grain is relatively undeformed. **(D)** BSE image of zircon #14 in the 0 GPa thin section. Non-planar fractures are limited to the bottom right portion of the grain, with the remainder of the grain relatively undeformed.

Figure 11. BSE images of planar fractures in zircon grains from the Seeberger sandstone suite analysed. **A.** Zircon in the unshocked reference sample with planar microstructures. **B.** Zircon in the 2.5 GPa thin section with two sets of planar fractures. **C.** Zircon in the 5 GPa thin section showing one set of PF. **D.** Zircon in the 7.5 GPa thin section with two sets of planar fractures. **E.** Zircon in the 10 GPa thin section showing one set of PF. **F.** Zircon in the 12.5 GPa thin section with two sets of planar fractures. **G.** Zircon in the 17.5 GPa thin section showing one set of PF.

Figure 12. Orientation map of a representative zircon in the 0 GPa thin section. Crystallographic misorientation is limited to 5° across the grain, with misoriented areas appearing to be areas that have fractured. BC = Band contrast, TC = Texture component, Step = step size.

Figure 13. Example of a planar deformation band (PDB) in the 2.5 GPa thin section. Note the inset region that shows a PDB with misorientation of 12° and the associated misorientation profile. BC = Band contrast, TC = Texture component, Step = step size, PDB = planar deformation band.

Figure 14. Example of a relatively undeformed zircon in the 5 GPa thin section. **(A)** BSE image of zircon #9 showing a lack of significant non-planar fracturing. **(B)** Band contrast and texture component EBSD map of zircon #9 showing no crystal plastic deformation across the majority of the grain, whilst the bottom right corner shows around 5° of misorientation. This corner is also facing toward the shockwave. BC = Band contrast, TC = texture component.

Figure 15. Example of zircon with a PDB in the 5 GPa thin section. The top of the grain (inset) possesses a well-formed PDB set with misorientations approaching 10°. BC = band contrast, TC = texture component, PDB = planar deformation band.

Figure 16. Example of melt films adjacent to zircon in the 7.5 GPa thin section. Quenched silicate melt film is present on the periphery of the grain, the 7.5 GPa thin

section is the lowest pressure sample at which quenched silicate melt film is present around zircon grains.

Figure 17. Example of zircon with a PDB in the 7.5 GPa thin section. A single PDB is present within this grain, with misorientation across the band of around 12°. BC = band contrast, TC = texture component, PDB = planar deformation band.

Figure 18. Example of zircon with a PDB in the 10 GPa thin section. Texture component reveals the presence of a single wedge-shaped PDB. The misorientation profile shows that the PDB has a misorientation of 10°. BC = band contrast, TC = texture component, PDB = planar deformation band.

Figure 19. Example of zircon with two PDB sets in the 10 GPa thin section. Two sets of intersecting PDB are revealed by texture component, whilst misorientation profiles shows that misorientation in the first set is at most 6°, whilst misorientation in the second set is at most 4.4°. BC = band contrast, TC = texture component, PDB = planar deformation band.

Figure 20. Example of zircon with {112} twin lamellae in the 10 GPa thin section, and the associated pole figure which shows a set of well-formed twins.
(A) Band contrast, texture component and special boundary map of zircon #36. A closely spaced set of twins is apparent in the inset portion of the image, with their boundaries highlighted in yellow. BC = band contrast, TC = texture component, SB = special boundary. **(B)** Pole figure with data points from the inset image from (A). The data points from the twin data points (orange) show a 65° misorientation around {110} from the host grain (blue-green). n = number of data points in pole figure.

Figure 21. Example of reidite-bearing zircon in the 10 GPa sample. A small portion of domanial reidite (red) is apparent on the edge of the zircon grain (green). BC = band contrast.

Figure 22. Example of partially dissociated zircon in the 12.5 GPa sample revealed in BSE. The inset region shows fragmented portion of the zircon grain that have dissociated around their margins, surrounded by a quenched silicate melt film.

Figure 23. Example of zircon with {112} twins and two PDB sets in the 12.5 GPa thin section. Two sets of PDB in different orientations are visible in the left most corner of the grain, whilst a twin is seen near the top-centre of the grain. BC = band contrast, TC = texture component, SB = special boundary, PDB = planar deformation band.

Figure 24. Example of zircon with {112} twins in the 12.5 GPa thin section. BC = band contrast, IPFx = inverse pole figure (x), SB = special boundary. **(A)** Band contrast and inverse pole figure (x) EBSD map of the entire grain. The white box containing the twin is shown in (B). BC = band contrast, IPFx = inverse pole figure (x). **(B)** Band contrast, inverse pole figure (x) and special boundary EBSD map of the box shown in (A). A very thin (<0.25 μm) isolated twin is shown by the green sliver,

highlighted in yellow. BC = band contrast, IPFx = inverse pole figure (x), SB = special boundary.

Figure 25. Example of zircon with {112} twins and reidite in the 12.5 GPa sample. BC = band contrast, IPFx = inverse pole figure (x), TC = texture component, SB = special boundary. **(A)** Band contrast and inverse pole figure (x) EBSD map of the entire zircon grain, showing the regions highlighted in (B) and (C). BC = band contrast, IPFx = inverse pole figure (x). **(B)** Band contrast, texture component and special boundary map of the top portion of the grain. A well-formed set of twin lamellae is shown. BC = band contrast, TC = texture component, SB = special boundary. **(C)** Band contrast and phase map of an area in the middle-left of zircon #26. A portion of domainal reidite is highlighted in red, while the host zircon is green. BC = band contrast.

Figure 26. Zircon grains with reidite in the 12.5 GPa sample showing two different forms of reidite. BC = band contrast. **(A)** Band contrast and phase EBSD map of zircon #50 showing a portion of tabular or lens-shaped reidite (red) surrounded by zircon (green). BC = band contrast. **(B)** Band contrast and phase EBSD map of zircon #25 showing a region of domanial reidite (red) surrounded by zircon (green). BC = band contrast.

Figure 27. Zircon with two PDB sets in the 15 GPa thin section. Two sets of intersecting PDB, each with a misorientation of <5°, are visible in texture component. BC = band contrast, TC = texture component, PDB = planar deformation band.

Figure 28. Zircon with {112} twins and reidite in the 15 GPa sample. This grain was the only zircon observed to possess twins in the entire thin section. Also present in this zircon is reidite (purple). BC = band contrast, TC = texture component, SB = special boundary.

Figure 29. Reidite-bearing zircon in the 15 GPa thin section. A portion of domanial reidite (red) is visible at the bottom portion of the zircon grain (green). BC = band contrast.

Figure 30. Example of zircon with a PDB in the 17.5 GPa thin section. A PDB set is visible in the bottom half of the grain, with individual misorientations in the set of a maximum of 12°. BC = band contrast, TC = texture component, PDB = planar deformation band.

Figure 31. Disaggregated zircon with {112} twins in the 17.5 GPa thin section. Two regions of twins are present at the top and bottom of the main grain. The twinned portions appear to be physically disrupted and disaggregated. BC = band contrast, IPFx = inverse pole figure (x), SB = special boundary.

Figure 32. Zircon with {112} twins and reidite in the 17.5 GPa thin section. The whole grain reveals an area of domanial reidite (aqua), as well as twins on the

bottom portion of the grain, including likely twin lamellae that are below the resolution of the EBSD map. BC = band contrast, IPFx = inverse pole figure (x), SB = special boundary.

Figure 33. Reidite-bearing zircon in the 17.5 GPa thin section. A significant portion of the zircon grain (green) has been converted to domanial reidite (red). BC = band contrast.

Figure 34. Distribution of deformation microstructures in zircon from the 2.5 GPa thin section, overlaid with the positions of all zircon grains and their respective shock metamorphic features. Regions of like features (PF and PDB) are connected

Figure 35. Distribution of deformation microstructures in zircon from the 5 GPa thin section, overlaid with the positions of all zircon grains and their respective shock metamorphic features. Regions of like features (PF and PDB) are connected.

Figure 36. Distribution of deformation microstructures in zircon from the 7.5 GPa thin section, overlaid with the positions of all zircon grains and their respective shock metamorphic features. Regions of like features (PF, PDB and melt films) are connected.

Figure 37. Distribution of deformation microstructures in zircon from the 10 GPa thin section, overlaid with the positions of all zircon grains and their respective shock metamorphic features. Regions of like features are connected, with reidite, twins and PDB appearing to be concentrically distributed outward from the shockwave propagation direction.

Figure 38. Distribution of deformation microstructures in zircon from the 12.5 GPa thin section, overlaid with the positions of all zircon grains and their respective shock metamorphic features. Regions of like features are connected, with reidite, twins and PDB appearing to be concentrically distributed outward from the shockwave propagation direction.

Figure 39. Distribution of deformation microstructures in zircon from the 15 GPa thin section, overlaid with the positions of all zircon grains and their respective shock metamorphic features. Regions of like features are connected, with reidite, twins and PDB appearing to be concentrically distributed outward from the shockwave propagation direction. The two different images show different interpretations of the shock microstructures, namely the zone containing PDB.

Figure 40. Distribution of deformation microstructures in zircon from the 17.5 GPa thin section, overlaid with the positions of all zircon grains and their respective shock metamorphic features. Regions of like features are connected, with reidite, twins and PDB appearing to be concentrically distributed outward from the shockwave propagation direction.

Figure 41. Percentages of zircons showing progression of shock microstructures in each of the shocked thin sections overlaid with shock stages in quartz calibrated by Kowitz et al. (2016).

Figure 42. Graph of percentages of shock features found in zircons from each thin section, overlaid with shock stages in quartz calibrated by Kowitz et al. (2016).

Figure 43. Band contrast and phase EBSD map of reidite-bearing grains in the 10 GPa to 17.5 GPa thin sections. The relative portion of the mapped grain containing reidite is seen to increase with shock pressure.

Figure 44. Graph of the maximum %age of reidite in a mapped grain for each thin section between 10 and 17.5 GPa showing an increase in the %age of zircon converted to reidite in the mapped portion of the grain with pressure.

Figure 45. Mesoscale numerical modelling of a shock-wave with a nominal bulk pressure of 2.5 GPa passing through a porous medium conducted by Kowitz et al. (2013). Relative shock pressure is indicated by the colour bar in the bottom left, and excursions of pressure up to four times the bulk shock pressure are observed (red areas).

Figure 46. Mesoscale numerical modelling of shock waves passing through single and multiple pores conducted by Güldemeister et al. (2013). Shock pressure magnification is seen to be up to four times the nominal bulk pressure.

Figure 47. Pressure-temperature-time path plots of minerals in nonporous (crystalline) and porous rocks at pressures insufficient to cause shock metamorphic features, and pressures sufficient to cause those features. **(A)** Pressure-temperature path for minerals in a crystalline rock that have not achieved the pressure required to form shock metamorphic features (apparent threshold pressure). Calculated applied pressure and maximum pressure are the same, as there is no microstructural variation in pressure resulting from pore collapse. **(B)** Pressure-temperature path for minerals in a crystalline rock that have achieved the pressure required to form shock metamorphic features (apparent threshold pressure). Again, calculated applied pressure and maximum pressure are the same, as there is no pressure variation in the microstructure due to porosity. **(C)** Pressure-temperature path for minerals in a porous rock that have not achieved the pressure required to form shock metamorphic features (apparent threshold pressure). Calculated applied pressure and maximum pressure are not the same, as microstructural variations in pressure (and therefore post-shock temperature) result in a range of shock pressures at different points in the microstructure. **(D)** Pressure-temperature path for minerals in a porous rock that have achieved the pressure required to form shock metamorphic features (apparent threshold pressure). Whilst the calculated applied pressure appears to be below the apparent threshold pressure required to form microstructures, the range of pressures resulting from pressure magnifications on a

pore-grain scale cause some portions of the shocked porous rock to exceed the apparent threshold pressure, forming shock metamorphic features in these portions.

Figure 48 Whole thin-section BSE maps showing the dome-shaped region of less deformation located at the bottom of each thin section. In the 7.5, 12.5 and 15 GPa thin sections this region is more pronounced, however in the 17.5 GPa thin section this region is more difficult to discern.

9 - Figures

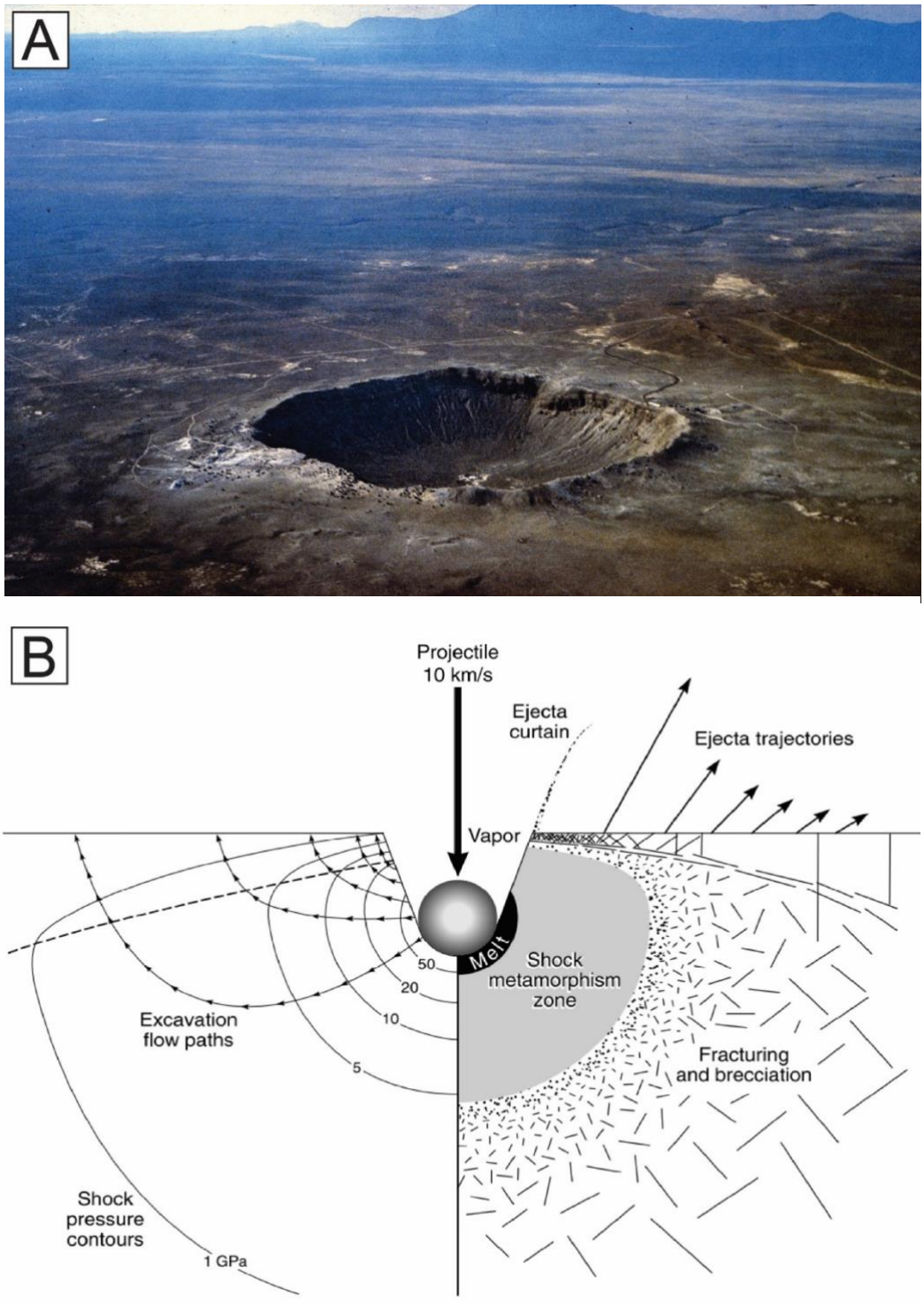

Figure 1

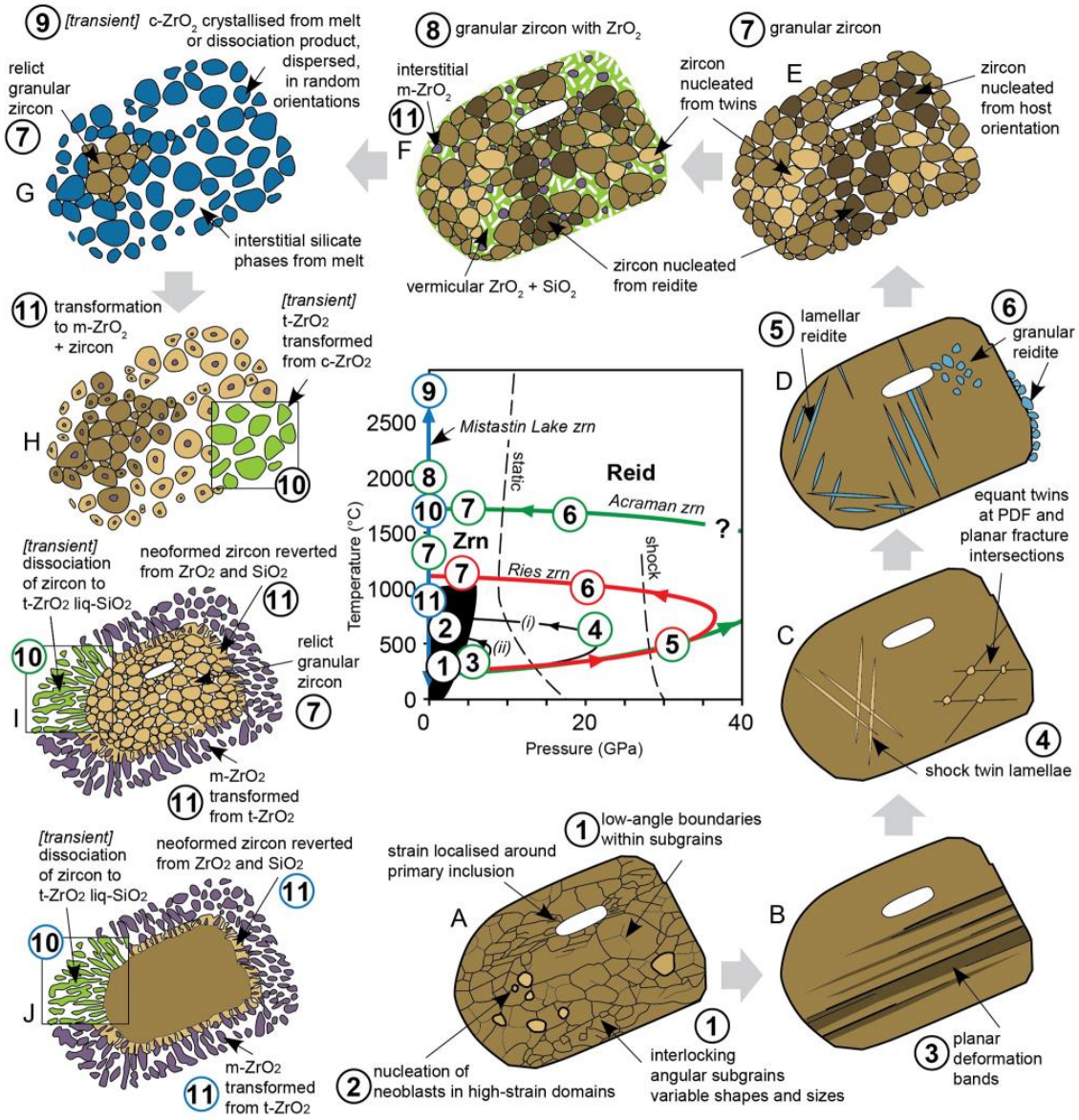
9 [transient] c-ZrO2 crystallised from melt or dissociation product, dispersed, in random orientations
relict granular zircon
7
G
interstitial silicate phases from melt
8 granular zircon with ZrO2
interstitial m-ZrO2
11
F
vermicular ZrO2 + SiO2
zircon nucleated from reidite
7 granular zircon
zircon nucleated from twins
E
zircon nucleated from host orientation
11 transformation to m-ZrO2 + zircon
[transient] t-ZrO2 transformed from c-ZrO2
H
10
[transient] dissociation of zircon to t-ZrO2 liq-SiO2
neoformed zircon reverted from ZrO2 and SiO2
relict granular zircon
I
m-ZrO2 transformed from t-ZrO2
[transient] dissociation of zircon to t-ZrO2 liq-SiO2
neoformed zircon reverted from ZrO2 and SiO2
J
m-ZrO2 transformed from t-ZrO2
Temperature (°C)
Pressure (GPa)
Mistastin Lake zrn
static
Reid
Acraman zrn
?
Zrn
Ries zrn
shock
(i)
(ii)
5 lamellar reidite
6 granular reidite
D
equant twins at PDF and planar fracture intersections
C
4 shock twin lamellae
1 low-angle boundaries within subgrains
strain localised around primary inclusion
A
2 nucleation of neoblasts in high-strain domains
1 interlocking angular subgrains variable shapes and sizes
B
3 planar deformation bands

Figure 2

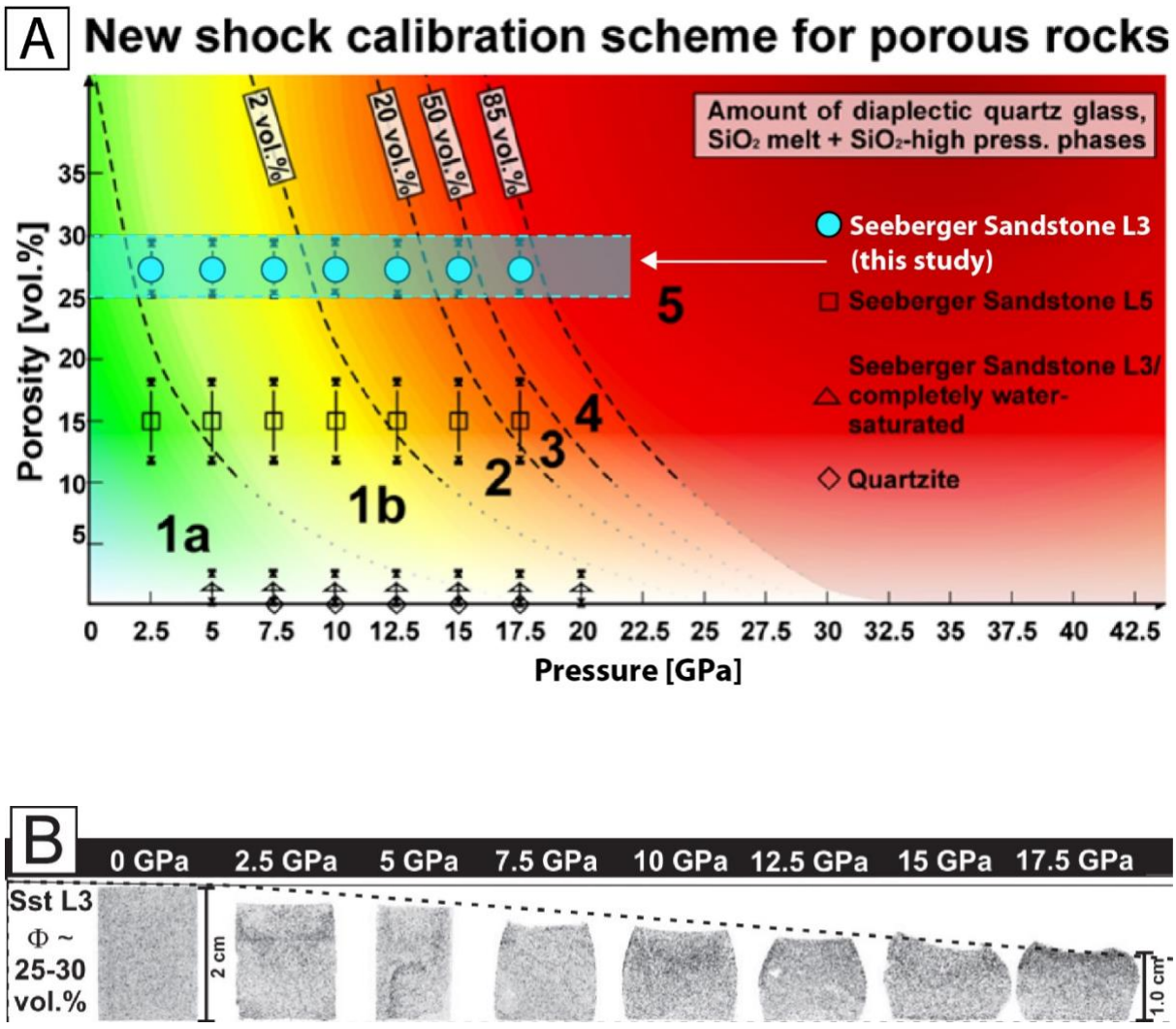
A
New shock calibration scheme for porous rocks
2 vol.%
20 vol.%
50 vol.%
85 vol.%
Amount of diaplectic quartz glass, SiO2 melt + SiO2-high press. phases
Seeberger Sandstone L3 (this study)
Seeberger Sandstone L5
Seeberger Sandstone L3/ completely water-saturated
Quartzite
1a
1b
2
3
4
5
Porosity [vol.%]
Pressure [GPa]
B
0 GPa
2.5 GPa
5 GPa
7.5 GPa
10 GPa
12.5 GPa
15 GPa
17.5 GPa
Sst L3
Φ ~
25-30
vol.%
2 cm
1.0 cm

Figure 3

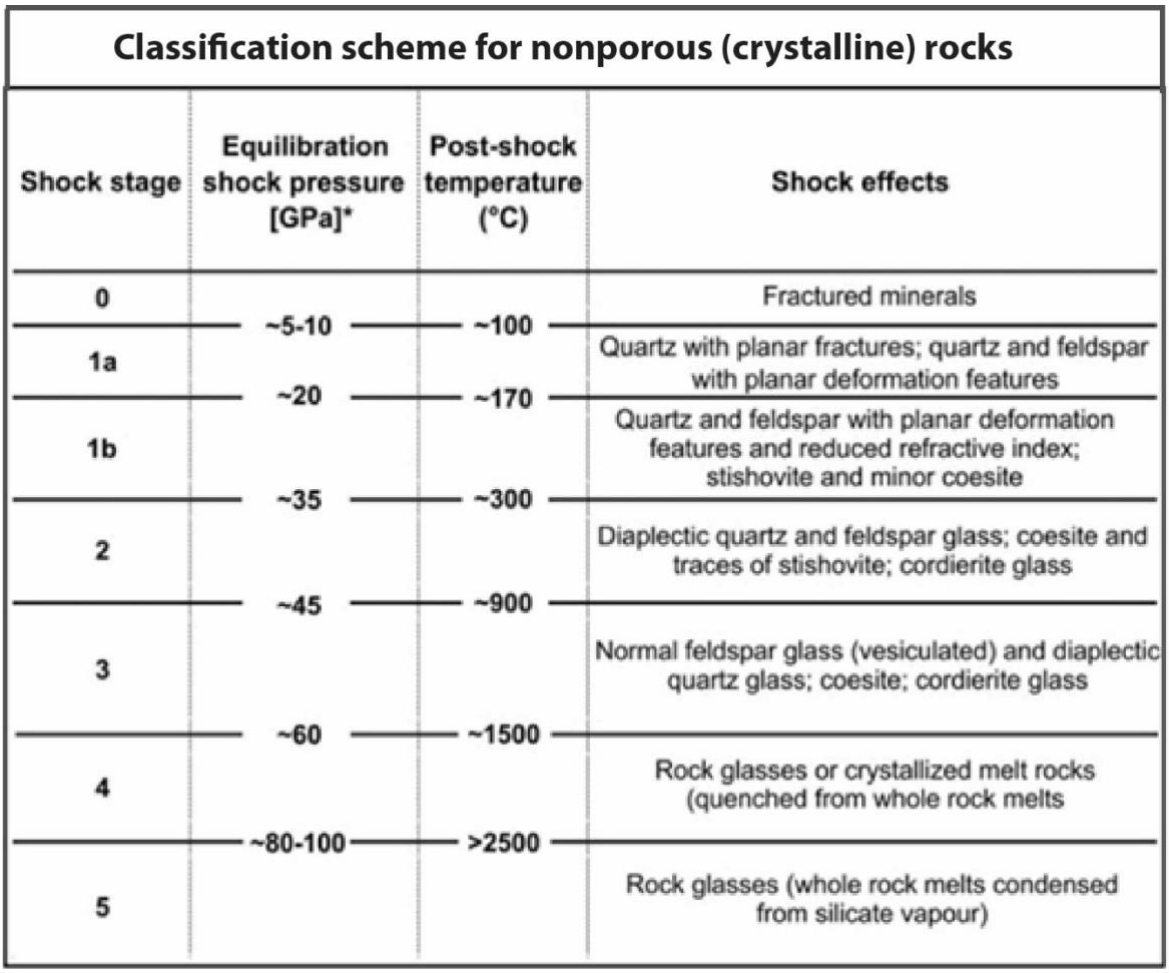

Classification scheme for nonporous (crystalline) rocks

Shock stage	Equilibration shock pressure [GPa]*	Post-shock temperature (°C)	Shock effects
0	~5-10	~100	Fractured minerals
1a	~20	~170	Quartz with planar fractures; quartz and feldspar with planar deformation features
1b	~35	~300	Quartz and feldspar with planar deformation features and reduced refractive index; stishovite and minor coesite
2	~45	~900	Diaplectic quartz and feldspar glass; coesite and traces of stishovite; cordierite glass
3	~60	~1500	Normal feldspar glass (vesiculated) and diaplectic quartz glass; coesite; cordierite glass
4	~80-100	>2500	Rock glasses or crystallized melt rocks (quenched from whole rock melts
5			Rock glasses (whole rock melts condensed from silicate vapour)

Figure 4

A

Classification scheme for porous sandstones

Shock stage	Equilibration shock pressure [GPa]*	Post-shock temperature (°C)	Shock effects
0	0.2-0.9	~25	Undeformed sandstone
1a	~3.0 (2.2-4.5)	~250	Compacted sandstone with remnant porosity
1b	~5.5 (3.6-13)	~350	Compacted sandstone compressed to zero porosity
2	~13	~950	Dense (non-porous) sandstone with 2-5 wt.% coesite, 3-10 wt.% glass and 80-95 wt.% quartz
3	~30	>1000	Dense (non-porous) sandstone with 18-32 wt.% coesite, traces of stishovite, 0-20 wt.% glass and 45-80 wt.% quartz
4			Dense (non-porous) sandstone with 10-30 wt.% coesite, 20-75 wt.% glass and 15-45 wt.% quartz
5			Vesicular (pumiceous) rock with 0-5 wt.% coesite, 80-100 wt.% glass (lechatelierite) and 0-15 wt.% quartz

B

New classification and calibration of dry, porous sandstone

Shock stage	Shock effects	Amount of diapl.qz glass, SiO_2 melt + high pres. phases of SiO_2 [vol.%]	Equilibration Shock pressure [GPa] Φ ~25-30 vol.%	Equilibration Shock pressure [GPa] Φ ~12-19 vol.%
0	Undeformed sandstone			
1a	Compacted sandstone with remnant porosity	0	< 1.5	< 4
1b	Compacted sandstone compressed to zero porosity	2	9	11.5
2	Dense (non-porous) sandstone with diaplectic quartz glass, SiO_2 melt, SiO_2 high-pressure phases, SiO_2 glass (lechatelierite), and quartz	20	14	16.5
3		50	16	19
4		85	18	21.5
5	Vesicular (pumiceous) rock with dominant SiO_2 glass (lechatelierite)			

Figure 5

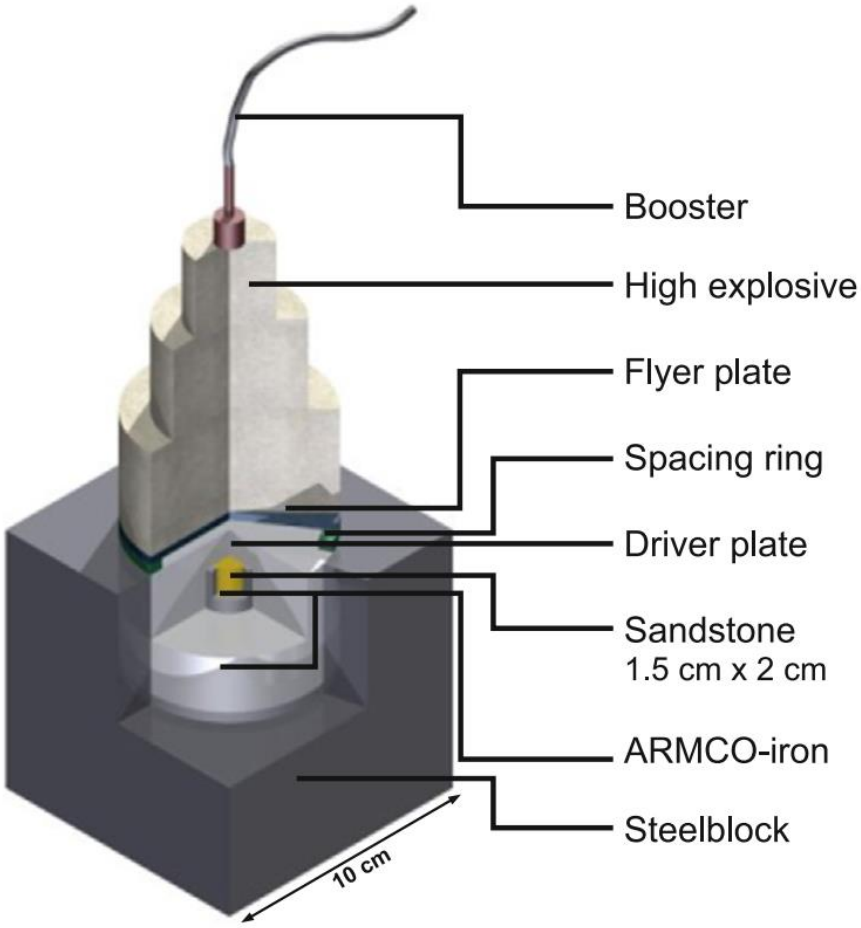
Booster
High explosive
Flyer plate
Spacing ring
Driver plate
Sandstone
1.5 cm x 2 cm
ARMCO-iron
Steelblock
10 cm

Figure 6

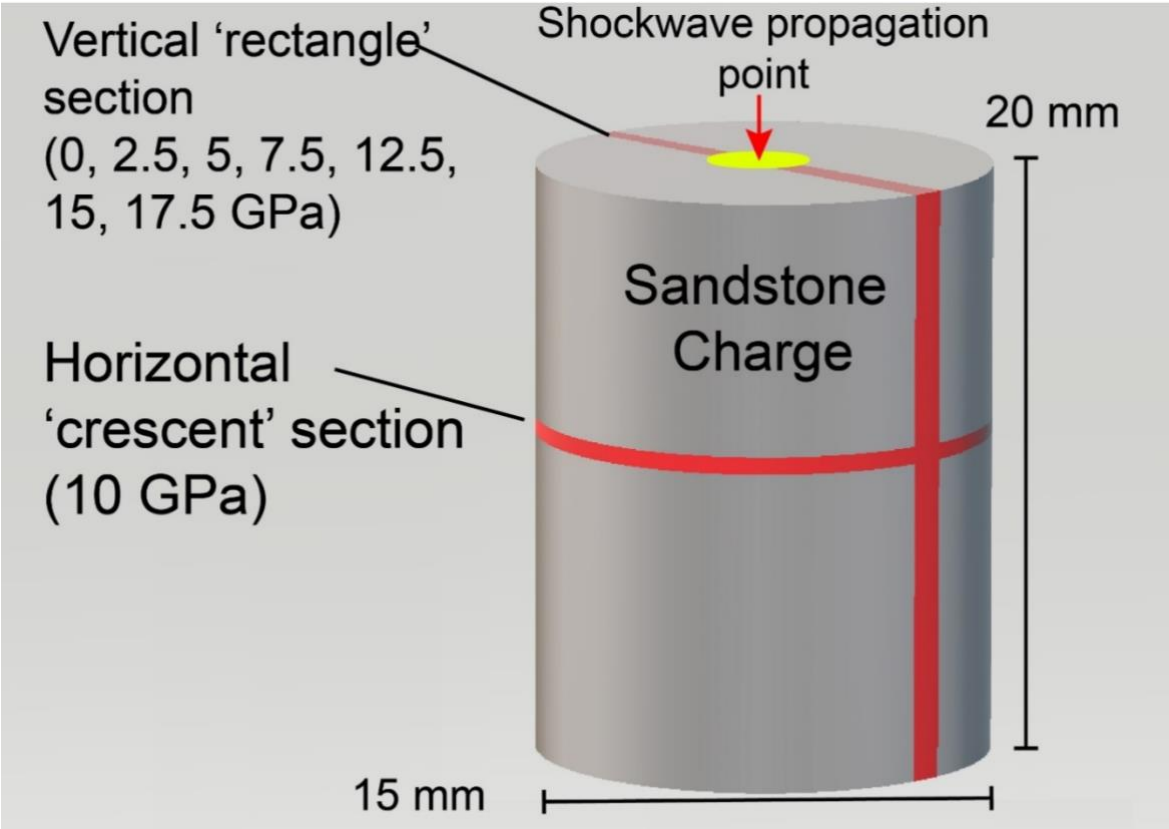
Vertical 'rectangle' section (0, 2.5, 5, 7.5, 12.5, 15, 17.5 GPa)
Shockwave propagation point
20 mm
Sandstone Charge
Horizontal 'crescent' section (10 GPa)
15 mm

Figure 7

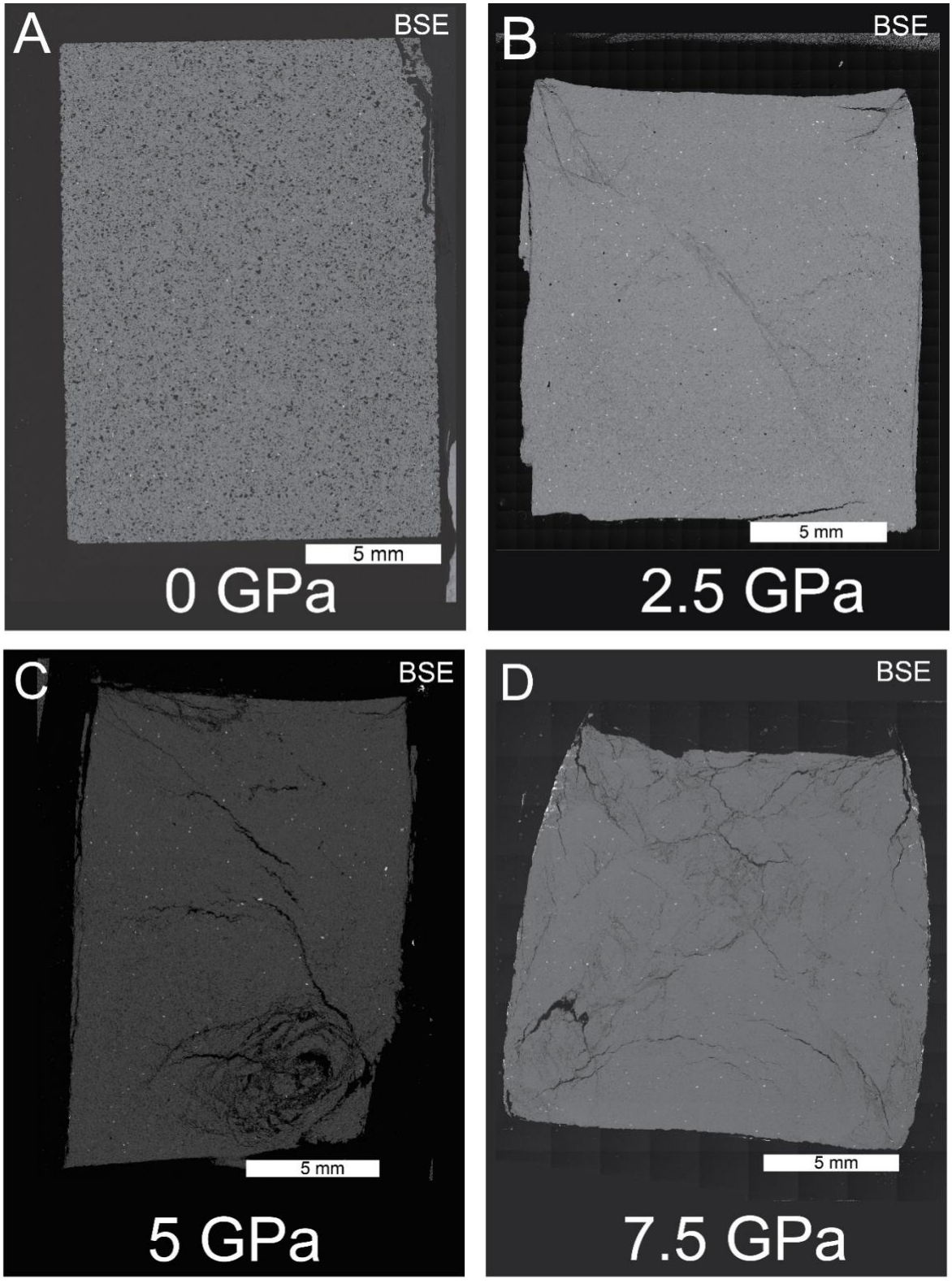

Figure 8

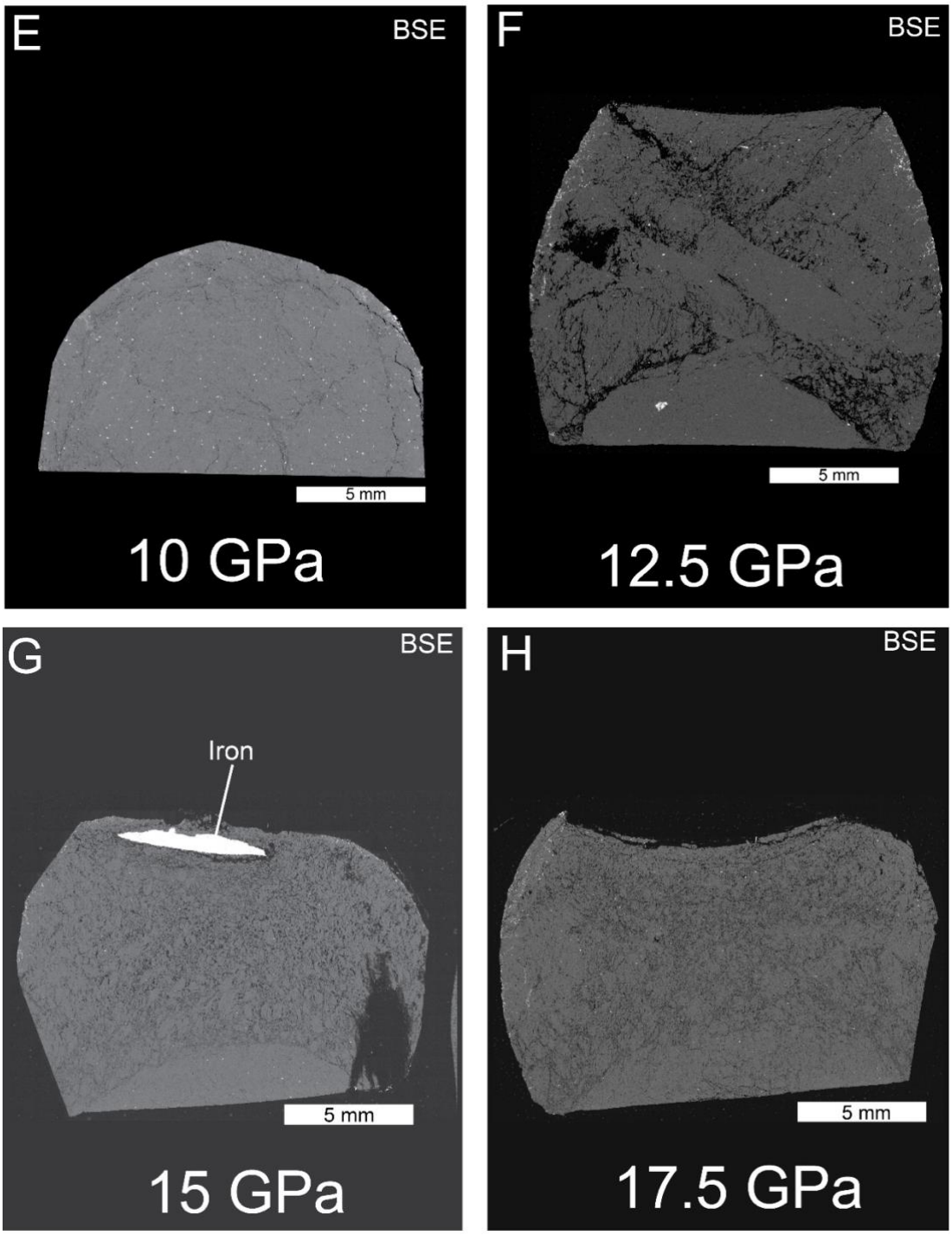

Figure 8 (cont.)

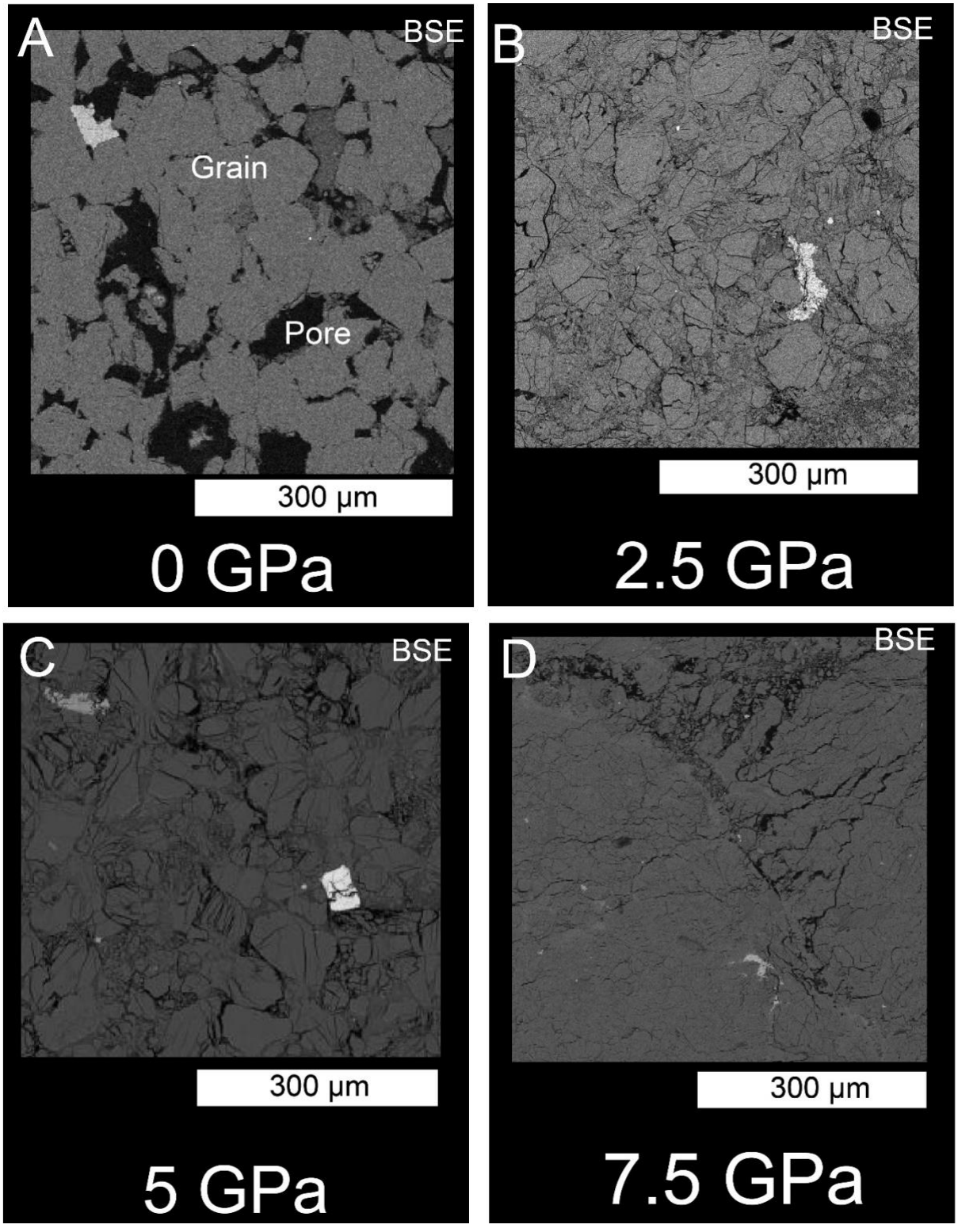
A
BSE
Grain
Pore
300 µm
0 GPa
B
BSE
300 µm
2.5 GPa
C
BSE
300 µm
5 GPa
D
BSE
300 µm
7.5 GPa

Figure 9

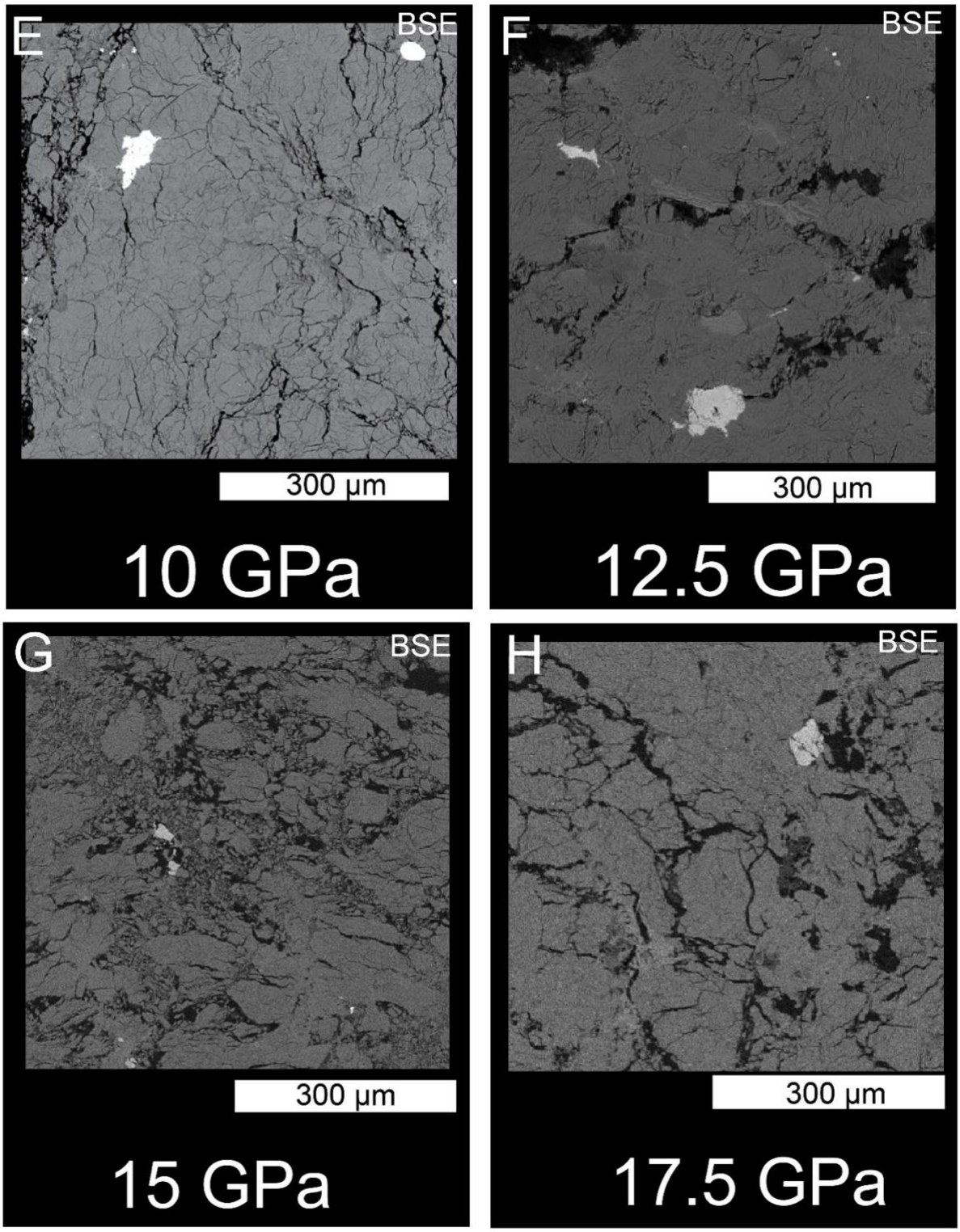

Figure 9 (cont.)

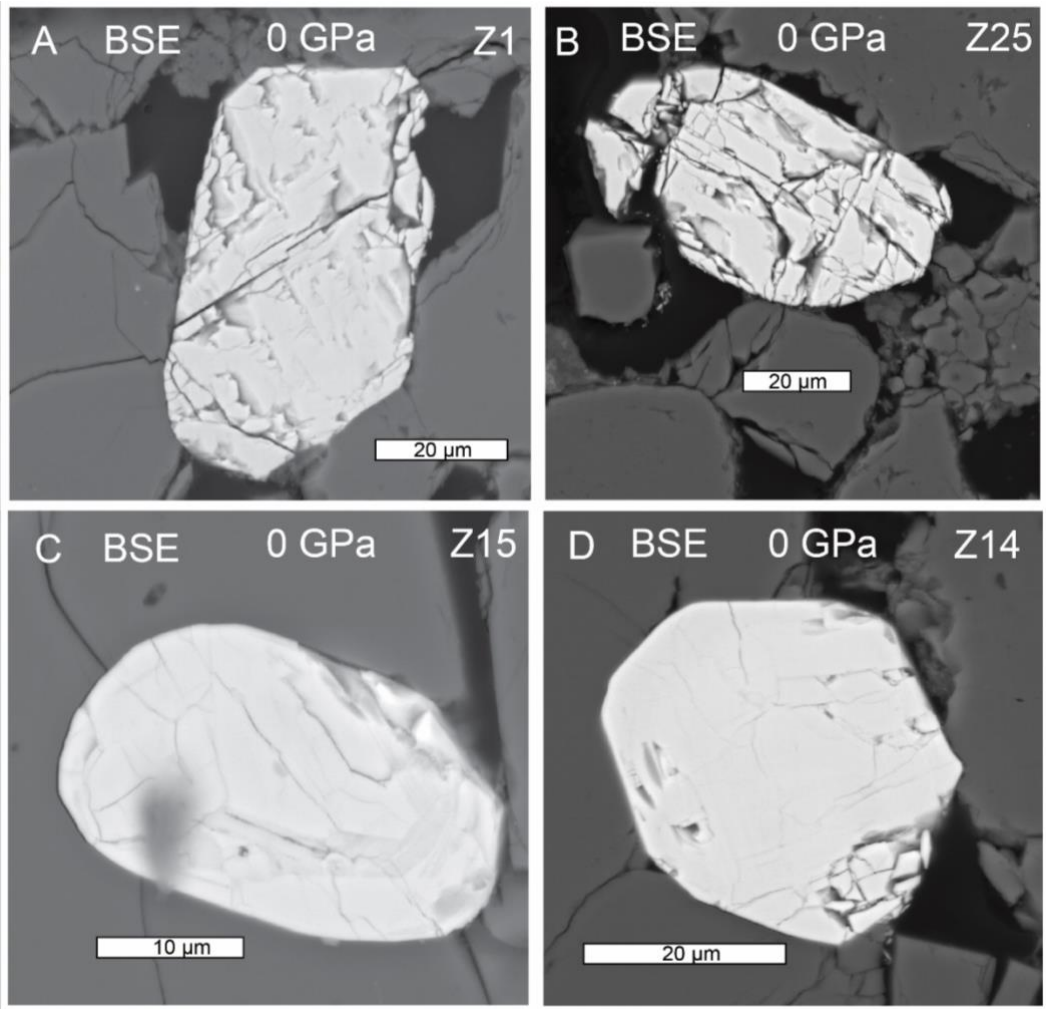
A BSE 0 GPa Z1
20 µm
B BSE 0 GPa Z25
20 µm
C BSE 0 GPa Z15
10 µm
D BSE 0 GPa Z14
20 µm

Figure 10

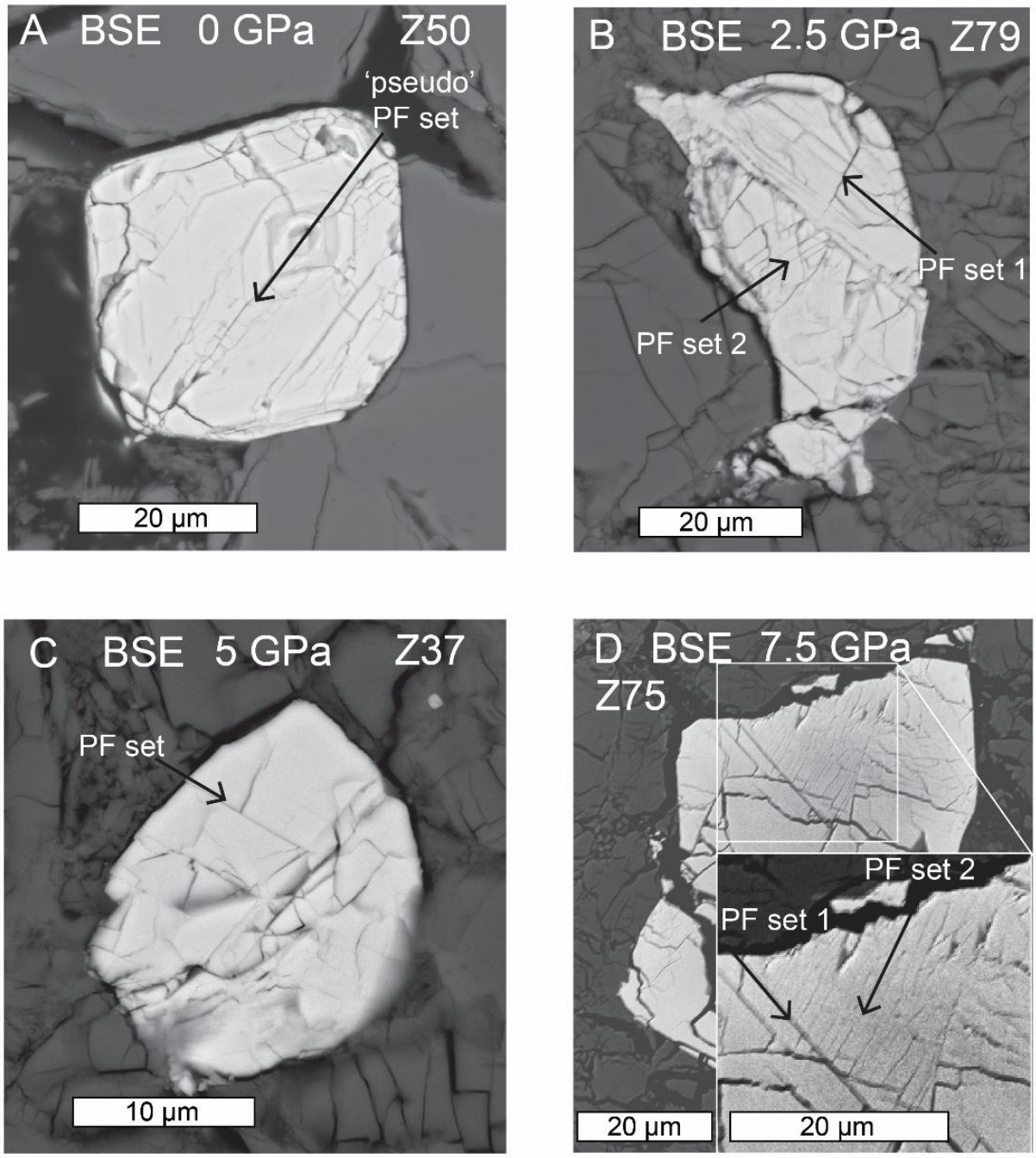
A BSE 0 GPa Z50
'pseudo'
PF set
20 µm
B BSE 2.5 GPa Z79
PF set 1
PF set 2
20 µm
C BSE 5 GPa Z37
PF set
10 µm
D BSE 7.5 GPa
Z75
PF set 2
PF set 1
20 µm
20 µm

Figure 11

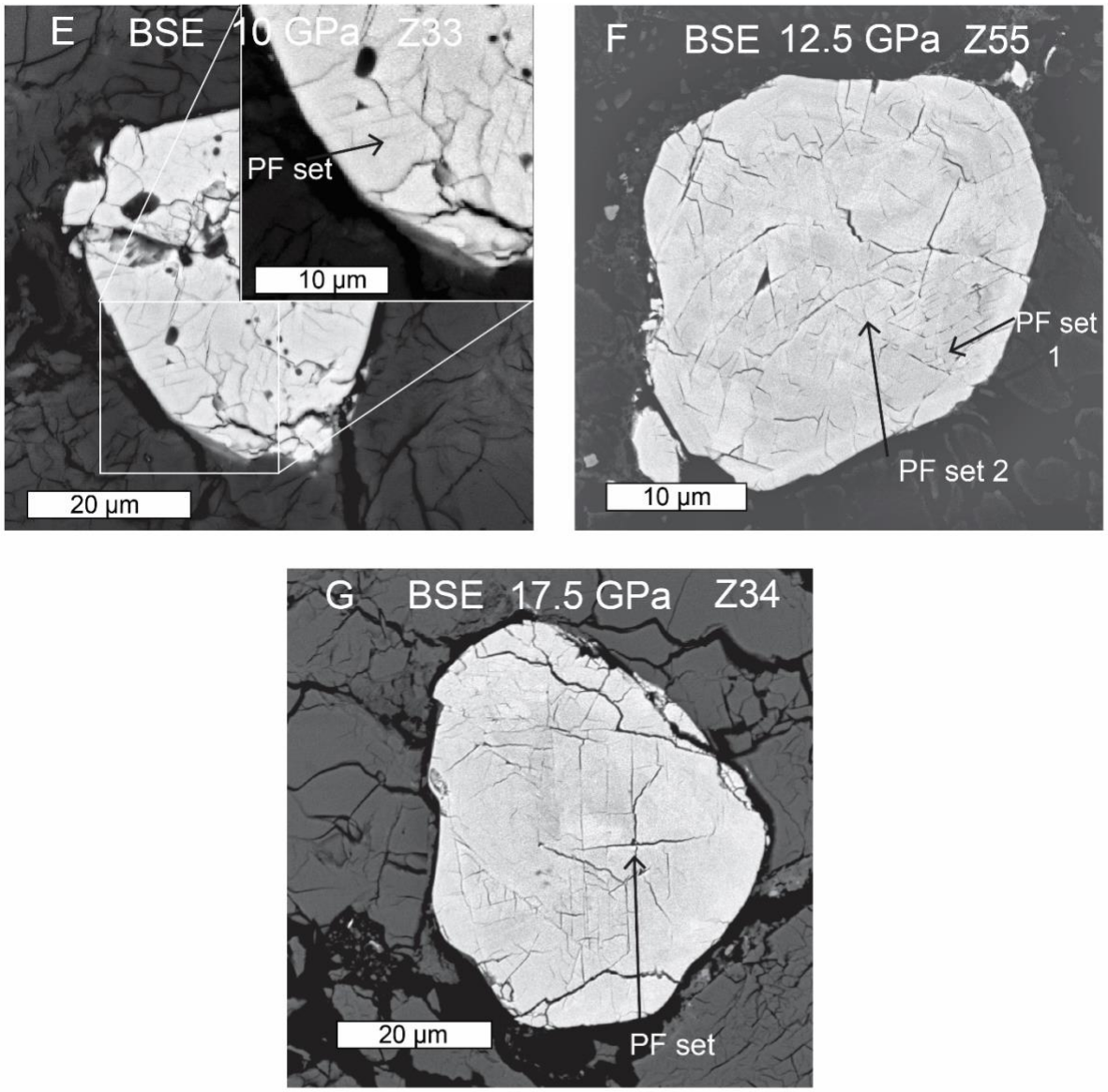

Figure 11 (cont.)

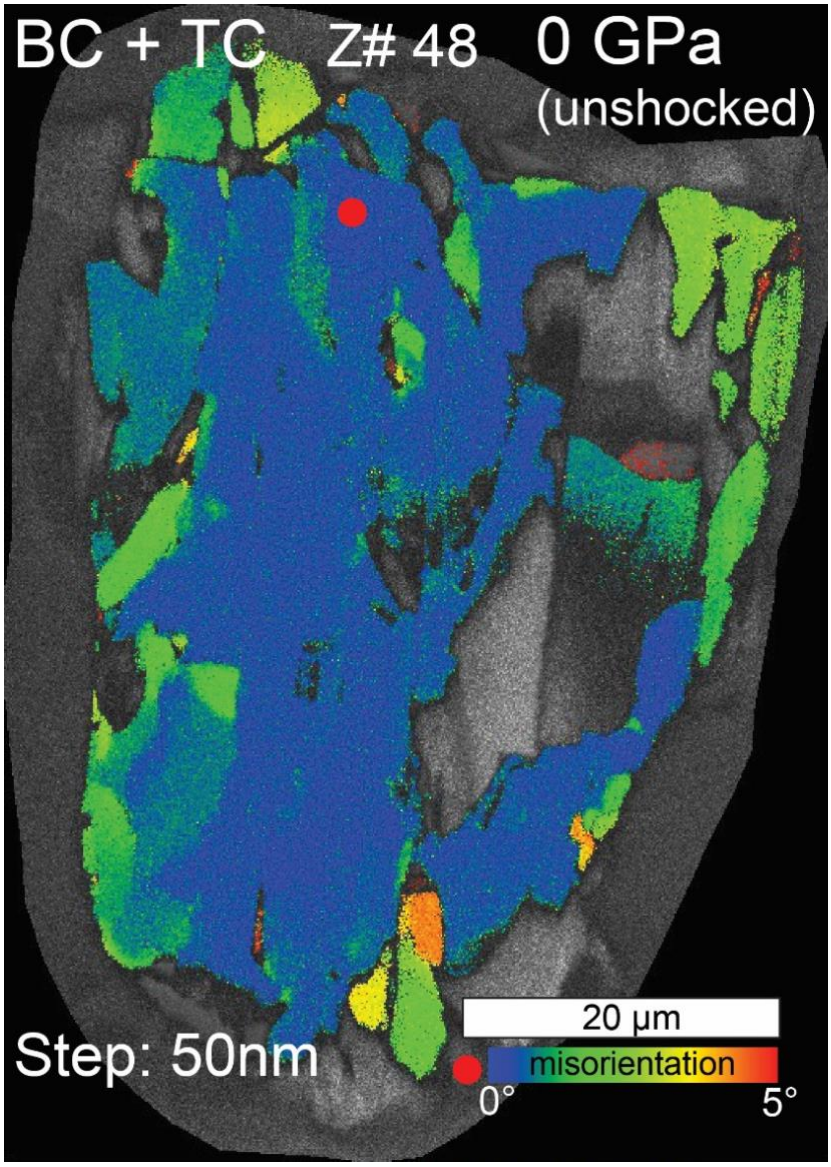

Figure 12

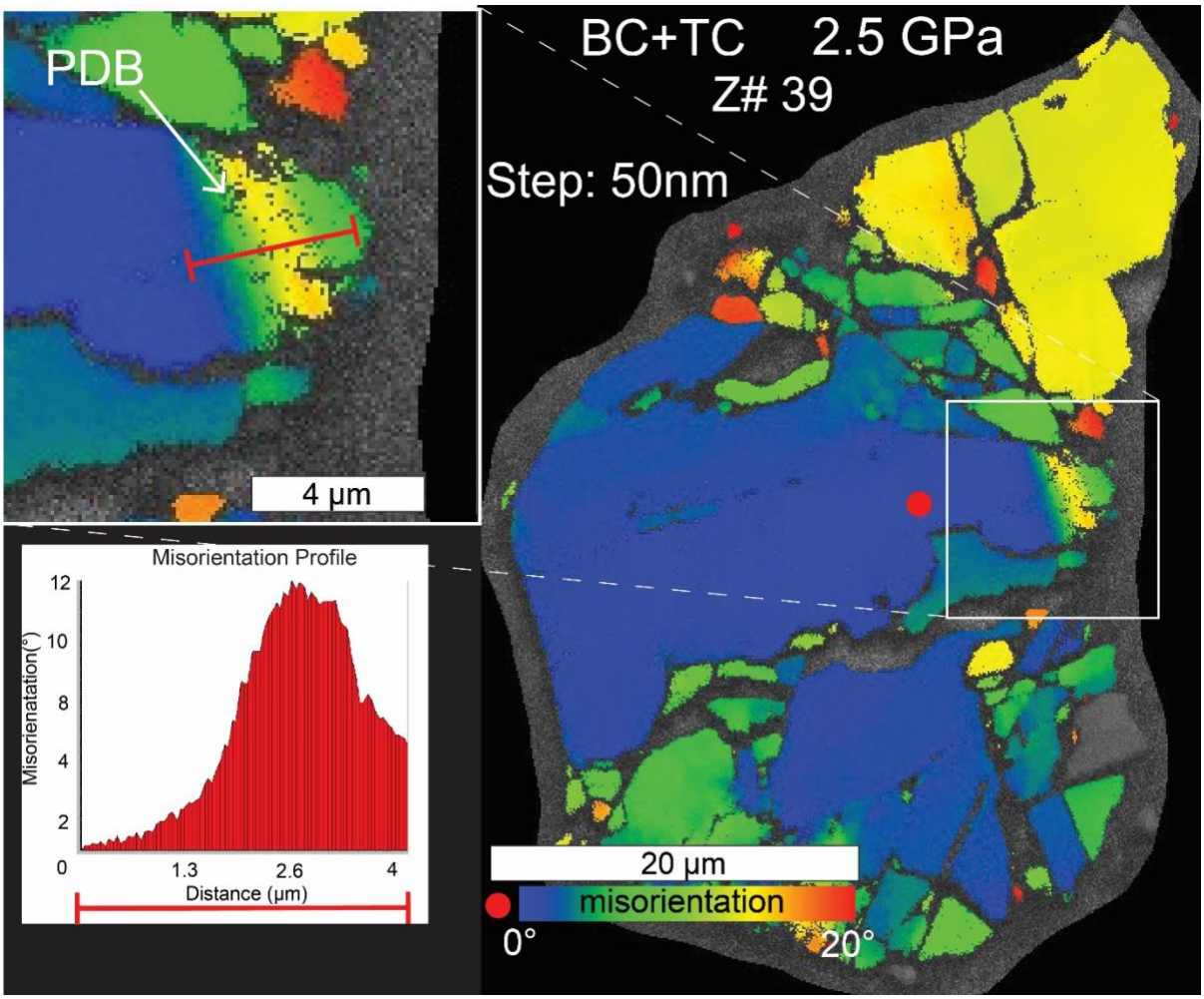
PDB
4 µm
BC+TC 2.5 GPa
Z# 39
Step: 50nm
Misorientation Profile
Misorienatation(°)
12
10
8
4
2
0
1.3
2.6
4
Distance (µm)
20 µm
misorientation
0°
20°

Figure 13

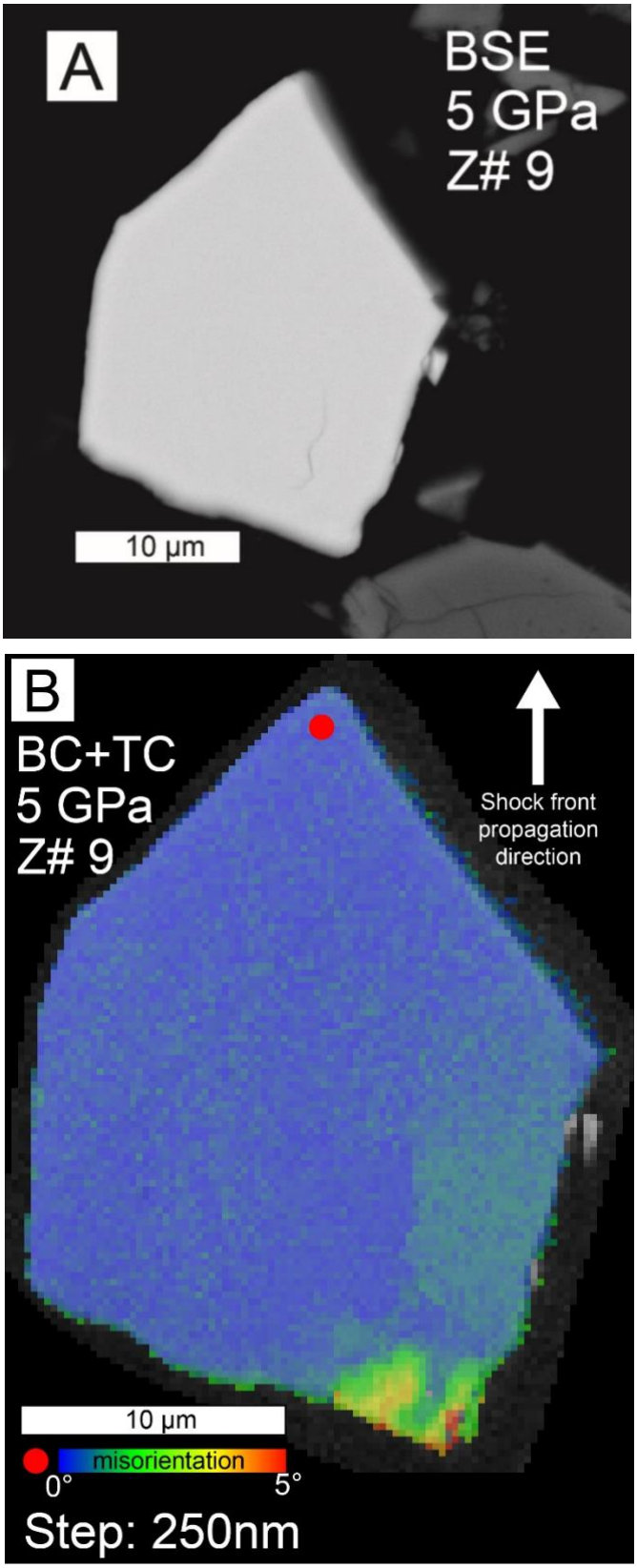
A
BSE
5 GPa
Z# 9
10 µm
B
BC+TC
5 GPa
Z# 9
Shock front
propagation
direction
10 µm
misorientation
0°
5°
Step: 250nm

Figure 14

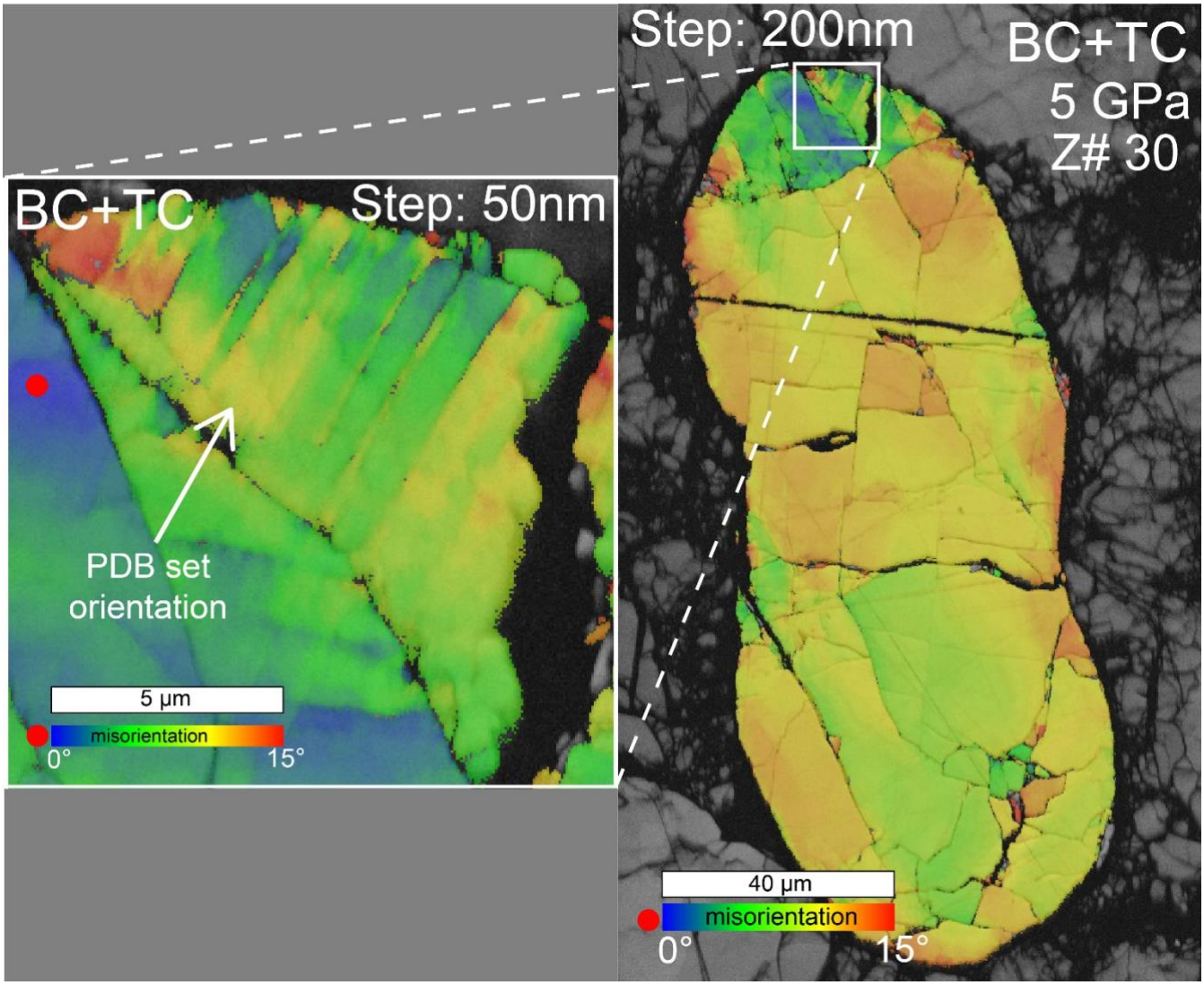
BC+TC
Step: 50nm
PDB set
orientation
5 µm
misorientation
0°
15°
Step: 200nm
BC+TC
5 GPa
Z# 30
40 µm
misorientation
0°
15°

Figure 15

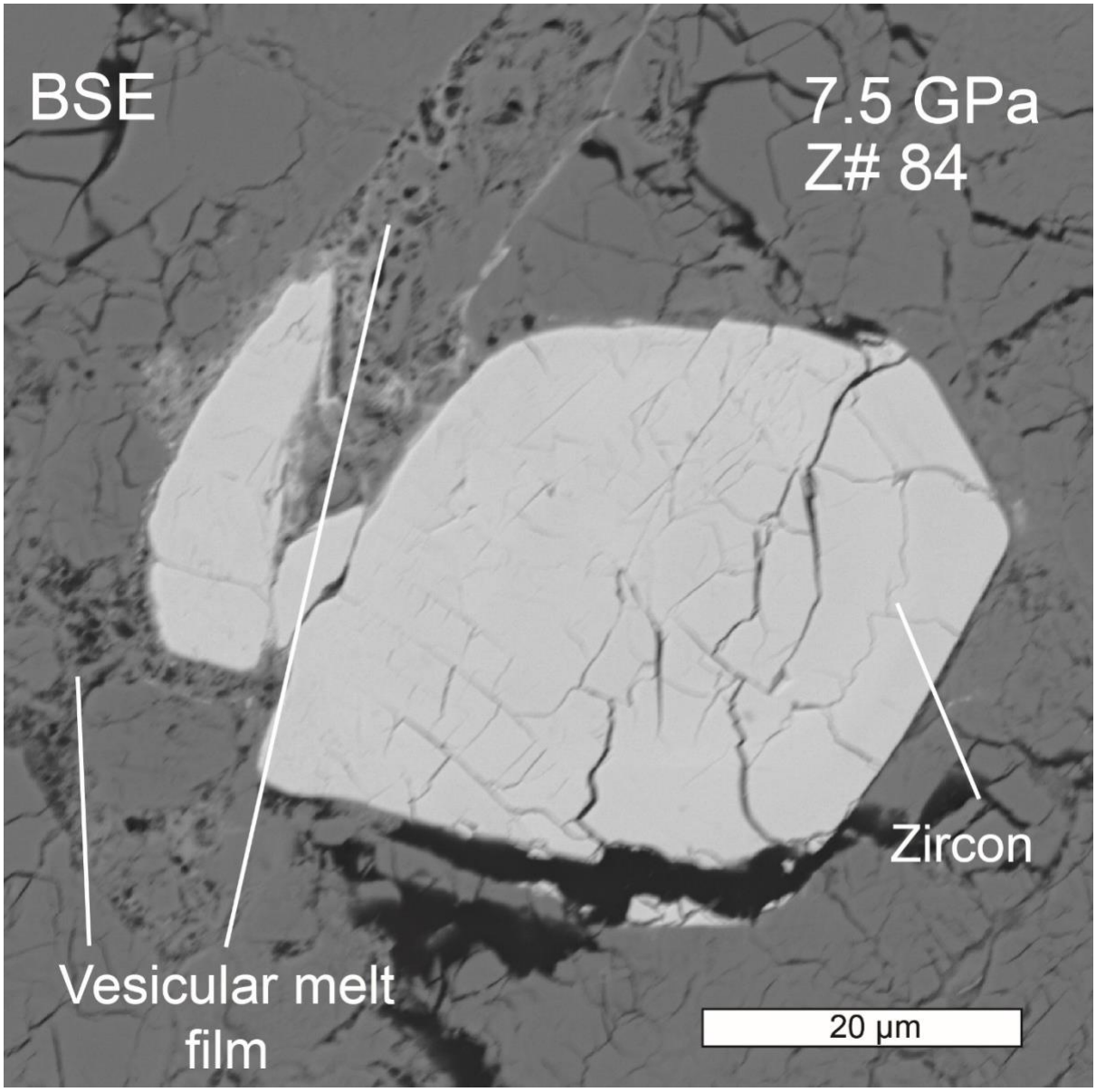

Figure 16

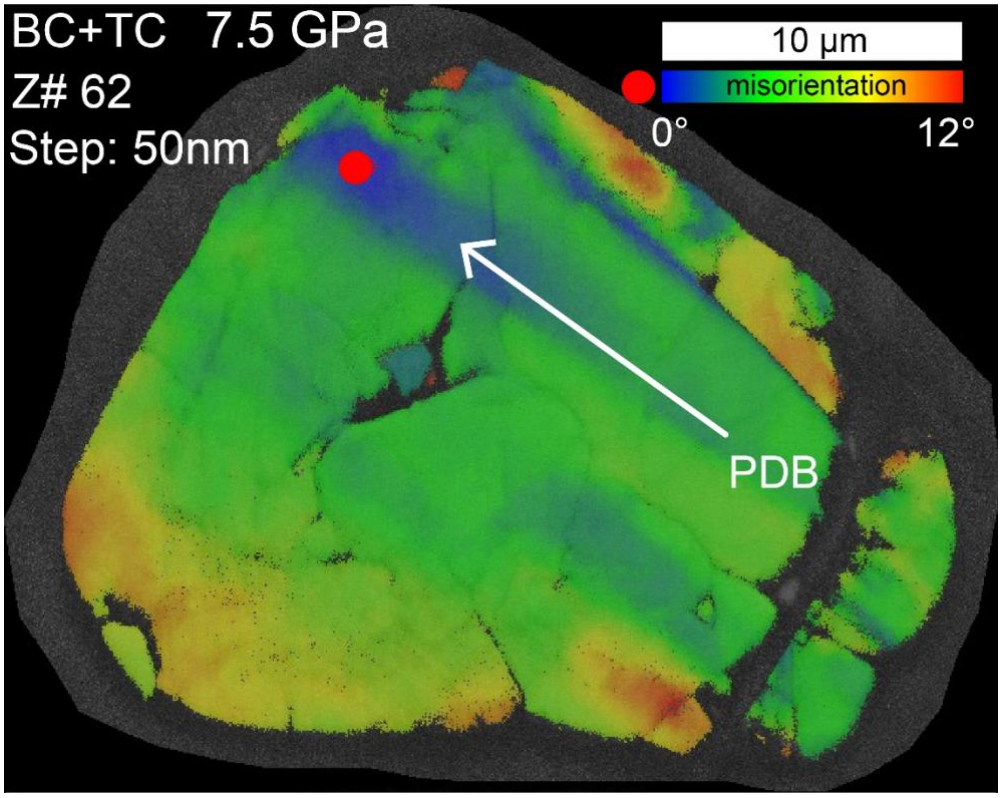

Figure 17

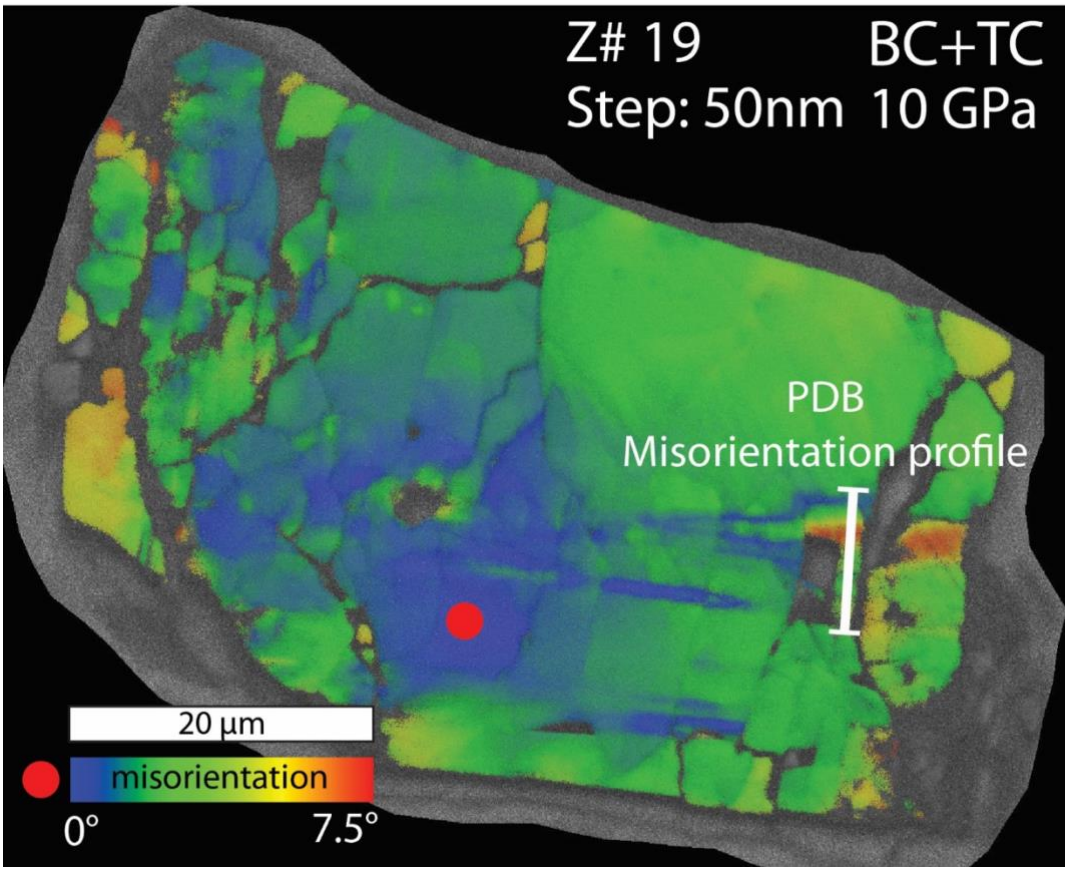
Z# 19
Step: 50nm
BC+TC
10 GPa
PDB
Misorientation profile
20 µm
misorientation
0°
7.5°

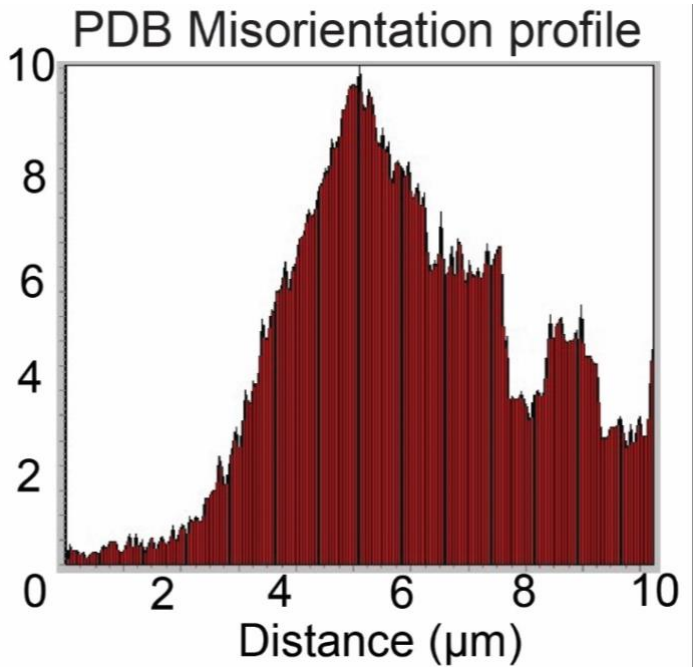
PDB Misorientation profile
10
8
6
4
2
0
2
4
6
8
10
Distance (µm)

Figure 18

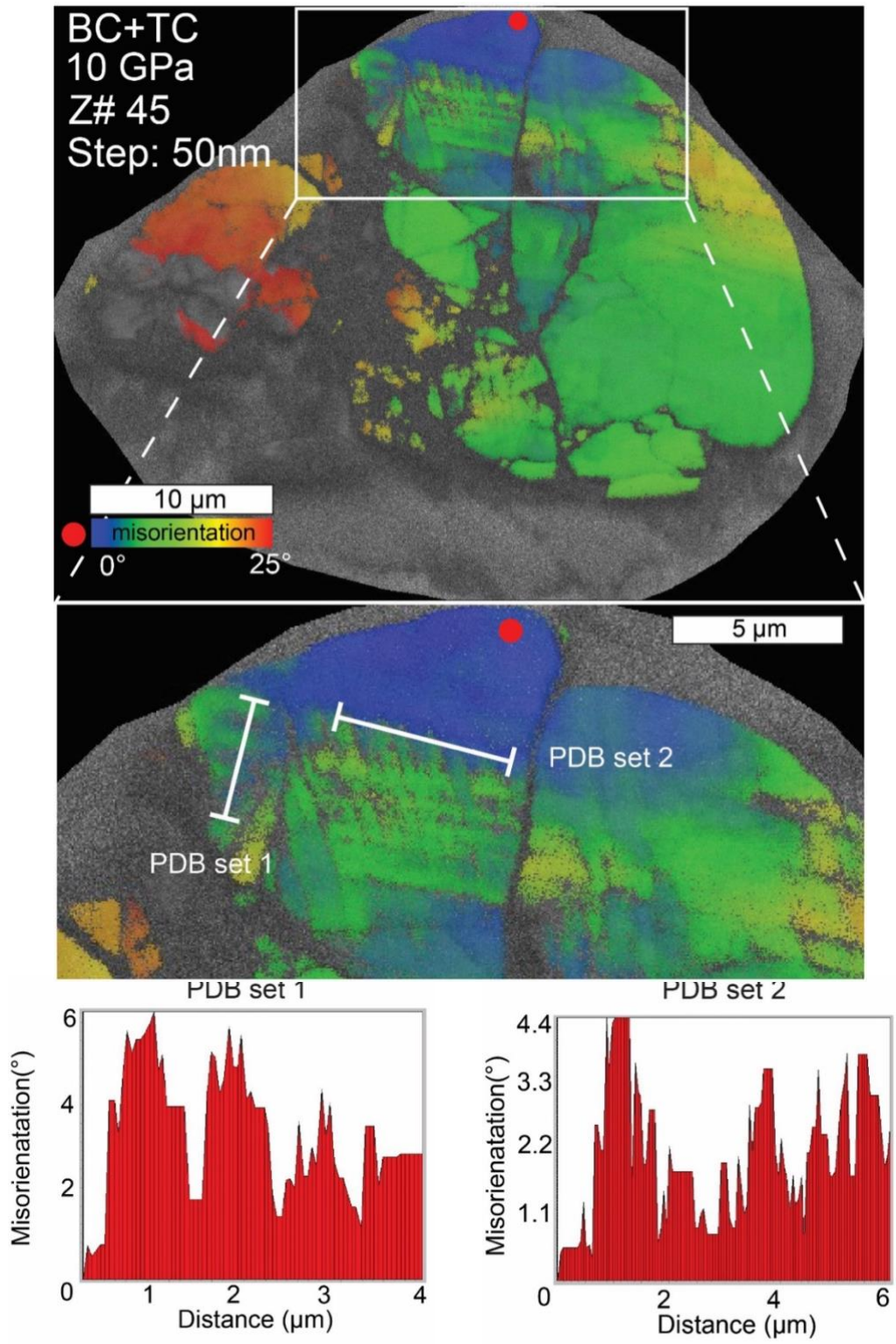
BC+TC
10 GPa
Z# 45
Step: 50nm
10 μm
misorientation
0°
25°
5 μm
PDB set 1
PDB set 2
PDB set 1
Misorienatation(°)
Distance (μm)
PDB set 2
Misorienatation(°)
Distance (μm)

Figure 19

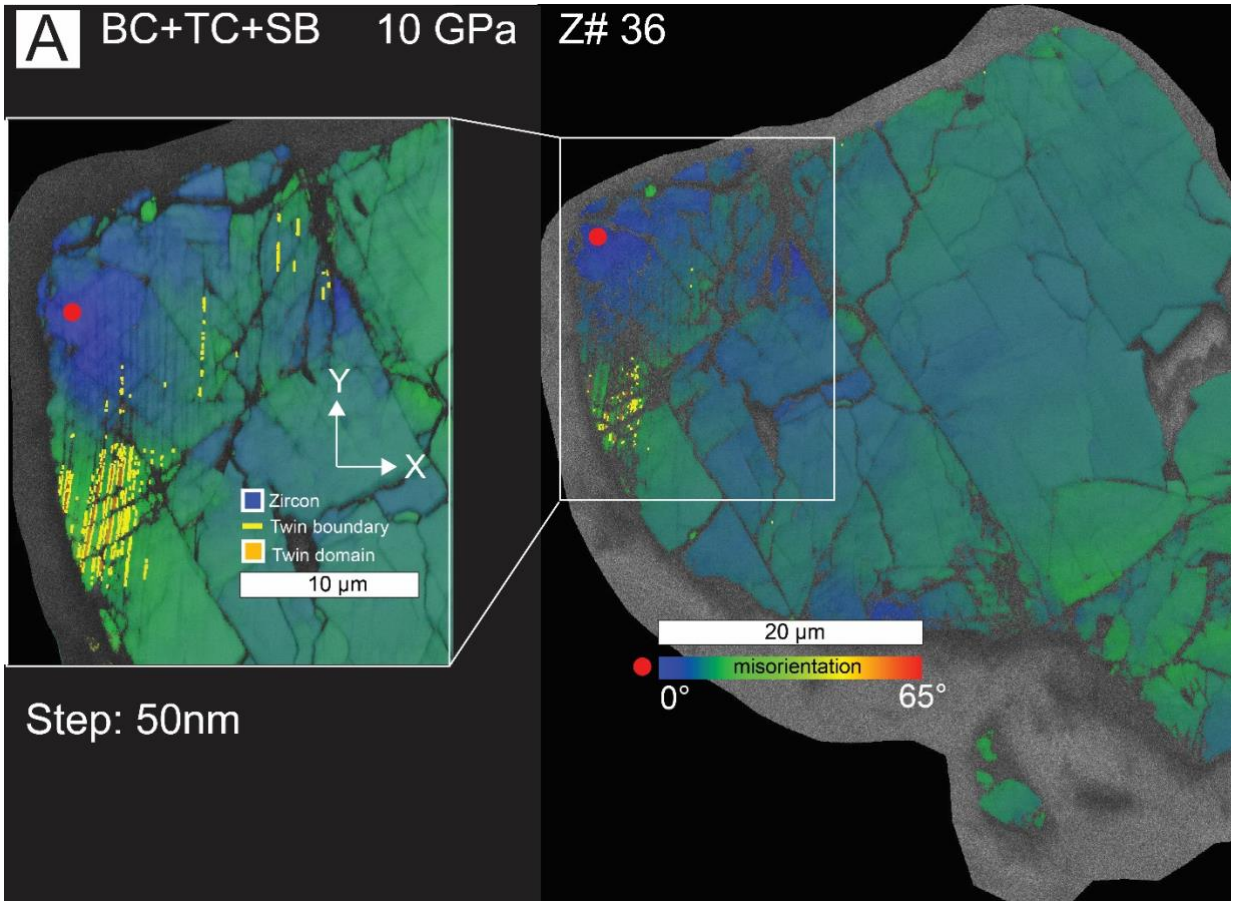
A
BC+TC+SB 10 GPa
Z# 36
Y
X
Zircon
Twin boundary
Twin domain
10 μm
20 μm
misorientation
0°
65°
Step: 50nm

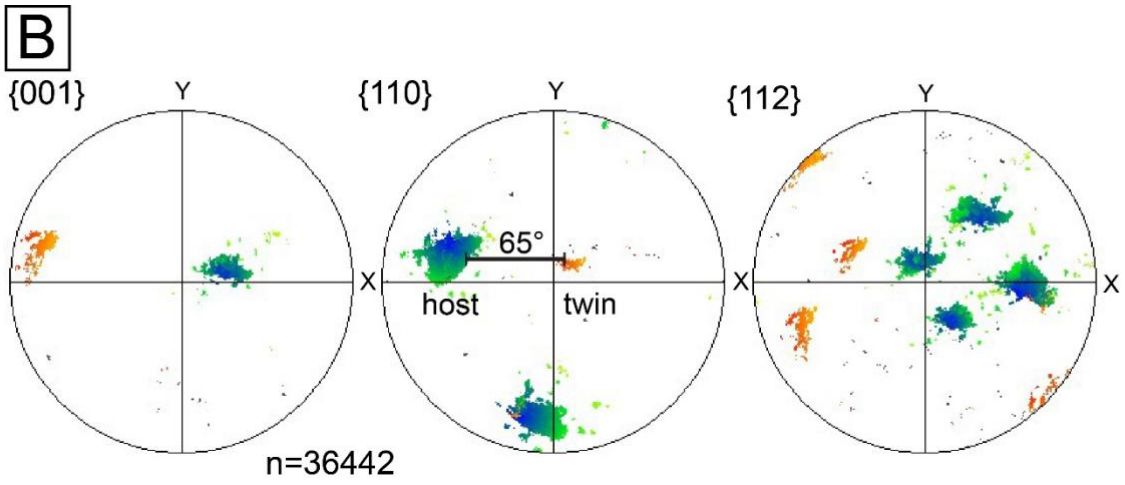
B
{001}
{110}
{112}
Y
X
65°
host
twin
n=36442

Figure 20

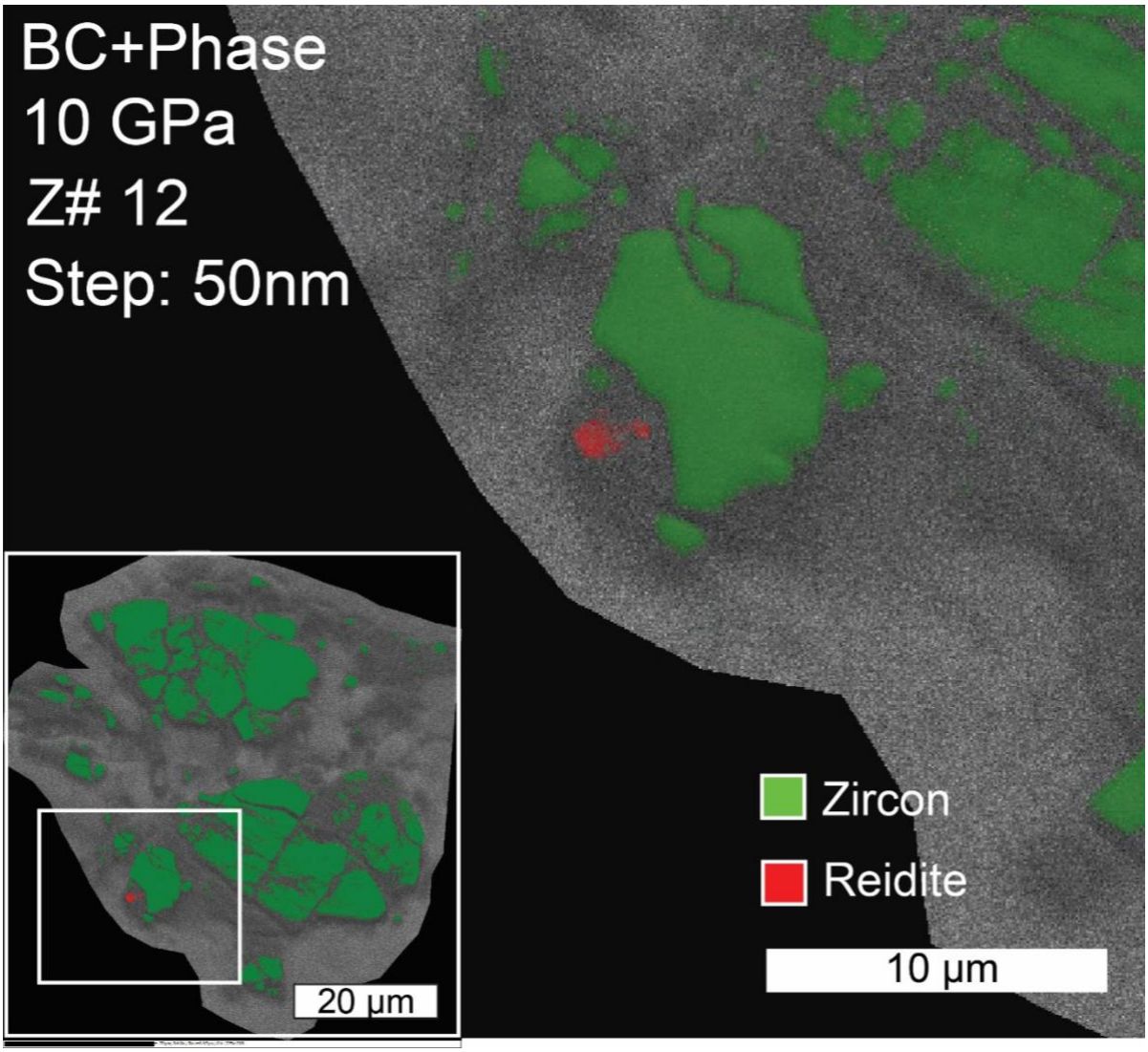

Figure 21

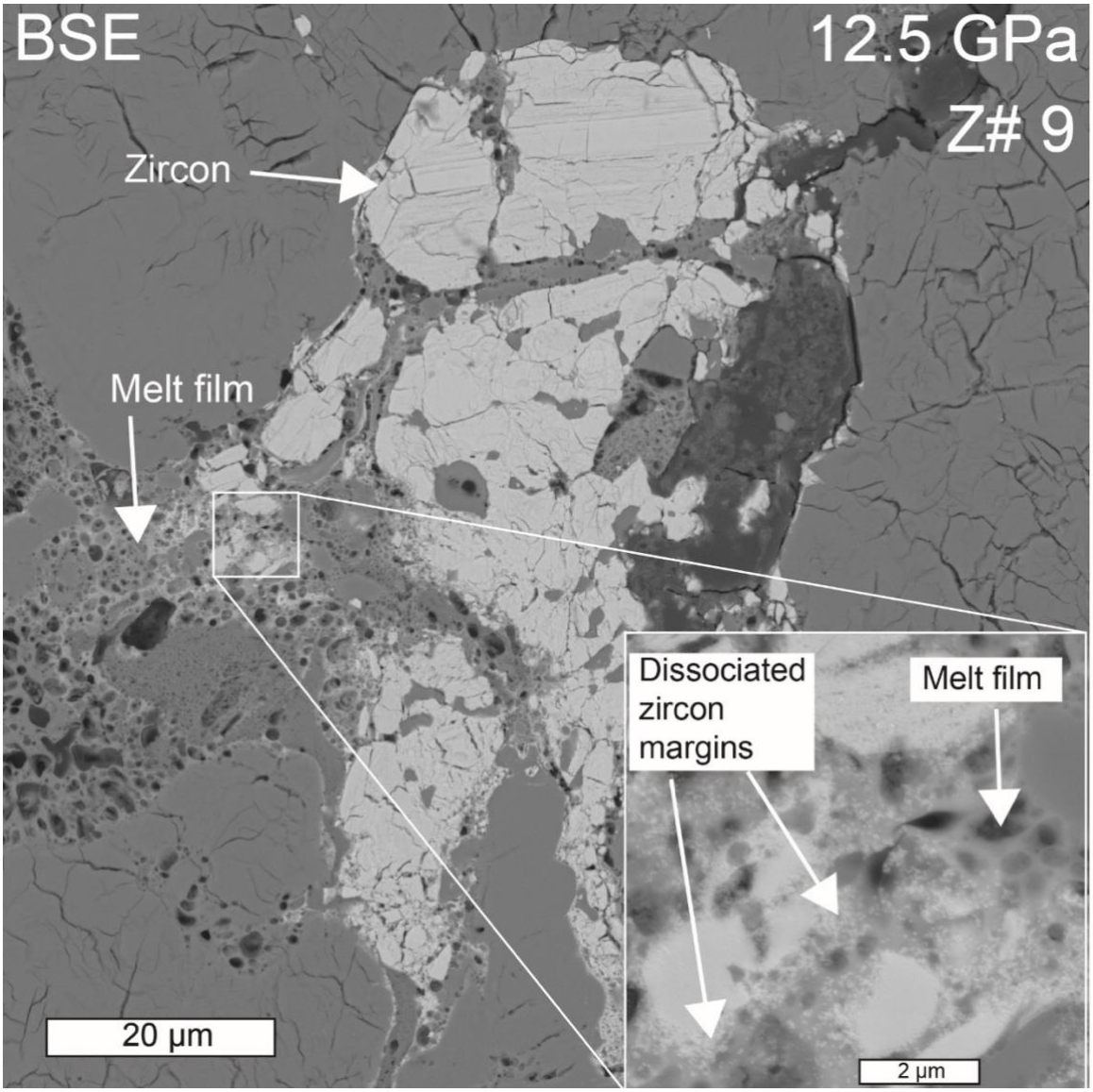
BSE
12.5 GPa
Z# 9
Zircon
Melt film
20 µm
Dissociated zircon margins
Melt film
2 µm

Figure 22

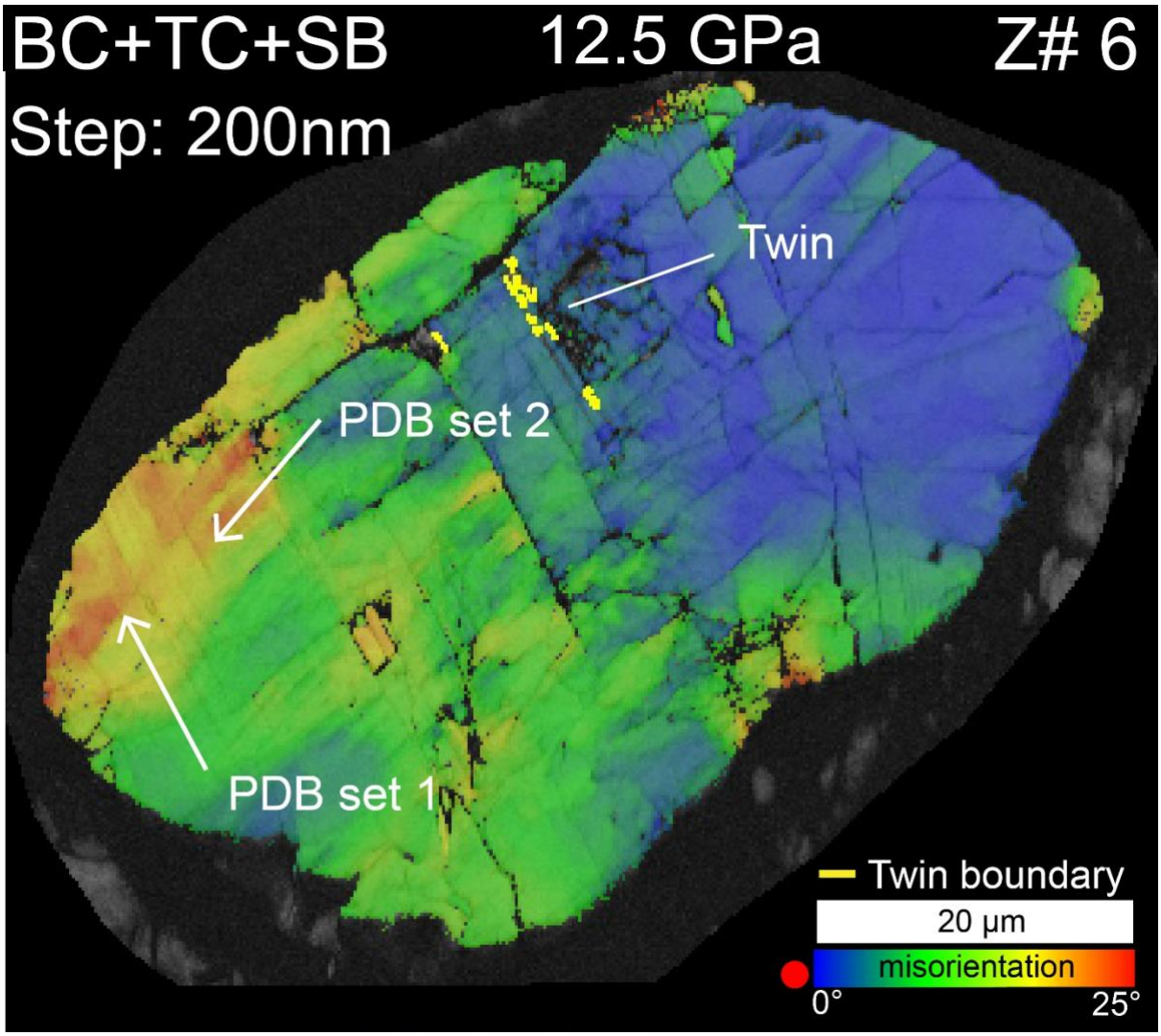
BC+TC+SB
12.5 GPa
Z# 6
Step: 200nm
Twin
PDB set 2
PDB set 1
Twin boundary
20 μm
misorientation
0°
25°

Figure 23

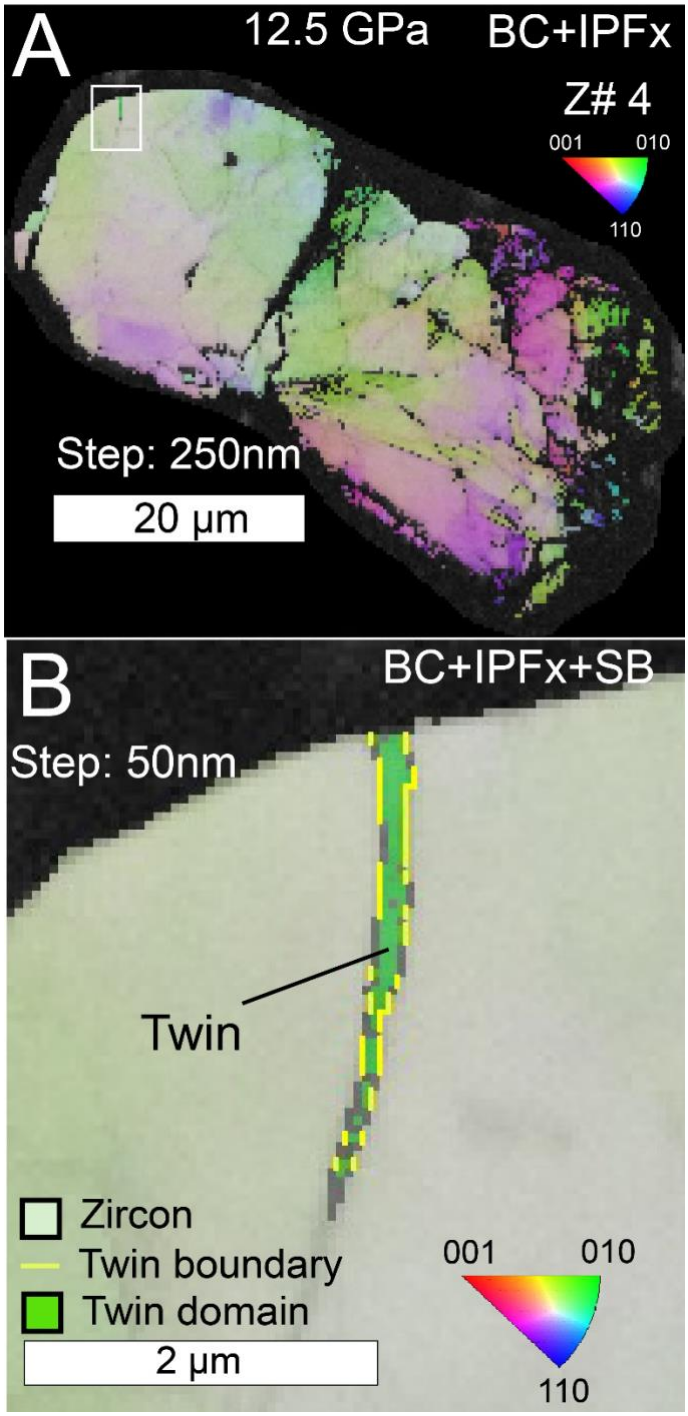
A
12.5 GPa
BC+IPFx
Z# 4
001
010
110
Step: 250nm
20 µm
B
BC+IPFx+SB
Step: 50nm
Twin
Zircon
Twin boundary
Twin domain
2 µm
001
010
110

Figure 24

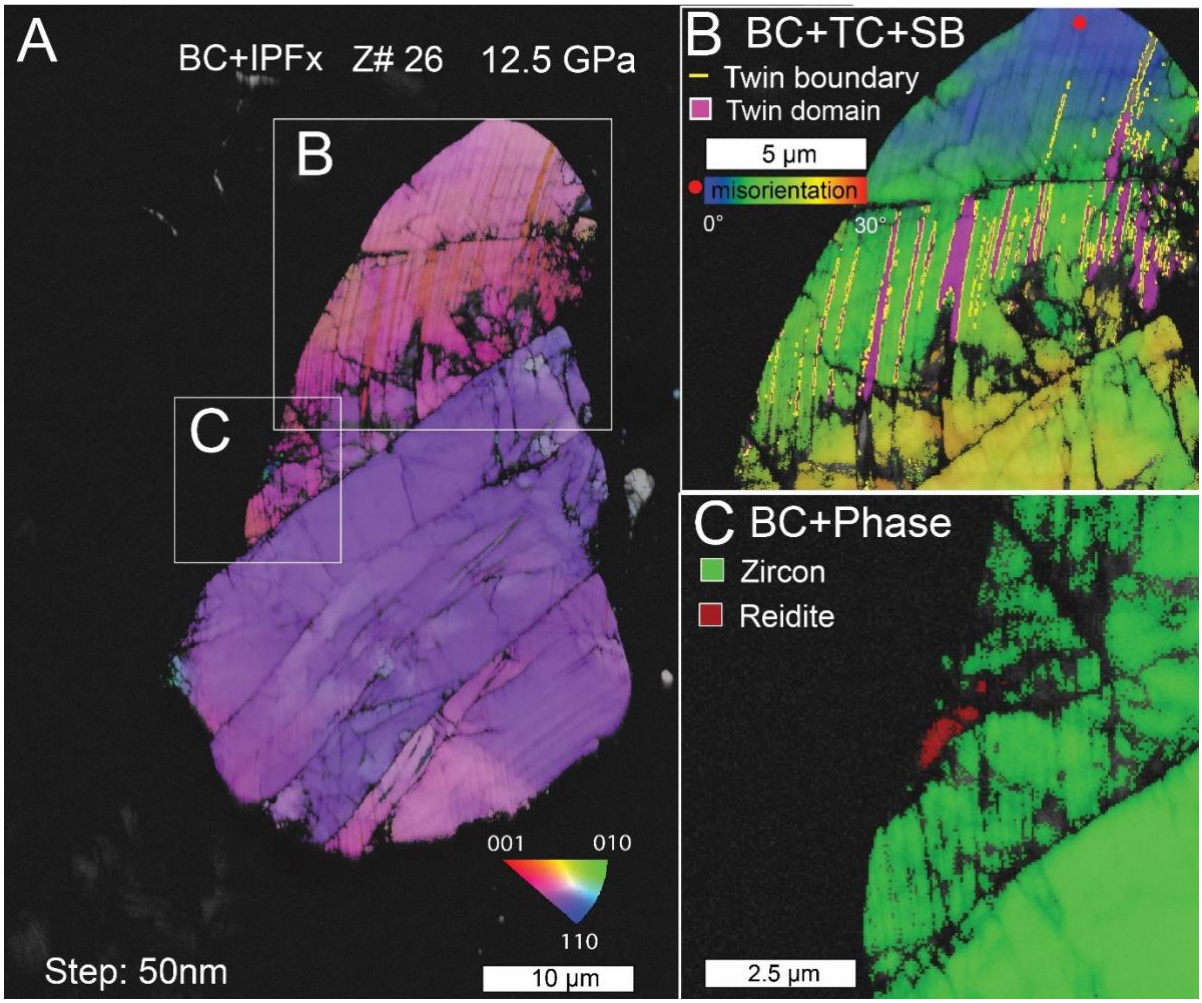
A
BC+IPFx Z# 26 12.5 GPa
B
C
001
010
110
10 µm
Step: 50nm
B BC+TC+SB
Twin boundary
Twin domain
5 µm
misorientation
0°
30°
C BC+Phase
Zircon
Reidite
2.5 µm

Figure 25

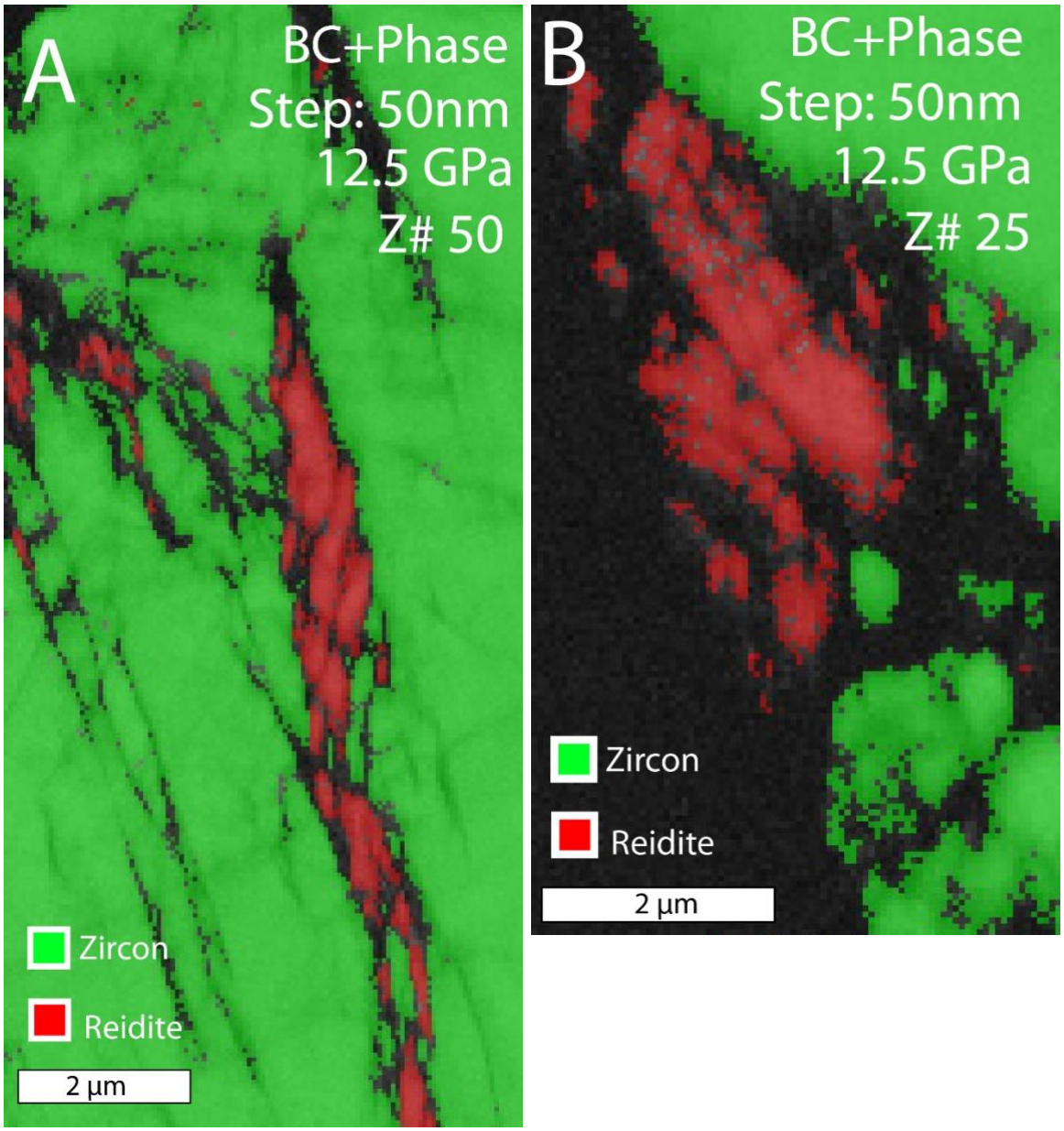
A
BC+Phase
Step: 50nm
12.5 GPa
Z# 50
Zircon
Reidite
2 µm
B
BC+Phase
Step: 50nm
12.5 GPa
Z# 25
Zircon
Reidite
2 µm

Figure 26

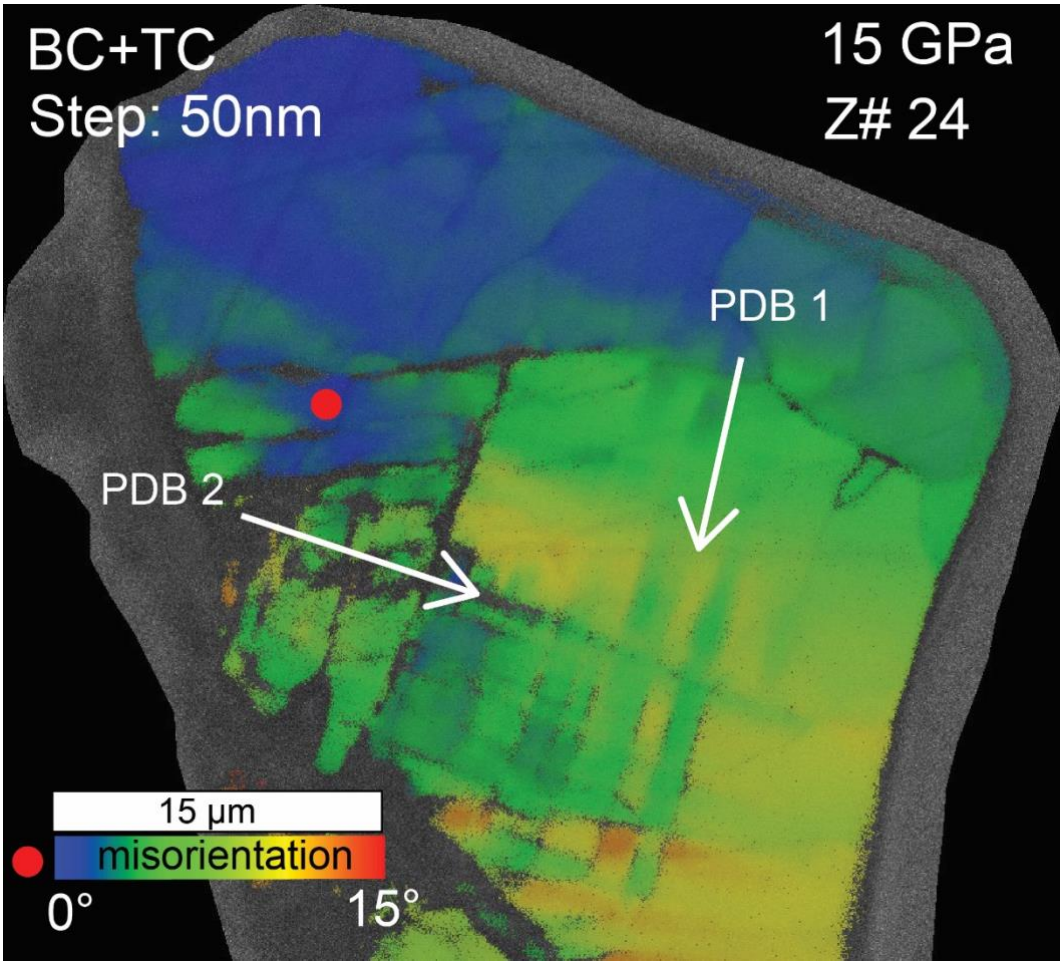

Figure 27

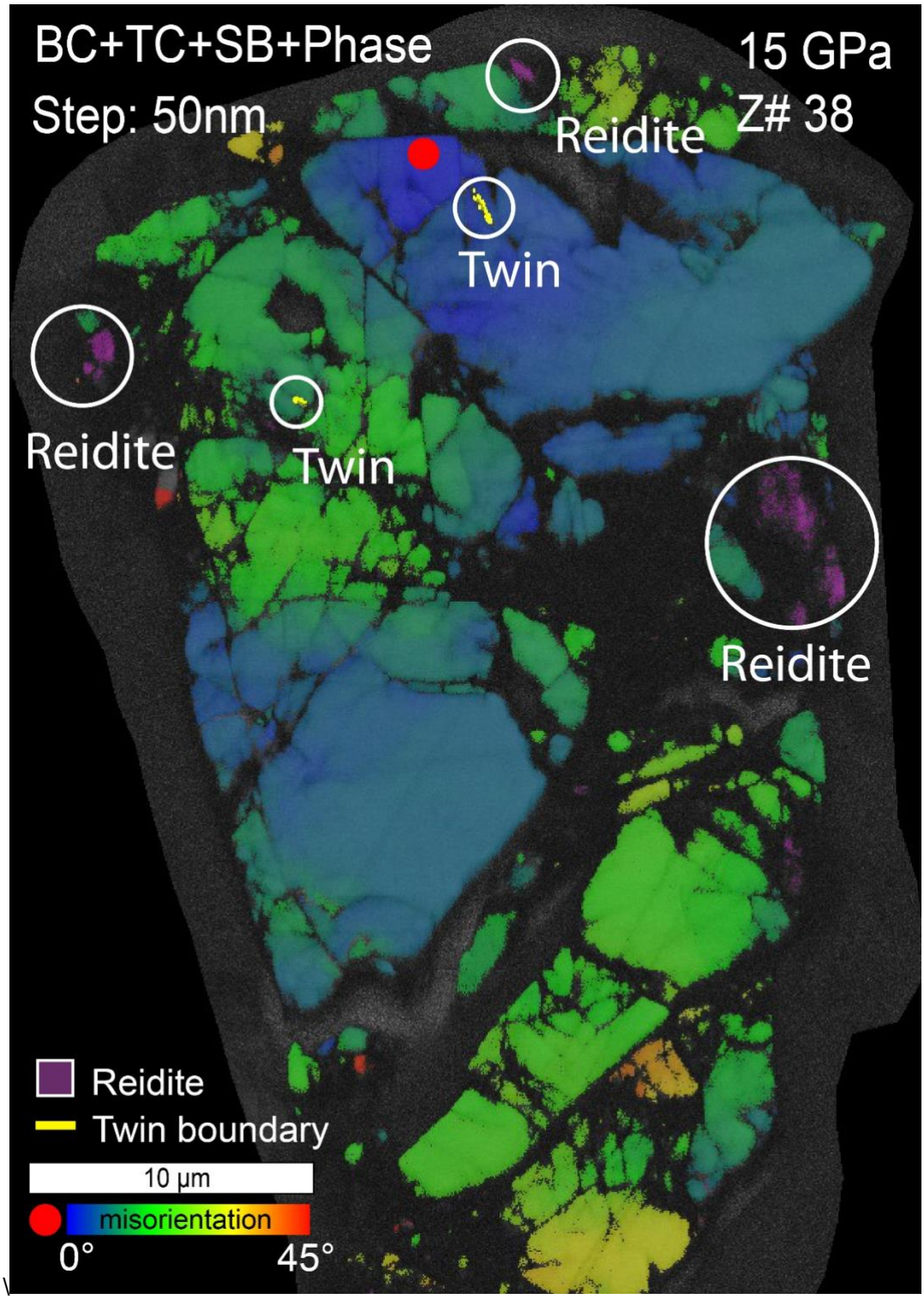
BC+TC+SB+Phase
Step: 50nm
15 GPa
Z# 38
Reidite
Twin
Reidite
Twin
Reidite
Reidite
Twin boundary
10 μm
misorientation
0°
45°

Figure 28

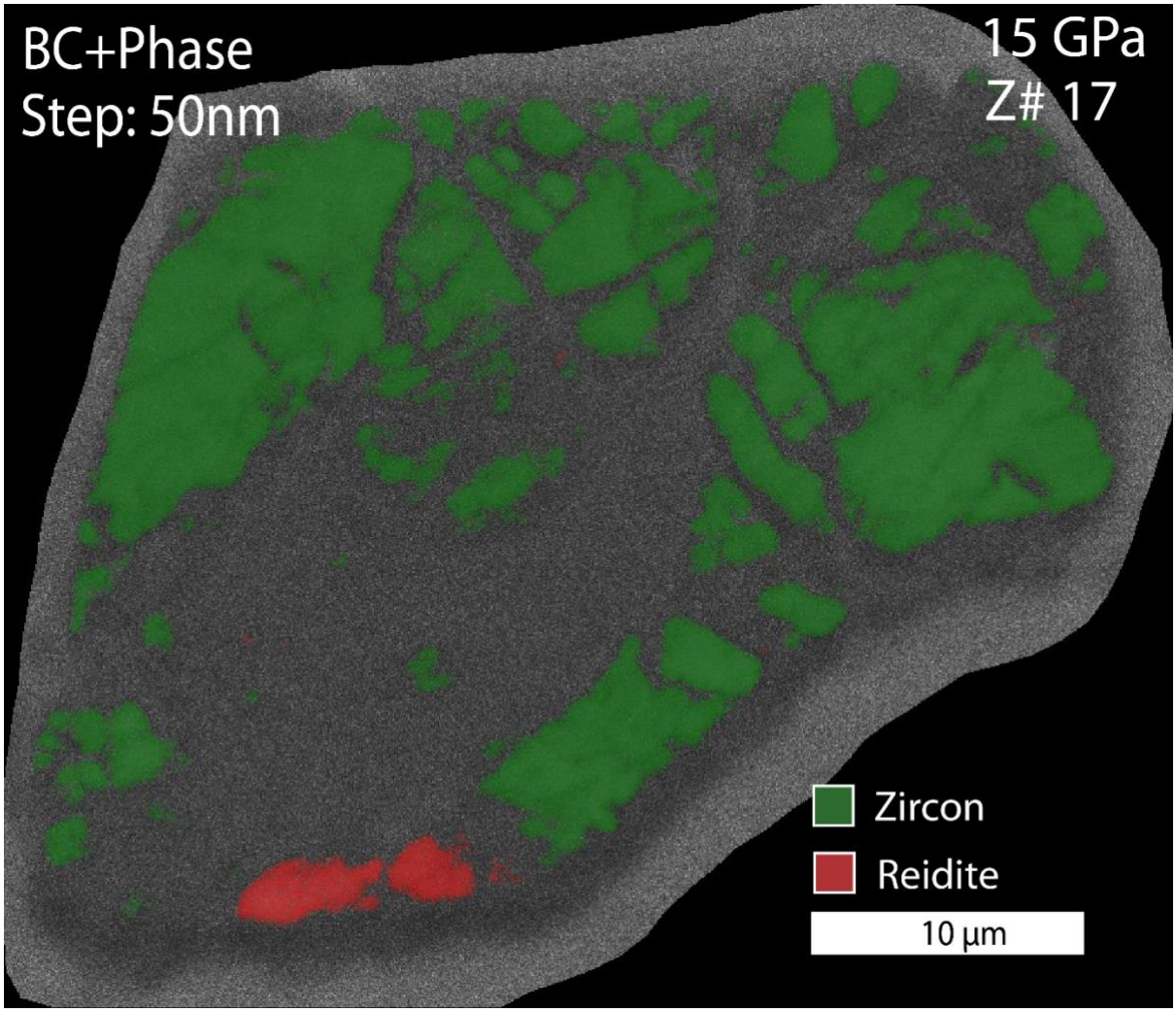

Figure 29

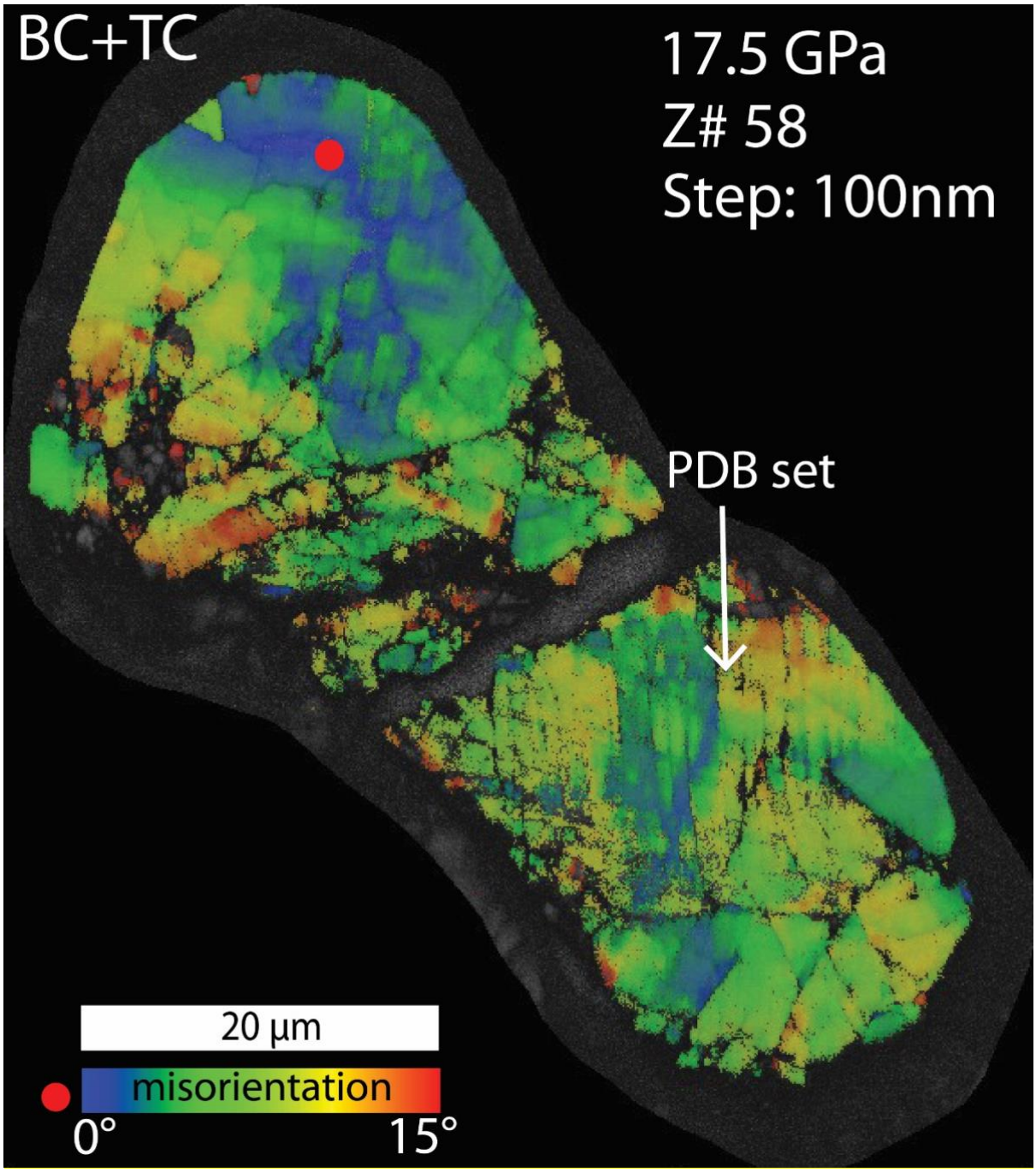

Figure 30

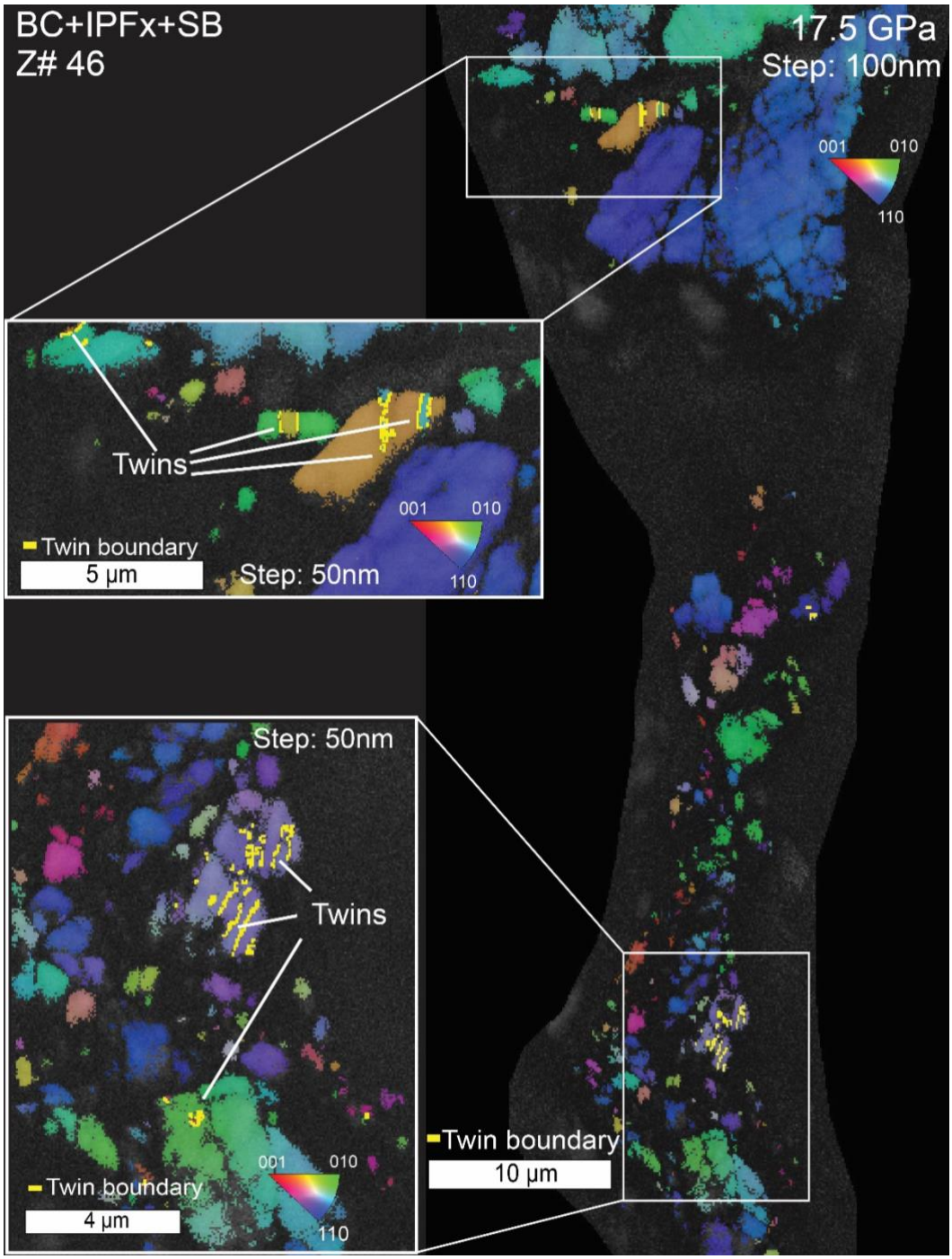
BC+IPFx+SB
Z# 46
17.5 GPa
Step: 100nm
001
010
110
Twins
Twin boundary
5 µm
Step: 50nm
001
010
110
Step: 50nm
Twins
Twin boundary
4 µm
001
010
110
Twin boundary
10 µm

Figure 31

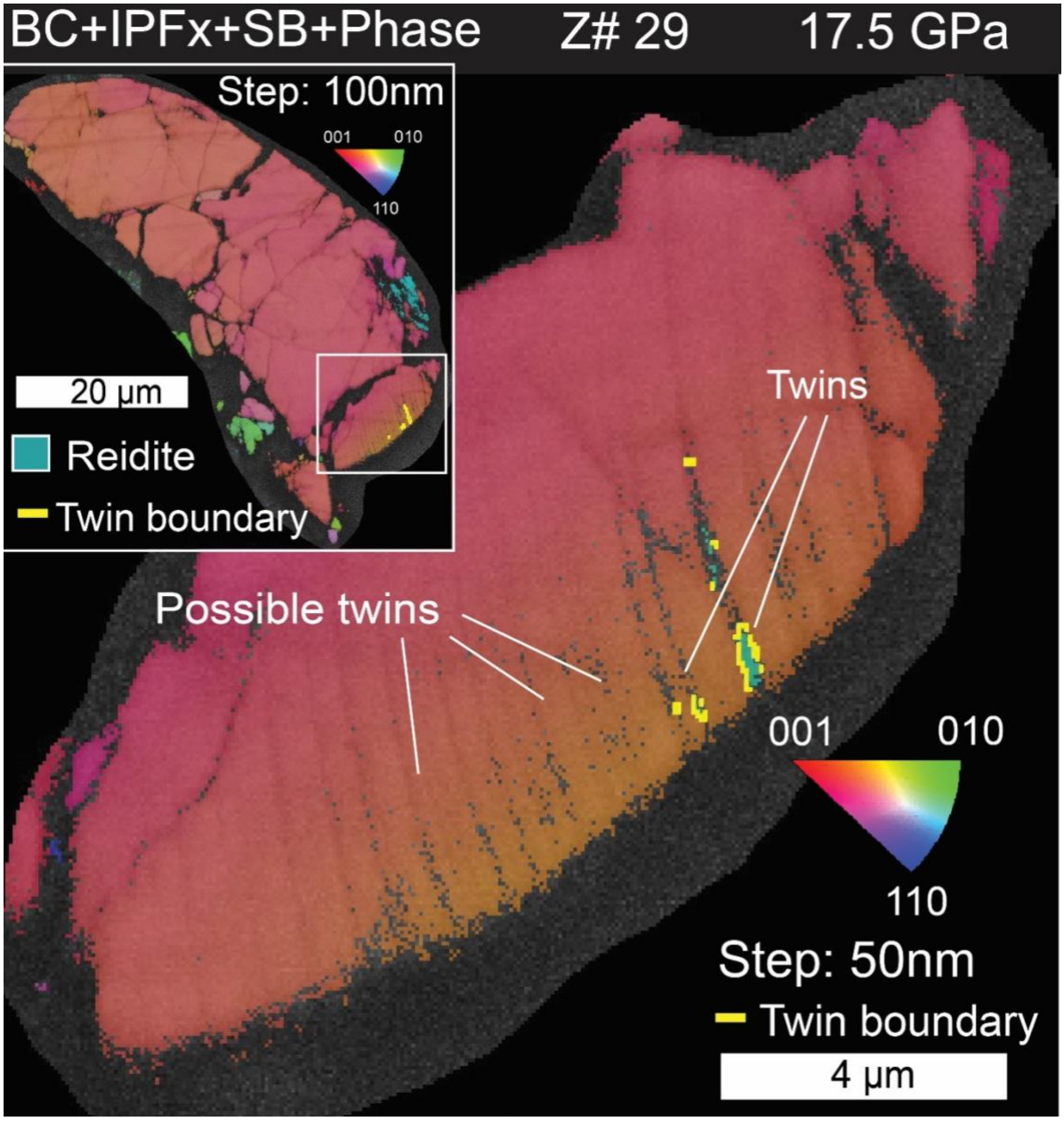
BC+IPFx+SB+Phase
Z# 29
17.5 GPa
Step: 100nm
001
010
110
20 μm
Reidite
Twin boundary
Twins
Possible twins
001
010
110
Step: 50nm
Twin boundary
4 μm

Figure 32

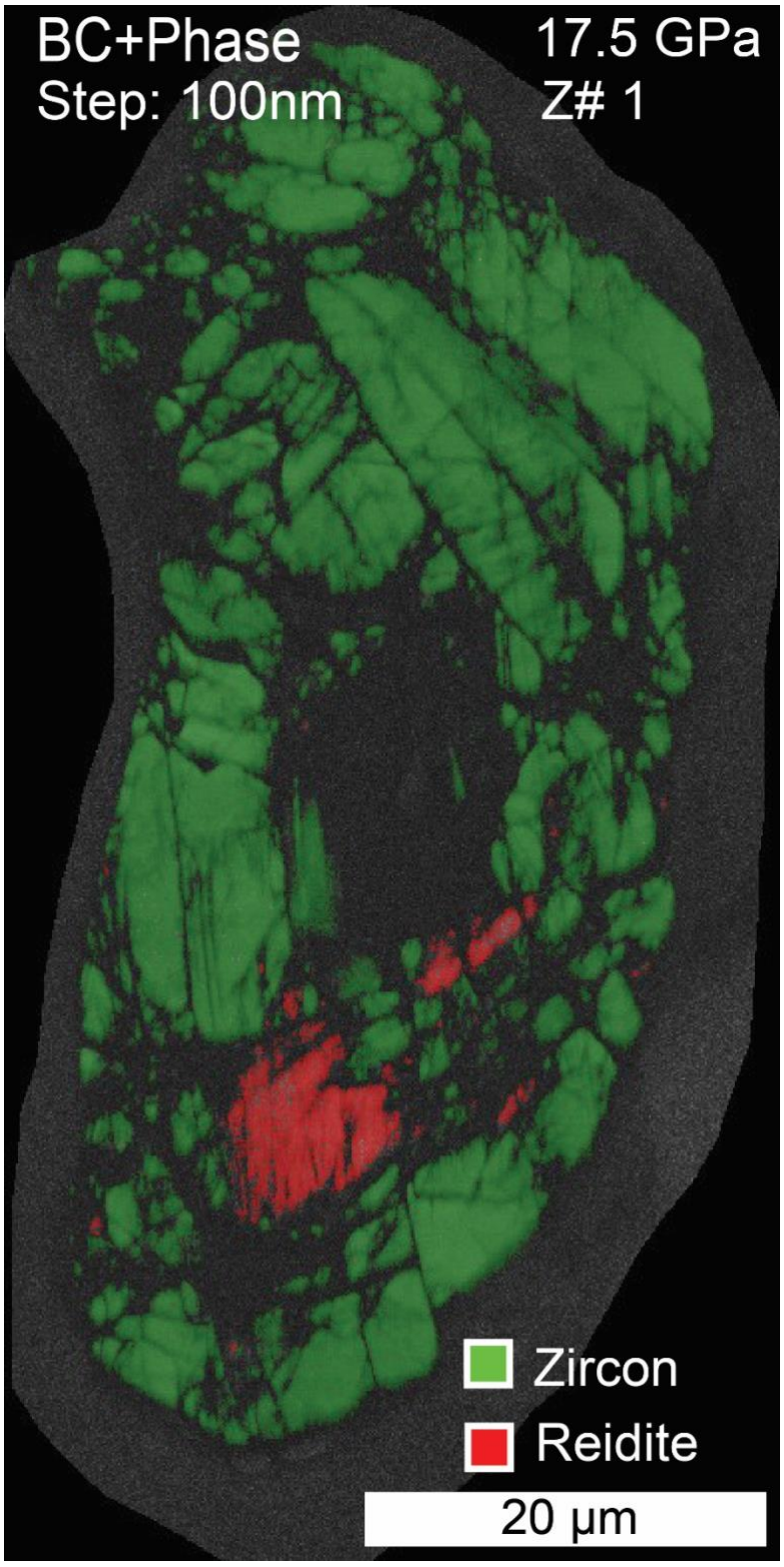

Figure 33

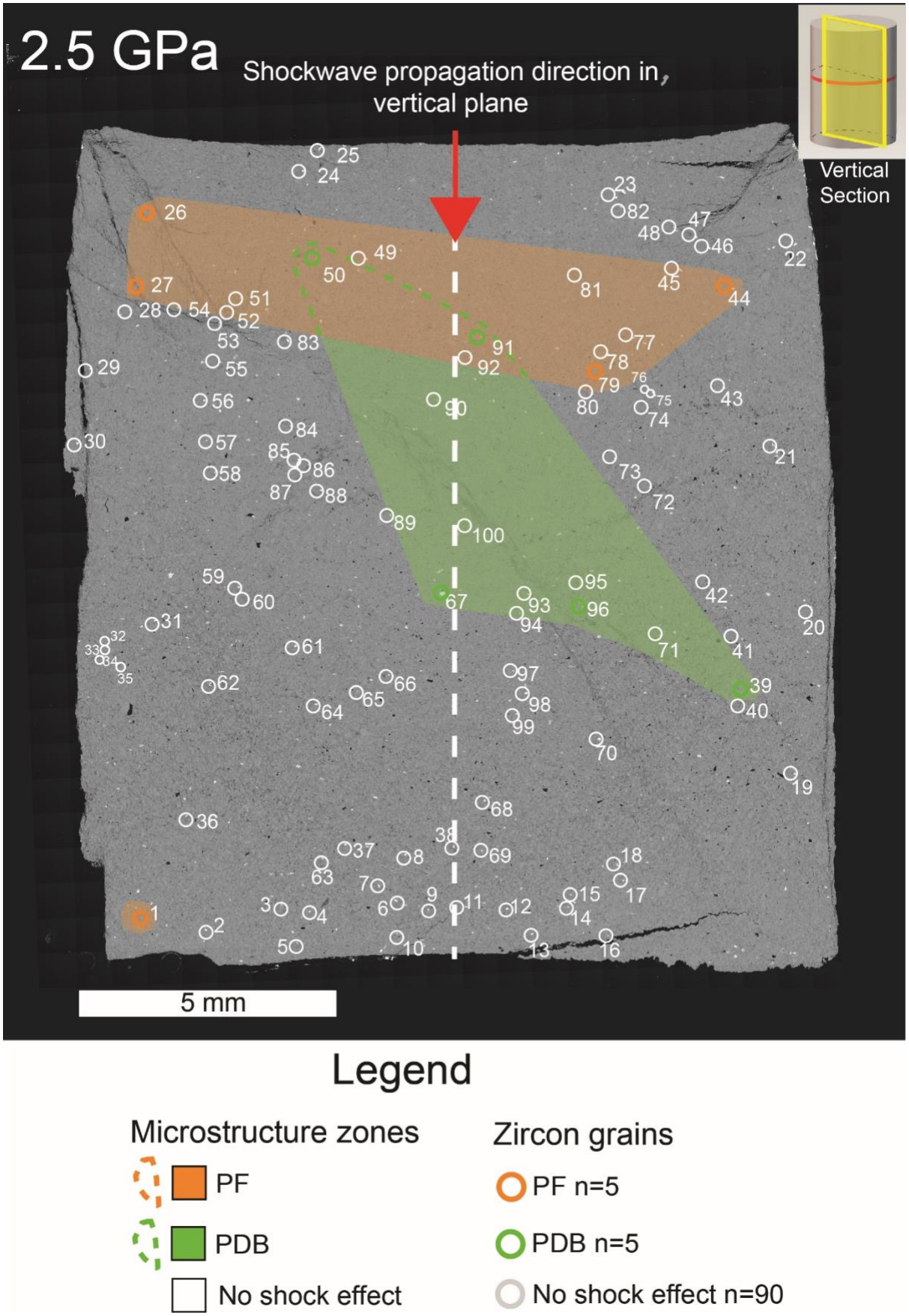
2.5 GPa
Shockwave propagation direction in vertical plane
Vertical Section
5 mm
Legend
Microstructure zones
PF
PDB
No shock effect
Zircon grains
PF n=5
PDB n=5
No shock effect n=90

Figure 34

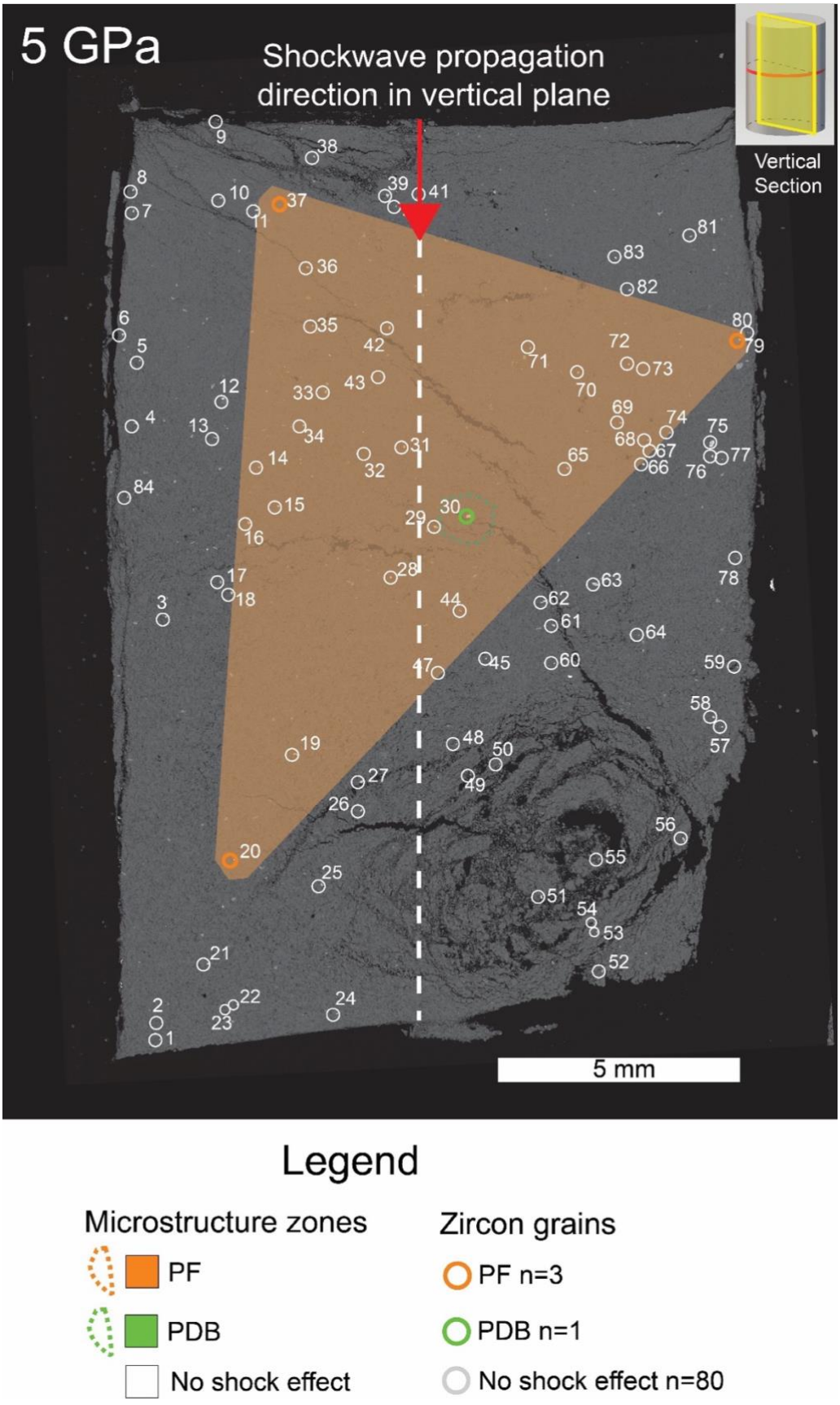
5 GPa
Shockwave propagation direction in vertical plane
Vertical Section
5 mm
Legend
Microstructure zones
PF
PDB
No shock effect
Zircon grains
PF n=3
PDB n=1
No shock effect n=80

Figure 35

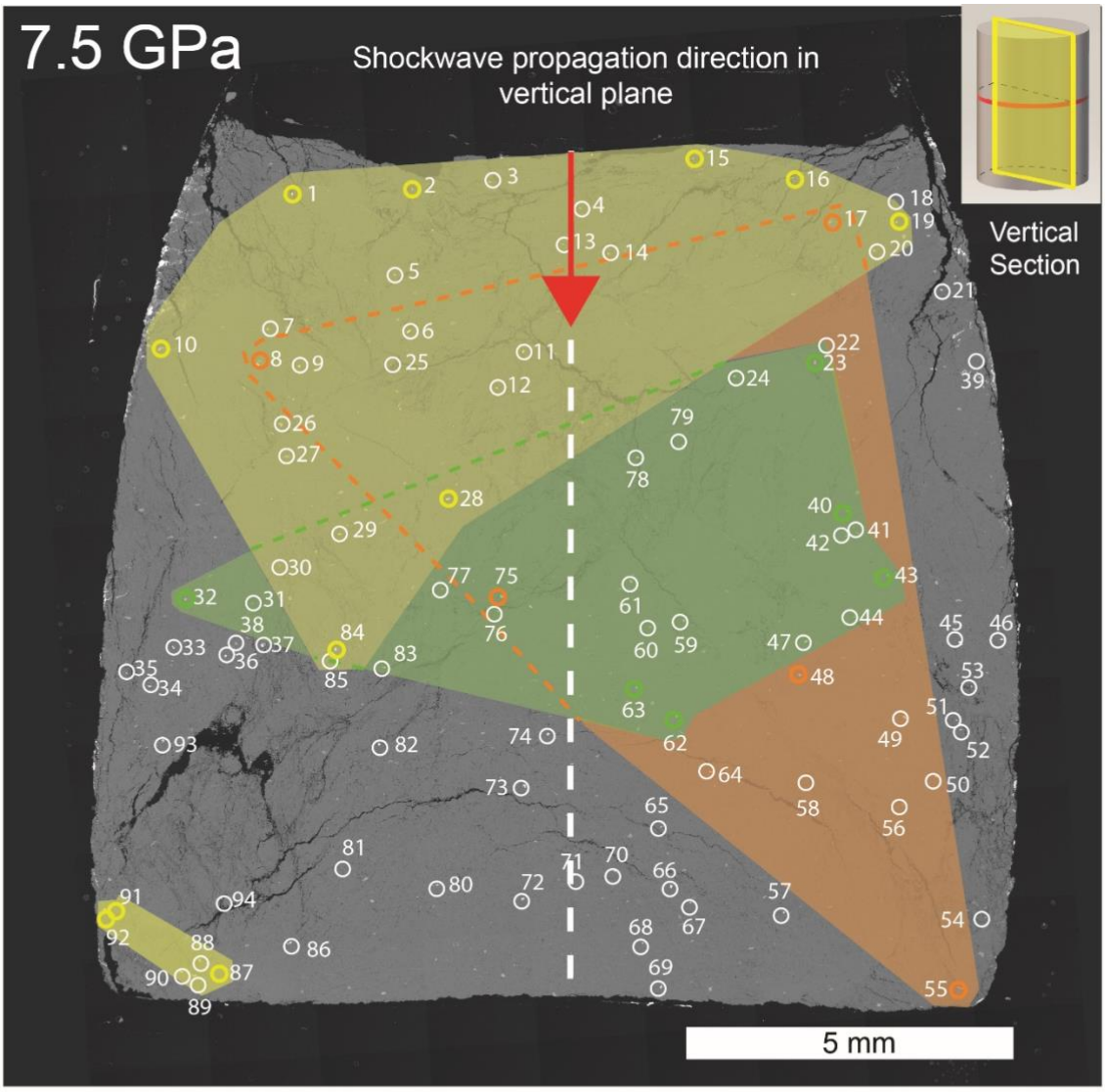
7.5 GPa
Shockwave propagation direction in vertical plane
Vertical Section
5 mm
Legend
Microstructure zones
Melt film
PF
PDB
No shock effect
Zircon grains
Melt film n=11
PF n=5
PDB n=6
No shock effect n=83

Figure 36

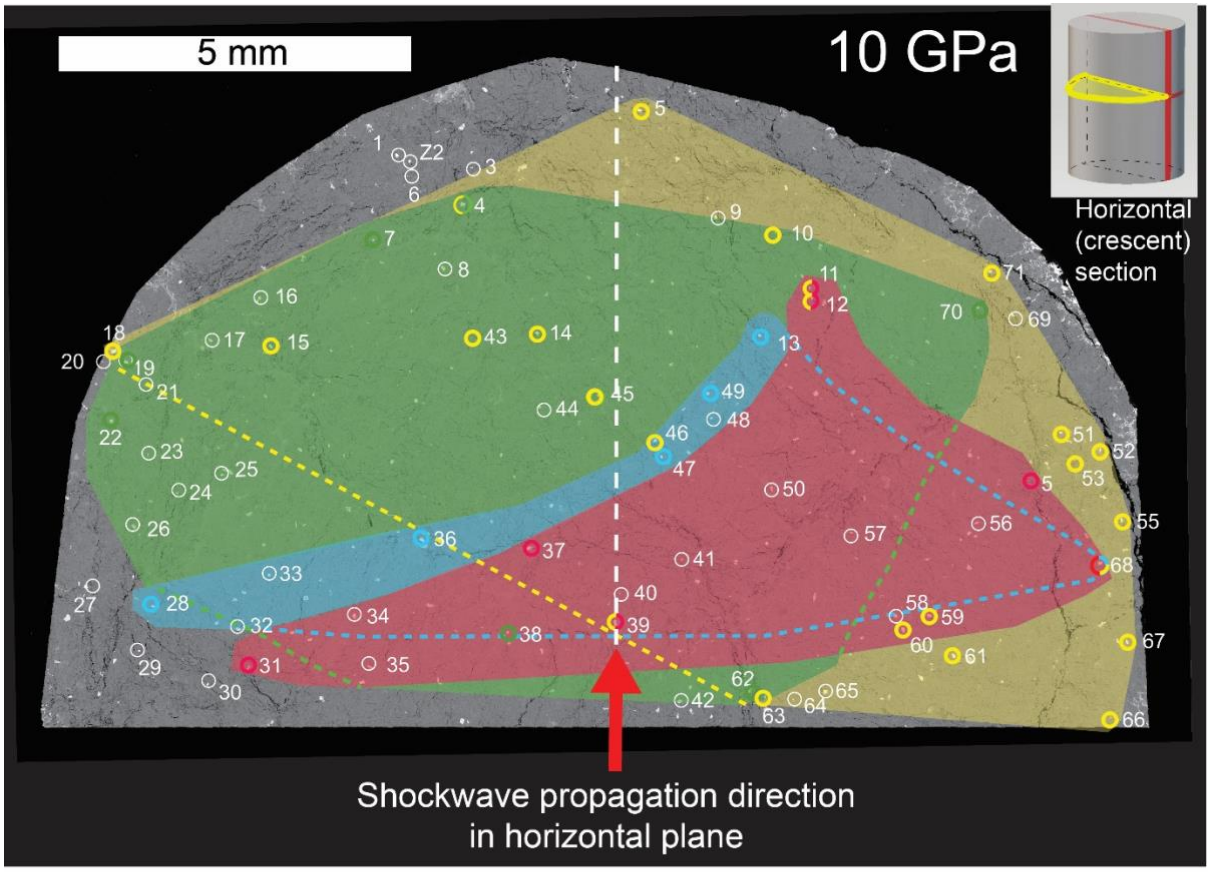

Legend

Microstructure zones

- Reidite
- Twins
- Melt film
- PDB
- No shock effect

Zircon grains

- Reidite n=7
- Twins n=6
- Melt film n=24
- PDB n=7
- No shock effect n=52

Figure 37

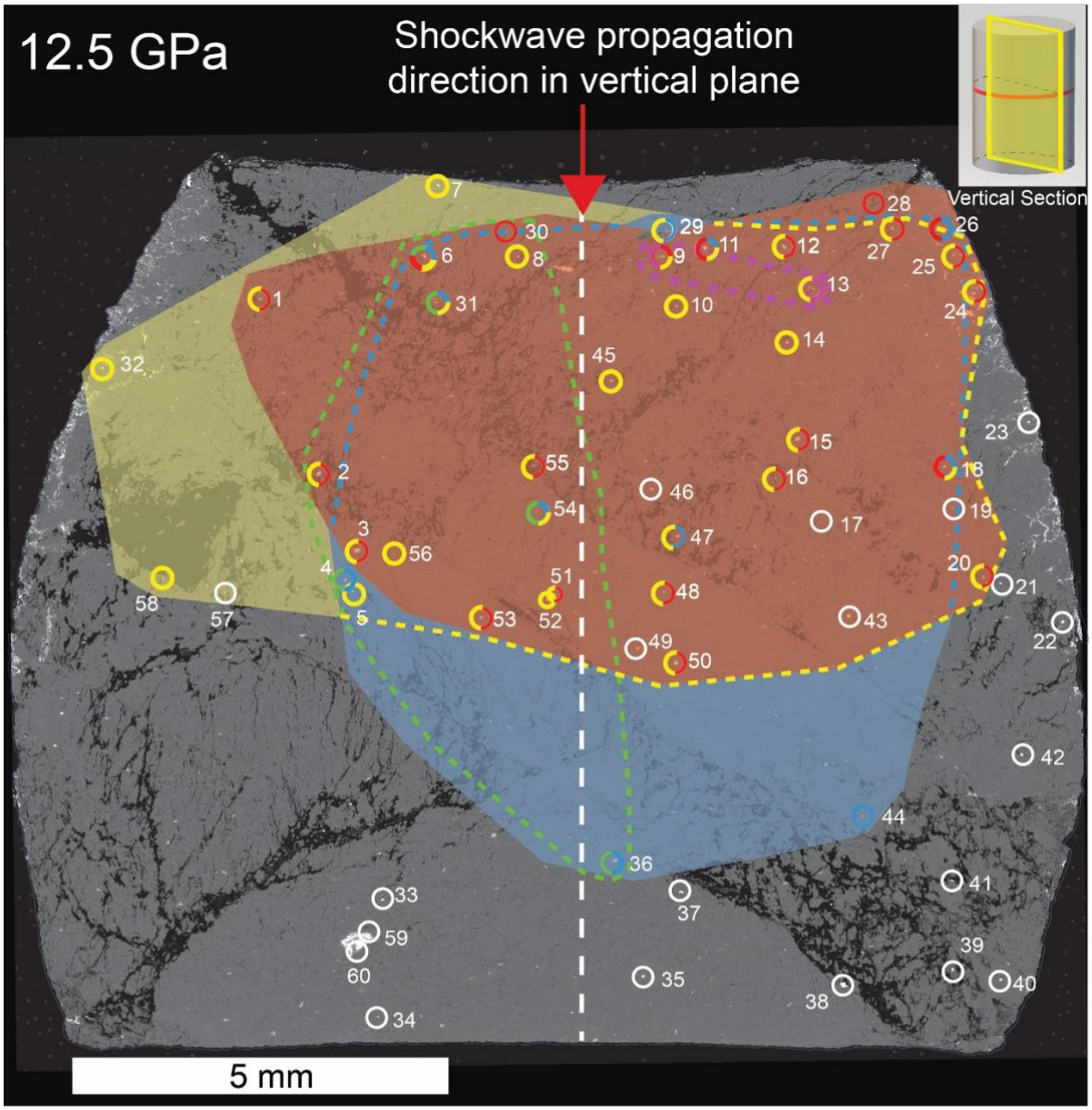
12.5 GPa
Shockwave propagation direction in vertical plane
Vertical Section
5 mm
Legend
Microstructure zones
Dissociation
PDB
Reidite
Melt film
Twins
No shock effect
Zircon grains
Dissociation n = 2
PDB n = 5
Reidite n = 20
Melt film n=32
Twin n = 11
No shock effect n=31

Figure 38

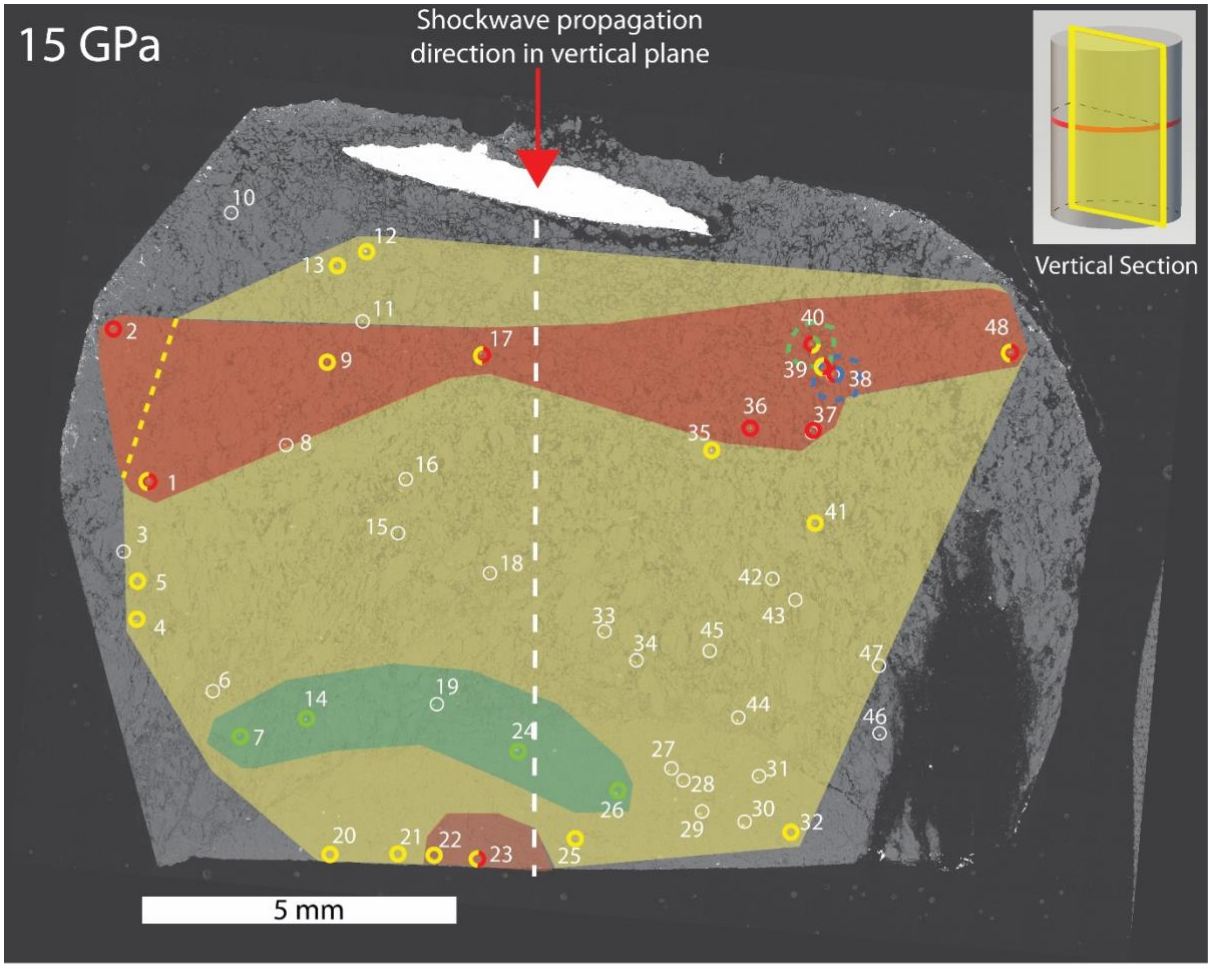
15 GPa
Shockwave propagation direction in vertical plane
Vertical Section
5 mm
Legend
Microstructure zones
Reidite
Twins
PDB
Melt film
No shock effect
Zircon grains
Reidite n=10
Twins n=1
PDB n=5
Melt film n=18
No shock effect n=34

Figure 39

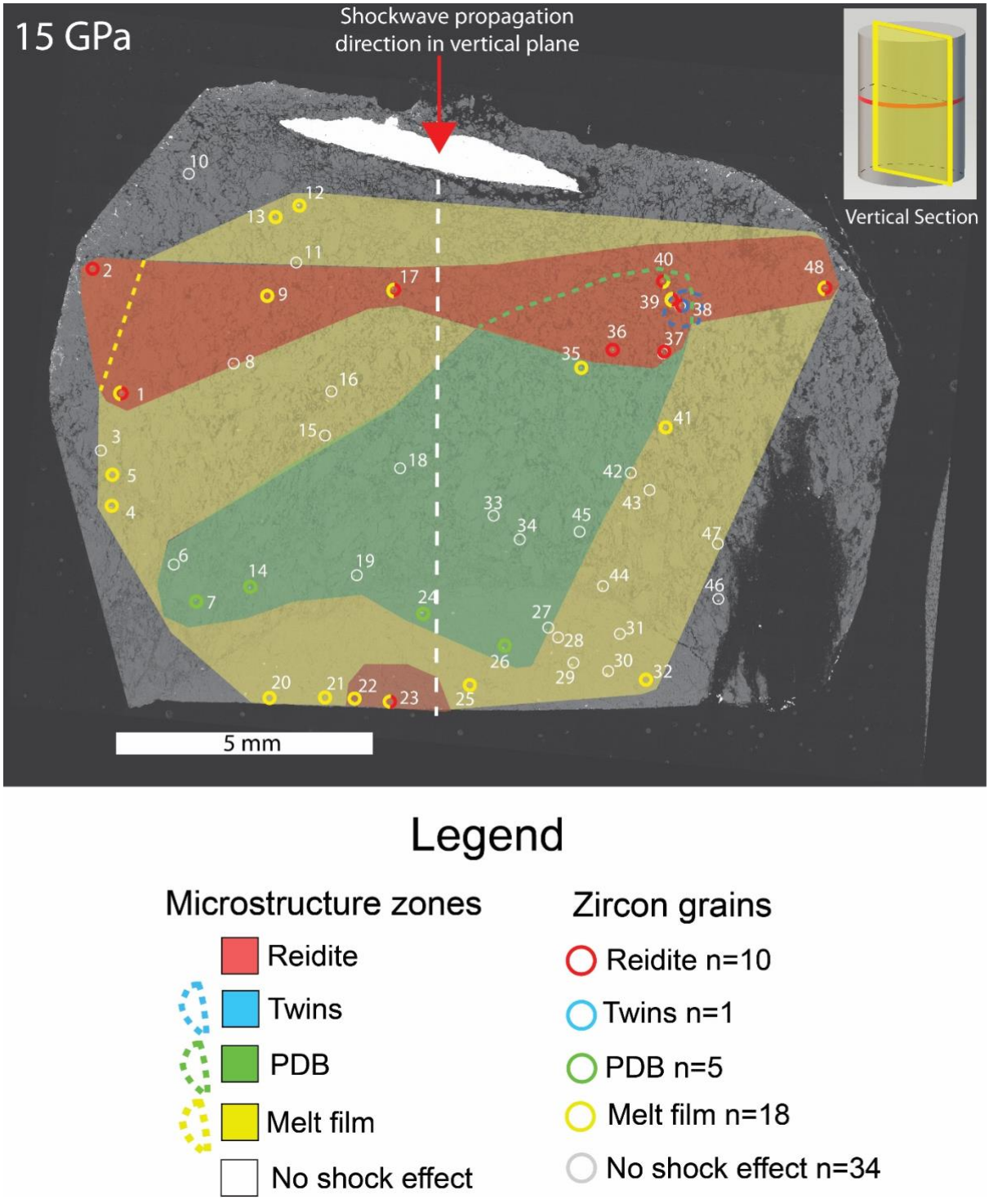

Figure 39 (cont.)

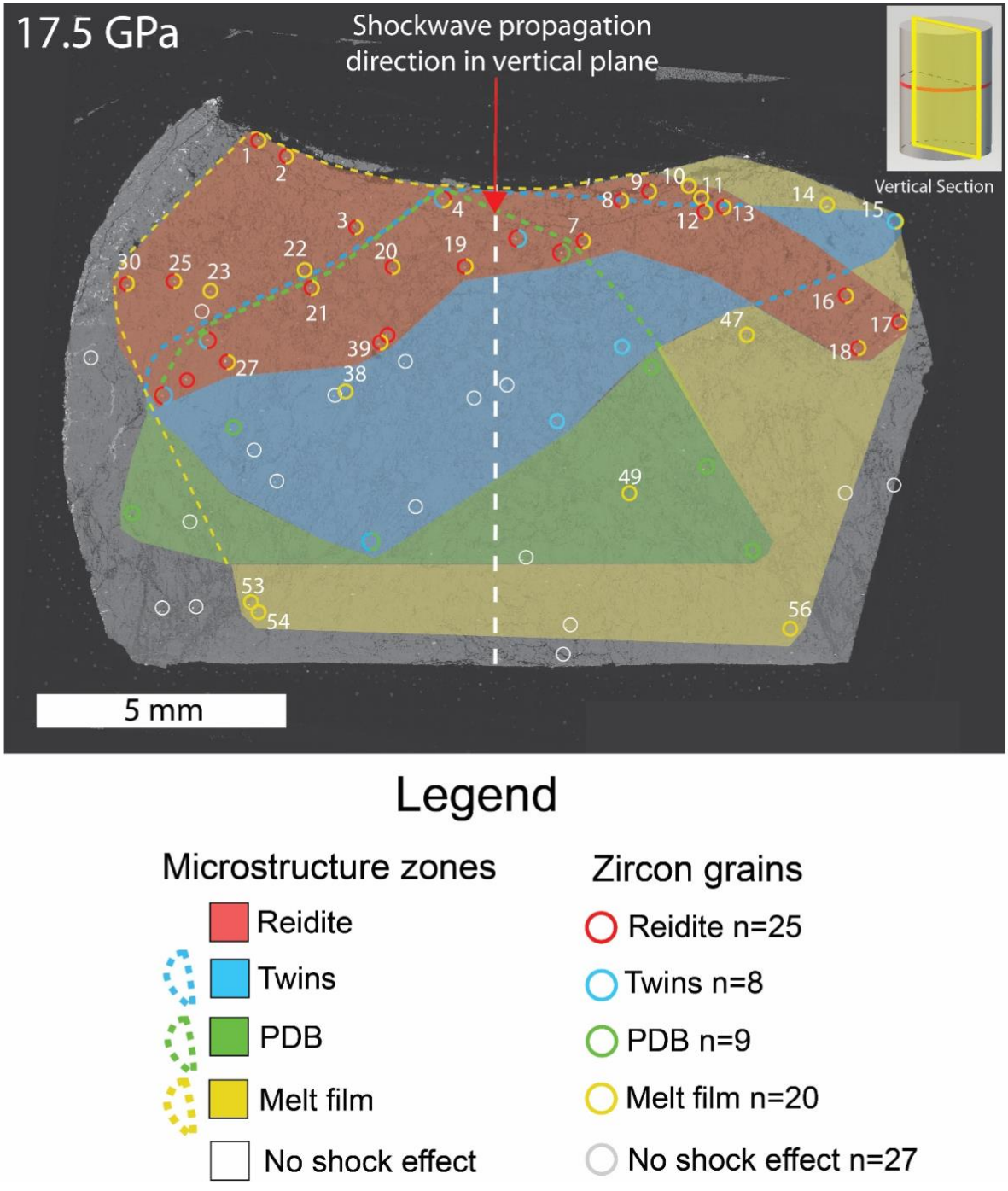
17.5 GPa
Shockwave propagation direction in vertical plane
Vertical Section
5 mm
Legend
Microstructure zones
Reidite
Twins
PDB
Melt film
No shock effect
Zircon grains
Reidite n=25
Twins n=8
PDB n=9
Melt film n=20
No shock effect n=27

Figure 40

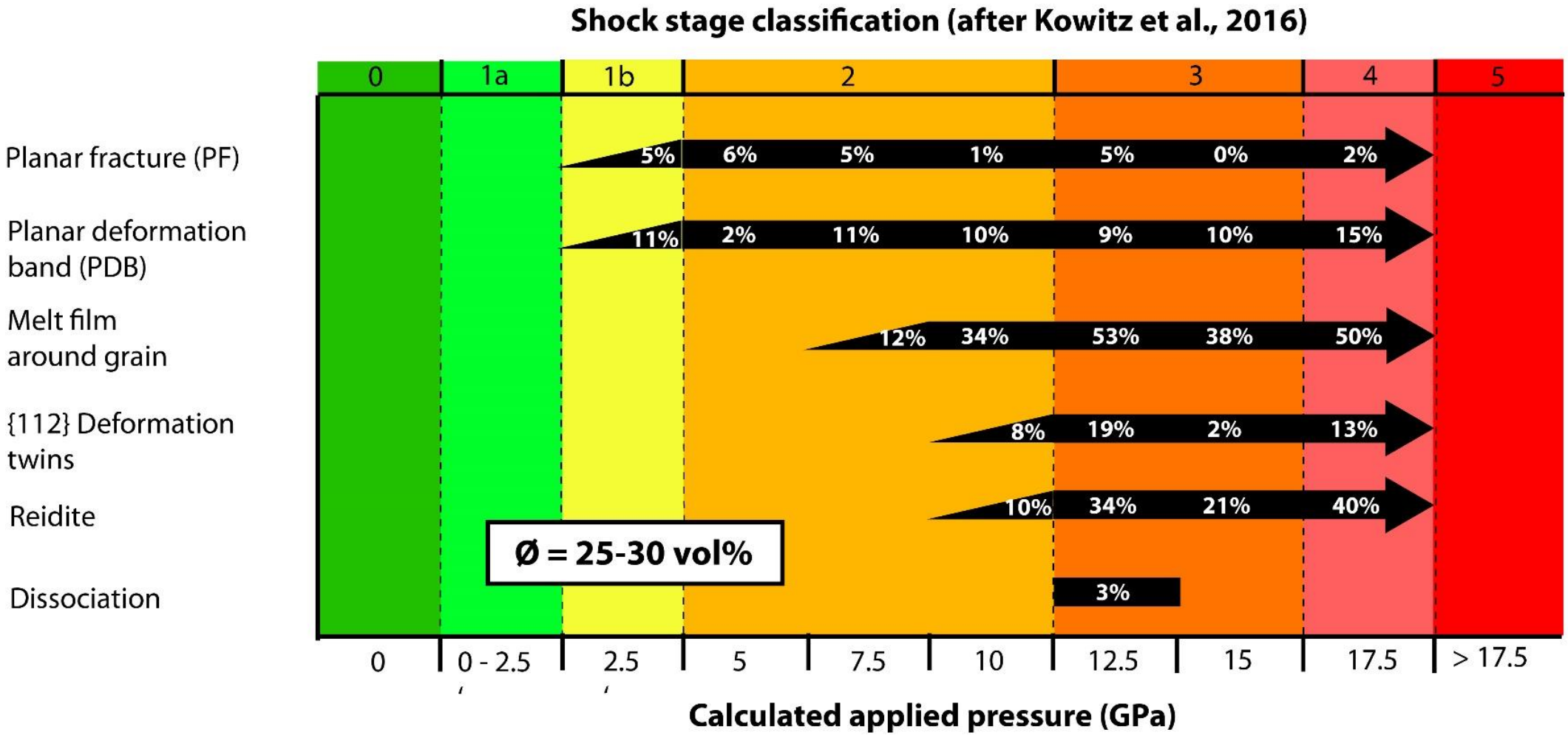
Shock stage classification (after Kowitz et al., 2016)
0
1a
1b
2
3
4
5
Planar fracture (PF)
Planar deformation band (PDB)
Melt film around grain
{112} Deformation twins
Reidite
Dissociation
5%
6%
5%
1%
5%
0%
2%
11%
2%
11%
10%
9%
10%
15%
12%
34%
53%
38%
50%
8%
19%
2%
13%
10%
34%
21%
40%
3%
Ø = 25-30 vol%
0
0 - 2.5
2.5
5
7.5
10
12.5
15
17.5
> 17.5
Calculated applied pressure (GPa)

Figure 41

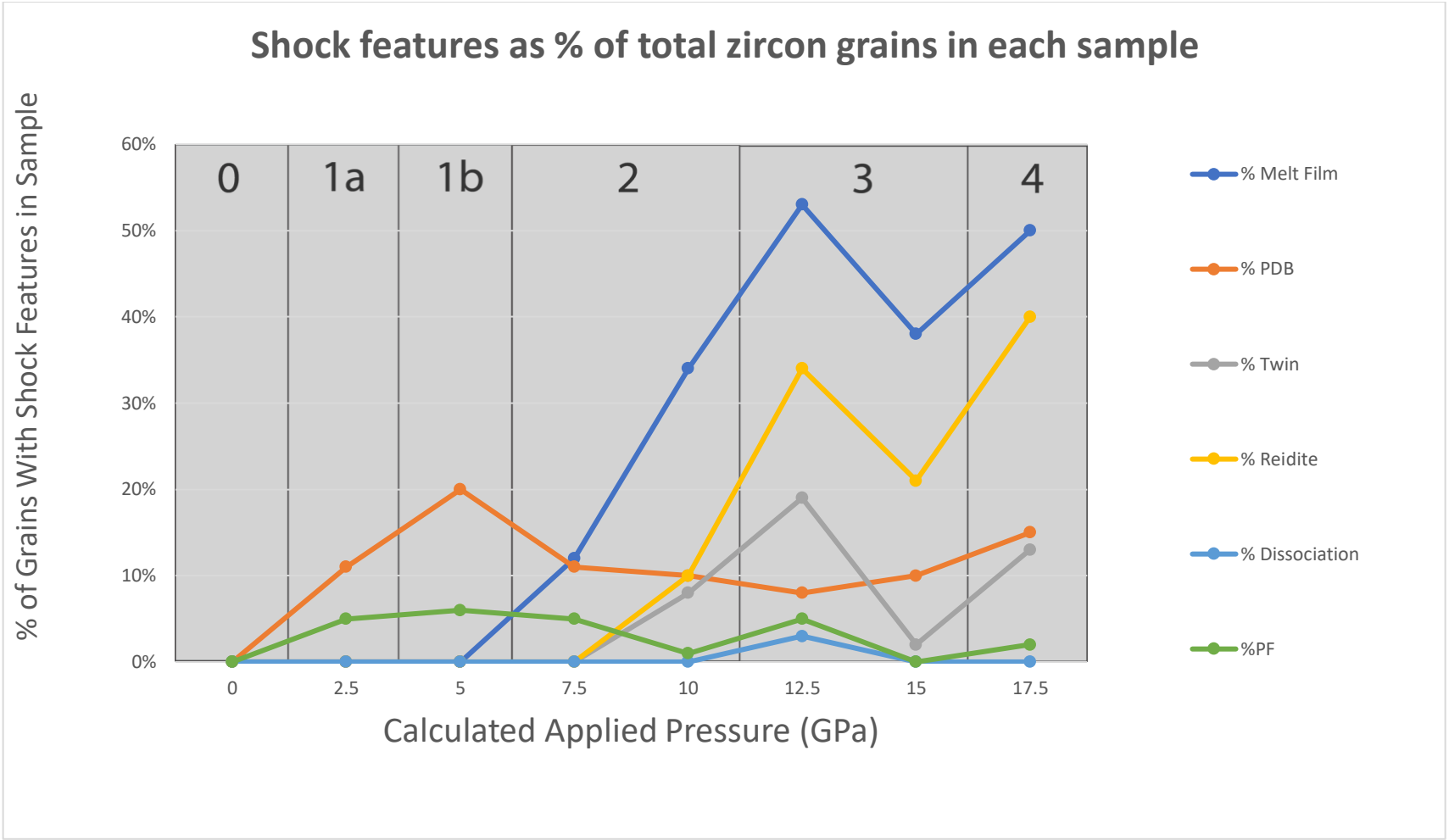
Shock features as % of total zircon grains in each sample
% of Grains With Shock Features in Sample
60%
50%
40%
30%
20%
10%
0%
0
1a
1b
2
3
4
0
2.5
5
7.5
10
12.5
15
17.5
Calculated Applied Pressure (GPa)
% Melt Film
% PDB
% Twin
% Reidite
% Dissociation
%PF

Figure 42

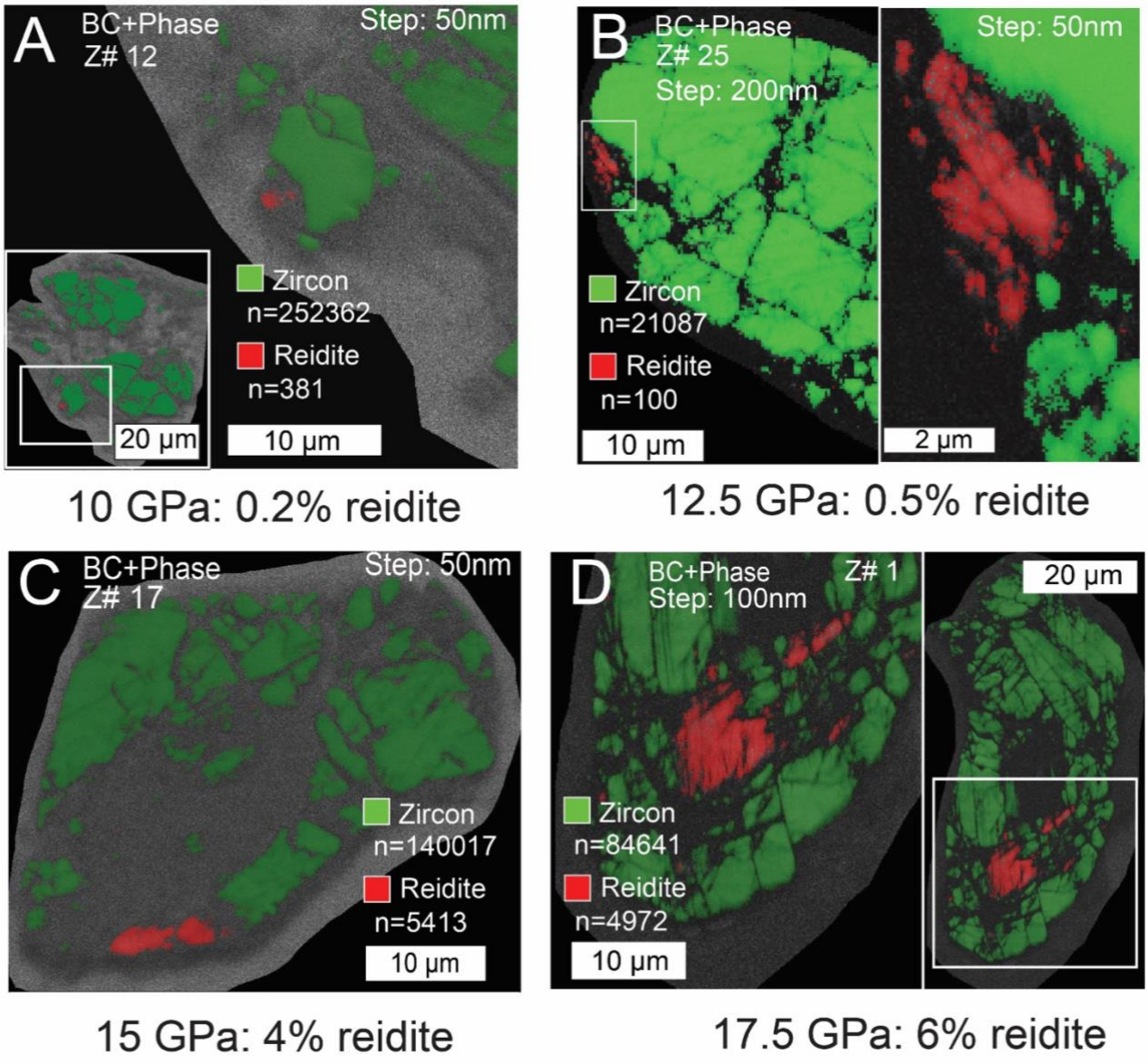
A
BC+Phase
Z# 12
Step: 50nm
Zircon
n=252362
Reidite
n=381
20 μm
10 μm
10 GPa: 0.2% reidite
B
BC+Phase
Z# 25
Step: 200nm
Step: 50nm
Zircon
n=21087
Reidite
n=100
10 μm
2 μm
12.5 GPa: 0.5% reidite
C
BC+Phase
Z# 17
Step: 50nm
Zircon
n=140017
Reidite
n=5413
10 μm
15 GPa: 4% reidite
D
BC+Phase
Step: 100nm
Z# 1
20 μm
Zircon
n=84641
Reidite
n=4972
10 μm
17.5 GPa: 6% reidite

Figure 43

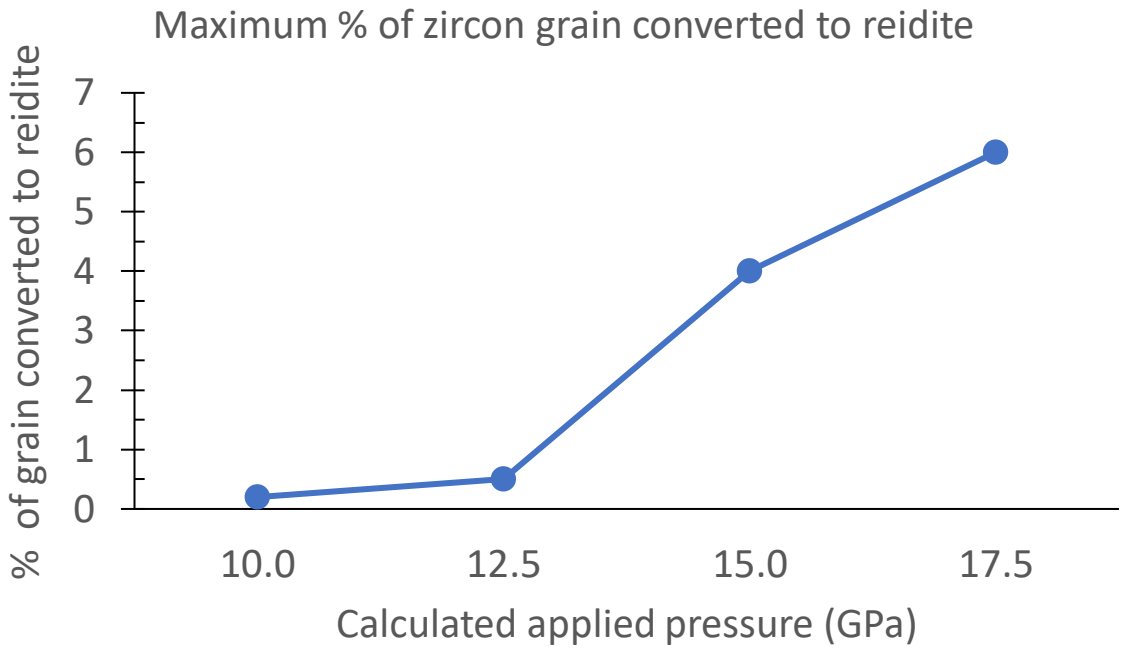
Maximum % of zircon grain converted to reidite
% of grain converted to reidite
7
6
5
4
3
2
1
0
10.0
12.5
15.0
17.5
Calculated applied pressure (GPa)

Figure 44

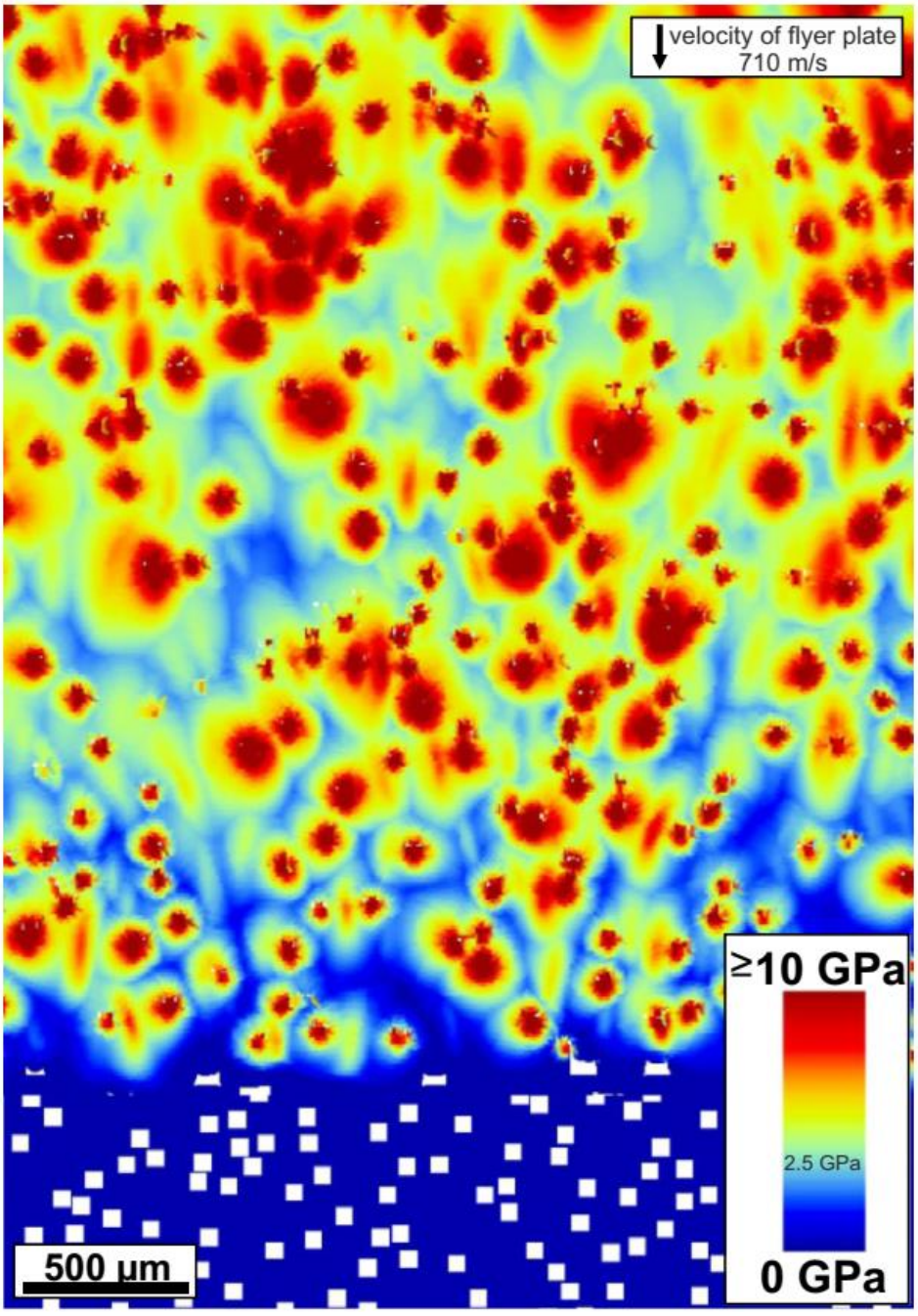

Figure 45

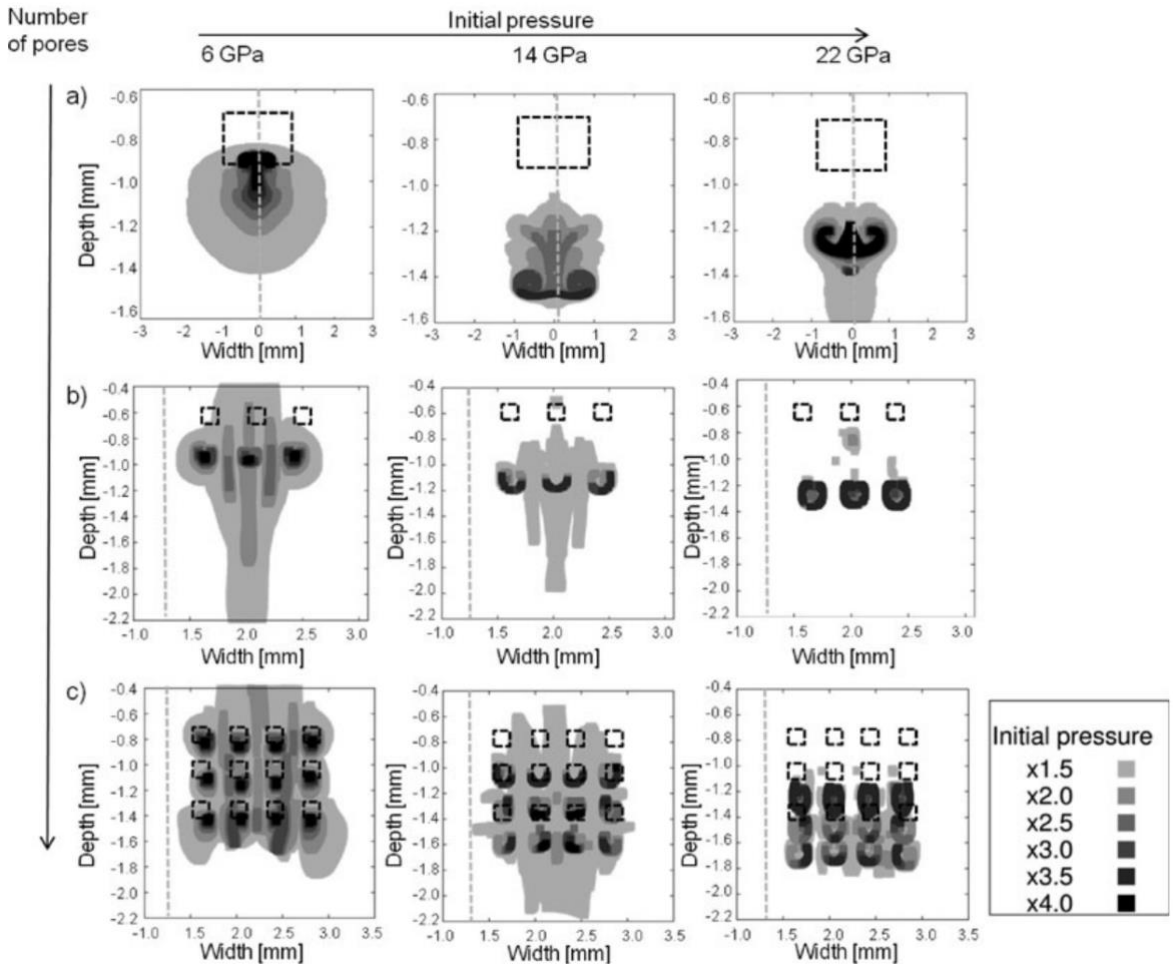
Number of pores
Initial pressure
6 GPa
14 GPa
22 GPa
a)
b)
c)
Depth [mm]
Width [mm]
Initial pressure
x1.5
x2.0
x2.5
x3.0
x3.5
x4.0

Figure 46

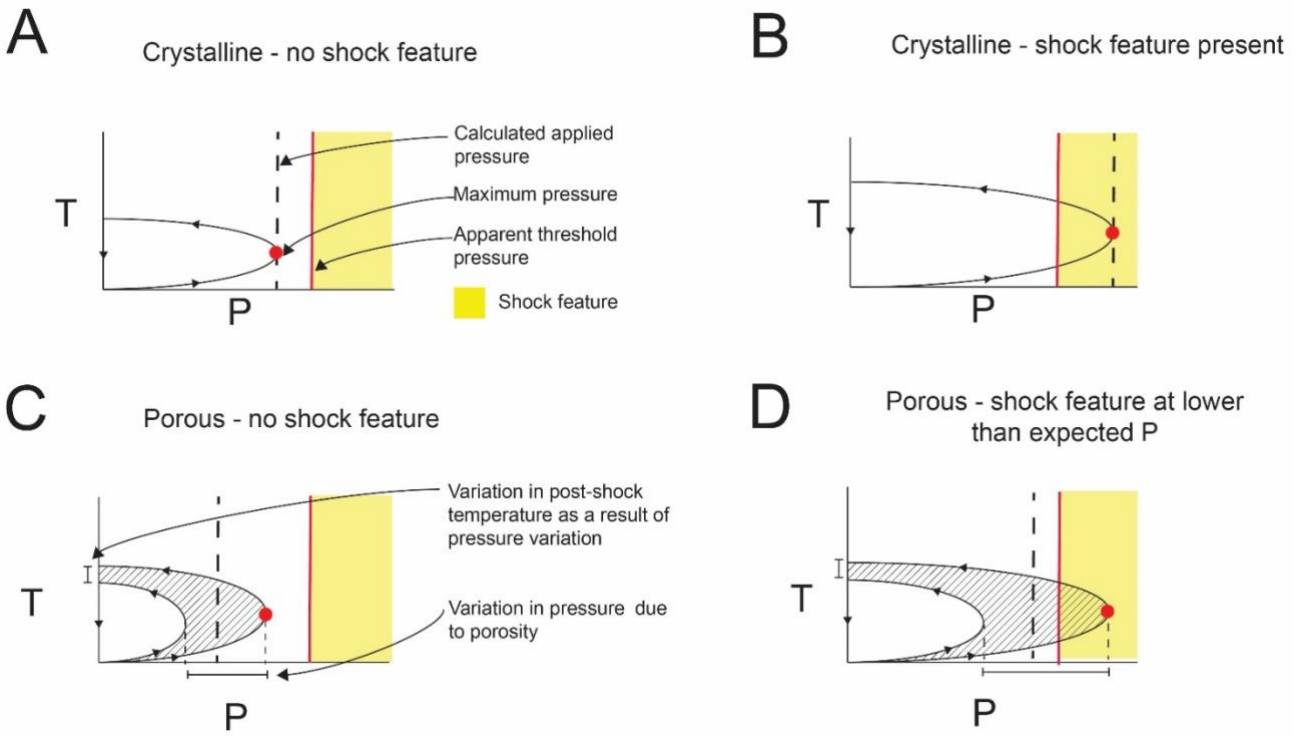
A
Crystalline - no shock feature
Calculated applied pressure
Maximum pressure
Apparent threshold pressure
Shock feature
T
P
B
Crystalline - shock feature present
T
P
C
Porous - no shock feature
Variation in post-shock temperature as a result of pressure variation
Variation in pressure due to porosity
T
P
D
Porous - shock feature at lower than expected P
T
P

Figure 47

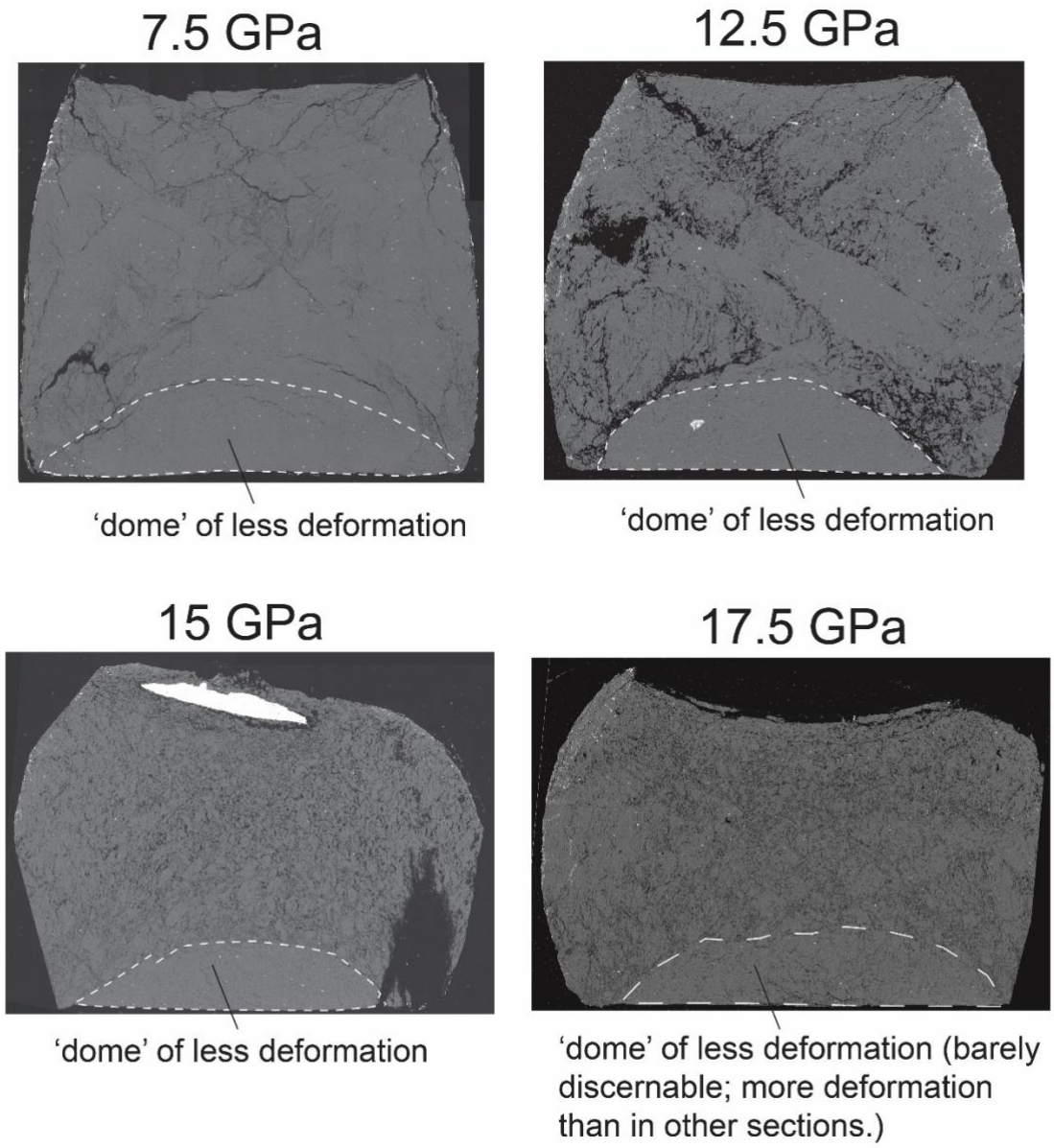
7.5 GPa
'dome' of less deformation
12.5 GPa
'dome' of less deformation
15 GPa
'dome' of less deformation
17.5 GPa
'dome' of less deformation (barely discernable; more deformation than in other sections.)

Figure 48

10 - Tables

Table 1 – Summary table showing the area, number of zircons, number of zircons analysed in EBSD and relevant shock metamorphic features.

Sample details					BSE analysis						EBSD analysis							
sample (GPa)	area (mm^2)	no. Zrn	Zrn /mm^2	no. Zrn analysed in EBSD	no. PF	PF (%)	no. melt film	melt film (%)	no. dissoc.	dissoc. (%)	no. PDB	PDB (%)	no. twin	twin (%)	no. reidite	reidite (%)	twin + reidite (no.)	Melt film + twin/ reidite (no.)
0	302	78	0.26	13	0	0	0	0	0	0	0	0	0	0	0	0	0	0
2.5	332	100	0.3	47	5	5	0	0	0	0	5	11	0	0	0	0	0	0
5	207	84	0.41	60	3	6	0	0	0	0	1	2	0	0	0	0	0	0
7.5	190	94	0.49	54	5	5	11	12	0	0	6	11	0	0	0	0	0	0
10	120	71	0.59	71	1	1	24	34	0	0	7	10	6	8	7	10	1	4
12.5	162	60	0.37	59	3	5	32	53	1	2	5	8	11	19	20	34	4	21
15	180	48	0.27	48	0	0	18	38	0	0	5	10	1	2	10	21	1	6
17.5	175	62	0.35	62	1	2	31	50	0	0	9	15	8	13	25	40	4	20
total		597		414	17		116		1		38		24		62		10	51

dissoc.= dissociation of zircon no. = number; Zrn : zircon; PF = Planar Fracture; BSE = Backscattered Electrons; PDB = Planar Deformation Band; EBSD = Electron Backscatter Diffraction;

Table 2: Existing experimental constraints on twin formation

Experiment	Experiment type	Starting material	Pressure twins identified at (GPa)
This study	Dynamic shock recovery	Seeberger sandstone (25-30 vol% porosity) with accessory zircon	10
Morozova et al. (2017)	Static diamond anvil cell	Zircon powder	20

Table 3 – Existing dynamic experimental constraints on reidite formation

Experiment	Experiment type	Starting material	Pressure reidite identified (GPa)
This study	Dynamic shock recovery	Zircon in sandstone host (25-30% porosity)	10
Erickson et al. (2020)	Dynamic shock recovery	Zircon powder	21.2
Kusaba et al. (1985)	Dynamic shock recovery	Zircon powder	30
Leroux et al. (1999)	Dynamic shock recovery	Thin zircon plates	40

Table 4. New shock stage classification for zircon in dry, porous (25-30%) sandstone.

Shock Stage	Effects in sandstone target (from Kowitz et al., 2016)	Shock features in quartz (vol. %, from Kowitz et al., 2016)	Calculated applied pressure (GPa)	Shock effects for zircon (this study)
0	Undeformed sandstone (reference)	0	0	irregular fractures (not shock metamorphism related)
1a	Compacted sandstone with remnant porosity	0	< 1.5	(not evaluated)
1b	Compacted sandstone with zero porosity	0 to 2	2.5	PF, PDB
		0 to 2	5.0	PF, PDB
1c*		0 to 2	7.5	PF, PDB, melt films
2	Dense (Non-Porous) sandstone with dialectic quartz glass, SiO_2 melt, SiO_2 high-pressure phases, SiO_2 glass (lechatelierite), and quartz	2 to 20	10.0	PF, PDB, melt films, {112} twins, reidite
			12.5	PF, PDB, melt films, {112} twins, reidite*
3		20 to 50	15.0	PF, PDB, melt films, {112} twins, reidite
4		50 to 85	17.5	PF, PDB, melt films, {112} twins, reidite
5	Vesicular (pumaceous) rock, dominantly SiO_2 glass (lechatelierite)	>85	>18	Granular (FRIGN) zircon

GPa = gigapascal; PF = planar fractures; PDB = planar deformation bands

Shock stage 5 data for zircon are from Coconino sandstone (Cavosie et al., 2016)
*The 12.5 GPa sample also had evidence of dissociation within melt films on the margins of two zircon grains. This was not observed in any of the higher pressure samples.